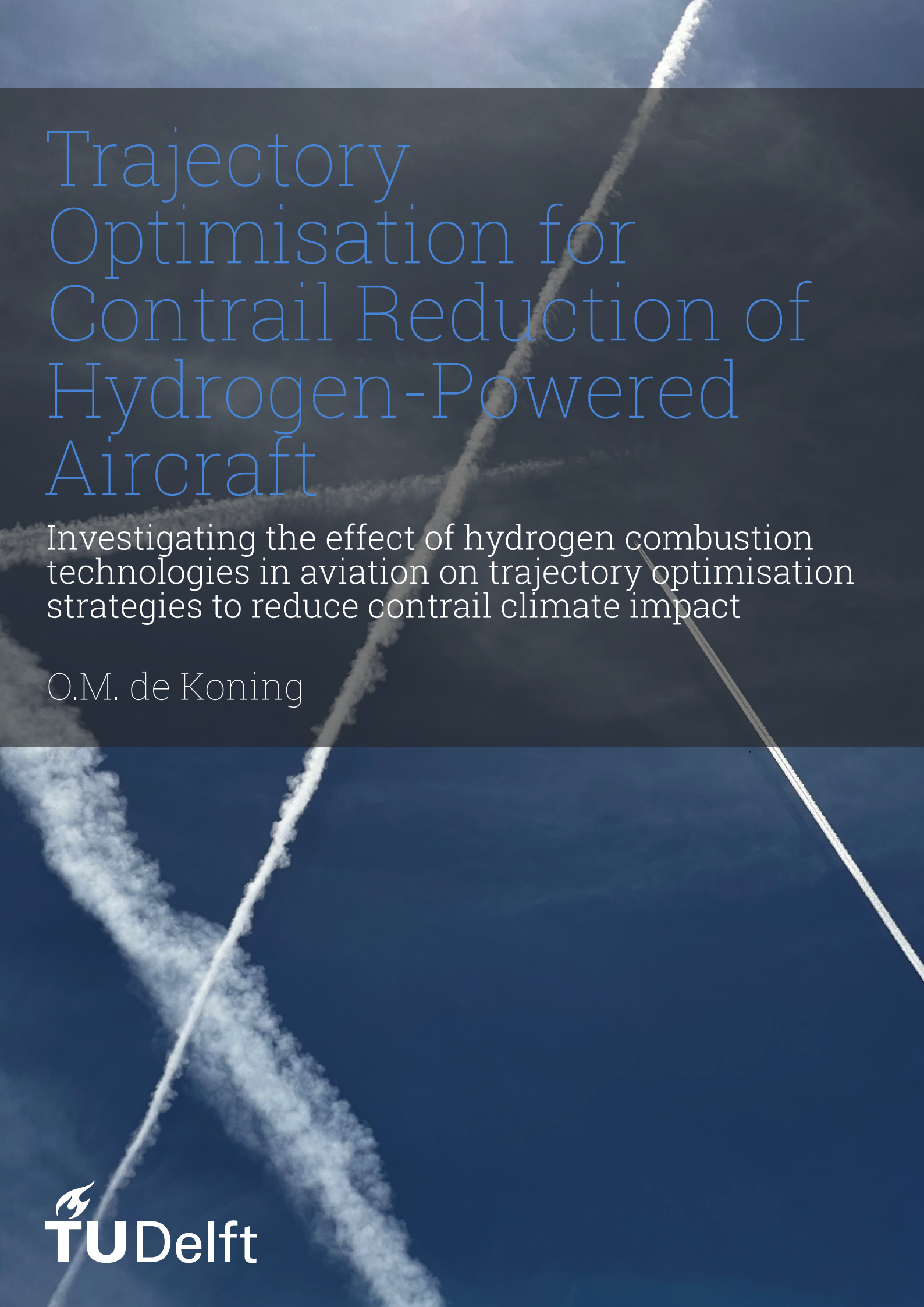

Trajectory Optimisation for Contrail Reduction of Hydrogen-Powered Aircraft

Investigating the effect of hydrogen combustion technologies in aviation on trajectory optimisation strategies to reduce contrail climate impact

O.M. de Koning

TU Delft

Trajectory Optimisation for Contrail Reduction of Hydrogen-Powered Aircraft

Investigating the effect of hydrogen combustion technologies in aviation on trajectory optimisation strategies to reduce contrail climate impact

by

O.M. de Koning

to obtain the degree of Master of Science
at the Delft University of Technology,
to be defended publicly on Thursday February 13, 2025 at 10:00 AM.

Student number:	4822870	
Project duration:	April 15, 2024 – February 13, 2025	
Thesis committee:	J. Sun, PhD	TU Delft, supervisor
	Dr. ir. D. Engler Faleiros	NLR, supervisor
	Prof. dr. ir. J.M. Hoekstra	TU Delft
	F. Yin, PhD	TU Delft
	E.J. Roosenbrand, MSc	TU Delft

Cover:	Contrail and contrail cirrus development in Dutch skies. Taken by Joseph Michaels.
Style:	TU Delft Report Style, with modifications by Daan Zwaneveld

An electronic version of this thesis is available at http://repository.tudelft.nl/.

TU Delft

Preface

If I had a dollar for every time someone mentioned the conspiracy theory on contrails when I told them what I did for my thesis, I'd have a nice graduation bonus by now. There are few aerospace-related topics that people encounter so often, and most know so little about. To be honest, the main reason for me to pursue this topic was that I knew so little about contrails and what they will mean for the climate impact of hydrogen-powered air travel. I wanted to be able to discuss the potential of hydrogen technologies for aviation with those who worry about the non-CO_2 effects, and I was getting slightly annoyed with not knowing anything about it.

The research, in the end, was fun and very interesting, not yielding the results I may have expected but certainly increasing my understanding of the climate effects of hydrogen-powered aircraft. I have a newfound appreciation for the hard work that is required to complete a comprehensive research in the field of aerospace engineering, including all the challenges and obstacles that come with it. But mostly, it was a great experience to bundle all the knowledge, skills, and previously received feedback to face the final challenge of this master's program. Being called 'organised' by my supervisor was a personal highlight for me, as this trait was usually at the 'constructive feedback' side of my evaluations.

I had many ideas of how to approach my research topic, and I was fortunate to find two great supervisors who helped me formulate a comprehensive plan for my thesis. Many thanks to David, who is an amazingly friendly supervisor with incredible research skills, and to Junzi, whose constant optimism always kept my morale high. I would also like to thank my thesis committee, who were present at many important milestones to provide feedback that helped me shape the research to what it has become.

Luckily for me, David is part of the Sustainability Team at NLR, where I spent time in the office and could leverage the incredible amount of knowledge available in this team. Working alongside this team substantially improved my knowledge on non-CO_2 effects, and motivated me to put in my best effort to contribute to this research field. For this, I would like to thank everyone at the Sustainability Team at NLR, with a special thanks to Wessel for helping me find my way in the world of contrails and being a great friend in the workplace.

Switching between NLR and the TU Delft was a great way to combine contact with professionals in the industry and fellow thesis writers. The days I worked at TU Delft were a mix of motivating one another and pulling each other away from our stations to grab a coffee. Many thanks to Julia, Korneel, Rahiq, Mees, and others in SIM.04, for making every day at TU Delft fun and motivating. And of course, a special thanks to Joey, who has challenged me to become a better aerospace engineer since we first started the BSc program in 2018. Being able to finish our theses alongside each other, including late nights fuelled on burgers and sushi, was a great way to end my time in Delft.

Lastly, I would like to thank my family and friends for supporting me throughout. My parents of course, for providing me with the opportunity to complete my studies at this university, and Rebecca for continuously motivating me to become better at what I do and for keeping me sane when things got rough. And Benjamin, for the interest he showed in my work and for being a great engineer whose example I will try to follow in my future pursuits.

O.M. de Koning
Delft, January 2025

Summary

Airlines worldwide have committed to the goal of achieving carbon neutrality in 2050. This goal is to be reached using a combination of sustainable aviation fuel (SAF), carbon offsetting, operational improvements, and the implementation of new propulsion technologies. Electric propulsion is expected to be applied for short-haul flights, while hydrogen-powered aircraft have the potential for medium-range routes too. Although these aircraft types are certain to cut the in-flight carbon emissions of the aviation sector if they are integrated into commercial fleets, the impact of hydrogen-powered aircraft on non-CO_2 climate effects is still rather unknown. The non-CO_2 effects of conventional aircraft have been researched extensively, focussing primarily on the climate impact of NO_X and contrails. Both climate effects are location dependent, meaning that the climate impact is correlated with local values of atmospheric properties. As the location dependency of contrails is the most significant, the bulk of the research on this topic is focused on trajectory optimisation for contrail reduction. The introduction of hydrogen-powered aircraft in the aviation system could add an extra dimension to this research, as the lack of carbon emissions reduce the negative effects of route diversions.

This research considers three aircraft concepts: a current aircraft powered by Jet A-1, an aircraft with technological improvements powered by a 70% SAF blend, and an aircraft powered by hydrogen combustion. The effect of trajectory optimisation for each aircraft type highly depends on the contrail climate impact of the fuel-optimal flight. Simulations in *pycontrails* show that flying on hydrogen can cause a decrease in contrail ice crystal numbers of 89% compared the contrail of a conventional aircraft, and 81% of that of future aircraft powered by a 70% SAF blend. The resulting decrease in climate impact is 87% and 79% compared to the two other aircraft types, respectively.

Two approaches to using contrail analysis for trajectory optimisation are proposed in this research. The first is based on using *pycontrails* to find correlations between the contrail climate impact and atmospheric properties, which can be used for formulate new algorithmic climate change functions (aCCFs). This method proved not to be applicable as low correlations were found between atmospheric variables at the location of contrail formation and contrail energy forcing. The physical processes modelled in *pycontrails* do not seem to sufficiently well-captured by aCCFs that only take into account the conditions at the contrail onset. The second method is based on directly forming a contrail cost grid in *pycontrails*. Although this method is more complex to implement, it yields more accurate results.

The resulting contrail climate impact grids are subsequently used for trajectory optimisation, performed in *OpenAP-TOP*. The fuel-optimal route per concept aircraft is determined for six different trajectories, after which weighted combinations of fuel and climate costs are passed through the program to end up with a range of small and larger route diversions for climate cost savings. The results show a high impact of trajectory optimisation for the Jet A-1 aircraft concept and the future aircraft concept flown on the 70% SAF blend, decreasing the P-ATR20 climate impact by approximately $25 - 50$ pK and $10 - 30$ pK, respectively, for the analysed case studies. Route diversions for hydrogen-powered aircraft show limited benefits (< 3 pK), which can be directly related to the relatively small contribution of contrails to the total climate impact of hydrogen-powered flights. For their fuel-optimal routes though, hydrogen-powered aircraft reduce the total climate impact of a flight greatly: generally, a 80-90% reduction in total climate impact is realised compared to Jet A-1.

Contents

Nomenclature

Abbreviations

Abbreviation	Definition
aCCF	Algorithmic Climate Change Function
AGTP	Absolute Global Temperature change Potential
AGWP	Absolute Global Warming Potential
ATR	Average Temperature Response
DOC	Direct Operating Costs
F-ATR	Future emission Average Temperature Response
ISSR	Ice-Supersaturated Region
nvPM	non-volatile particulate matter
OEM	Operational Empty Mass
OpenAP	Open Aircraft Performance model
P-ATR	Pulse emission Average Temperature Response
PMO	Primary Mode Ozone
SMR	Short-Medium Range
TOM	Take-off mass
TOP	Trajectory Optimiser
USD	United States Dollar
vPM	volatile particulate matter

Symbols

Symbol	Definition	Unit
c_p	Specific heat capacity of air	$\mathrm{J\,(kg\,K)^{-1}}$
$\mathcal{D}$	Dilution	$-$
EI	Emission index	$\mathrm{kg\,kg_{fuel}^{-1}}$
F	Thrust	N
G	Mixing line gradient	$\mathrm{Pa\,K^{-1}}$
h	Altitude	m
M	Mach number	-
m	Aircraft mass	kg

Symbol	Definition	Unit
$\dot{m}_f$	Fuel mass flow	$\mathrm{kg_{fuel}\,s^{-1}}$
n_w	Number concentration of water droplets	$\mathrm{cm^{-3}}$
OLR	Outgoing long-wave radiation	$\mathrm{W\,m^{-2}}$
p_a	Ambient pressure	Pa
PV	Potential vorticity	PVU
Q	Specific heat of fuel combustion	$\mathrm{J\,kg^{-1}}$
r	Mean particle radius	$\mu\mathrm{m}$
r_K	Kelvin radius	m
RF	Radiative forcing	$\mathrm{W\,m^{-2}}$
RH_w, RH_i	Relative humidity over water, over ice	$-$
s_w	Supersaturation over water	%
SDR	Solar direct radiation	$\mathrm{W\,m^{-2}}$
T	Absolute temperature	K
T_E	Engine exit temperature	K
V	True airspeed	$\mathrm{m\,s^{-1}}$
vs	Vertical speed	$\mathrm{m\,s{-}1}$
w	Weights for trajectory optimisation	-
x_p	Projected longitudinal values	deg
y_p	Projected latitudinal values	deg
β	Dilution factor	-
ϵ	Ratio of molar masses	-
η	Overall propulsion efficiency	-
Φ	Geopotential	$\mathrm{m^2\,s^{-2}}$
ψ	Heading	rad

1 Introduction

1.1. Background

In order to meet the aviation sector's goal of becoming carbon neutral in 2050, new types of aircraft are planned for market entry in the near future (IATA, 2021). Electric and hybrid-electric aircraft are set to be integrated into commercial fleets before 2035 and hydrogen-powered aircraft are expected to follow around 2040 (IATA, 2021). Although it is commonly believed that these new technologies will significantly reduce CO_2 emissions in the industry, there are concerns about their non-CO_2 climate impact. The emergence of hydrogen-powered flight technology comes at a time that concerns rise about the climate effects of contrails. These concerns have led to research into the efficacy of rerouting strategies to avoid contrail formation (Martin Frias et al., 2024). However, these route diversions result in increased CO_2 emissions, which decreases the positive climate impact of the rerouting strategies. Despite higher water emissions, contrails formed by hydrogen-powered aircraft are expected to have a smaller climate impact than those produced by regular aircraft (Bier et al., 2024; Clean Sky 2 JU & FCH 2 JU, 2020). Previous research has shown the alternative process of contrail formation for hydrogen as an aviation fuel, the variables that affect it, and what it means for contrail properties that affect its climate impact (Bier et al., 2024). Dependencies of contrail formation on additional atmospheric variables compared to conventional aircraft, such as ambient particle concentrations and radii, indicate that trajectory optimisation for hydrogen-powered aircraft requires a new approach compared to the approach used for conventional aircraft. Furthermore, due to the absence of CO_2 emissions, the penalty of route diversions for hydrogen-powered aircraft in terms of negative climate effects will likely be lower.

1.2. Research question

This thesis aims to increase our understanding of contrail climate impact by hydrogen-powered aircraft and the effect of route diversions to avoid contrail formation. Therefore, its main research question is formulated as follows:

How cost efficient can the climate impact of hydrogen-powered aircraft contrails be minimised through trajectory optimisation?

In order to answer the above question in a comprehensive manner, several subtopics are to be explored extensively through which the focus shifts throughout this thesis. First, the features of a contrail climate impact model must be investigated which are increasingly important when modelling hydrogen-powered aircraft contrails. Then, the additional variables are explored on which contrail formation for hydrogen-powered aircraft depends and how changes in these variables affect the contrail's climate impact. Finally, after trajectory optimisation is performed for different aircraft types, the effect of hydrogen-powered aircraft diversions for trajectory optimisation is compared to that of conventional aircraft types.

1.3. Report structure

The current research is split into several parts, starting with the literature review in chapter 2. This literature review covers the relevant state-of-the-art knowledge on contrail climate impact modelling in section 2.1, hydrogen-powered aircraft and how these fit into our current understanding of contrails in section 2.2, and trajectory optimisation for climate impact reduction in section 2.3.
The methods described in chapter 3 cover the models and tools used for this thesis, as well as the model inputs chosen to obtain results. Section 3.1 describes the methods used for contrail analysis and section 3.2 the methods for the trajectory optimisation. The choice of case studies used in this research is described in section 3.3.
The results are presented in chapter 4. Section 4.1 shows the output of the contrail analysis conducted for the current research. First, the analysis of a single hydrogen-powered flight is shown, after which an analysis of contrail climate impact for trajectory optimisation purposes is presented. In section 4.2, the results of trajectory optimisation are shown. The climate effects of all case studies are given for their fuel-optimal flight paths, after which the the decrease in climate impacts for route diversions are shown. Section 4.3 analyses variations in model parameters and inputs and their impact on the results.
Chapter 5 discusses the results and the methods that were used to obtain them. Section 5.1 analyses how the current results were affected by limitations during this research. Section 5.2 proposes next steps in research to further investigate the topic at hand.

2

Literature review

This chapter presents the literature review that is conducted to identify knowledge gaps to be focussed on in the current research. In the end, the goal of this research is to contribute to the understanding of contrail climate impact resulting from hydrogen-powered aircraft and the potential of trajectory optimisation to mitigate these effects. This mission statement presents three distinct areas of research that are to be treated separately in this literature review. Section 2.1 explains the physics behind contrail development, the factors that determine the persistence of contrails, and their resulting climate impact. Specifications of hydrogen technologies for aviation and how they affect contrail formation are described in section 2.2, followed by a brief introduction to trajectory optimisation in section 2.3.

2.1. Contrail development and climate impact

Prior to understanding contrail formation by hydrogen-powered aircraft, it is key to research the state-of-the-art knowledge on conventional contrail formation. This section dives into the physical process of contrail formation, what determines a contrail's persistence, and how their climate effects fit into the total climate impact of the aviation sector.

2.1.1. Contrail formation

The process of contrail formation depends on several factors that are discussed in this subsection. The well-known Schmidt-Appleman criterion is introduced first, after which the microphysical contrail formation model and the role of condensation nuclei for water activation are explained.

Schmidt-Appleman criterion

The basis for any contrail formation process is the Schmidt-Appleman criterion (Appleman, 1953; Gierens, 2021; Schmidt, 1941). This criterion is based on the thermodynamic processes surrounding the mixing of the exhaust plume and ambient air. This mixing process can be visualised by the solid line, known as the mixing line, in Figure 2.1(a). The mixing of the exhaust plume into ambient air can be seen as a process from the top-right of Figure 2.1(a), where the air is hot and moist, to the bottom-left, where it has mixed sufficiently with the surrounding air to decrease its temperature and water vapor content to ambient levels (Kärcher et al., 2015).
The slope G of the mixing line can be calculated by Equation 2.1 (Gierens, 2021).

$$G = \frac{c_p p_a}{\varepsilon} \frac{EI_{\mathrm{H_2O}}}{(1-\eta)Q} \tag{2.1}$$

where c_p is the heat capacity of air, p_a is the ambient air pressure, ε is the ratio of molar masses of water and air ($\varepsilon = 0.622$), $EI_{\mathrm{H_2O}}$ is the emission index of water in $\mathrm{kg_{H_2O}/kg_{fuel}}$, η is the overall propulsive efficiency, and Q is the heat of fuel combustion in $\mathrm{J\,kg^{-1}}$.
The slope of the mixing line is crucial to determine whether contrails form. Water droplets form when the plume becomes saturated with respect to liquid water, which occurs at the cross in Figure 2.1(a). These droplets freeze soon after they form. The plume continues to cool down until ambient conditions are reached. This occurs at the dot in Figure 2.1(a).

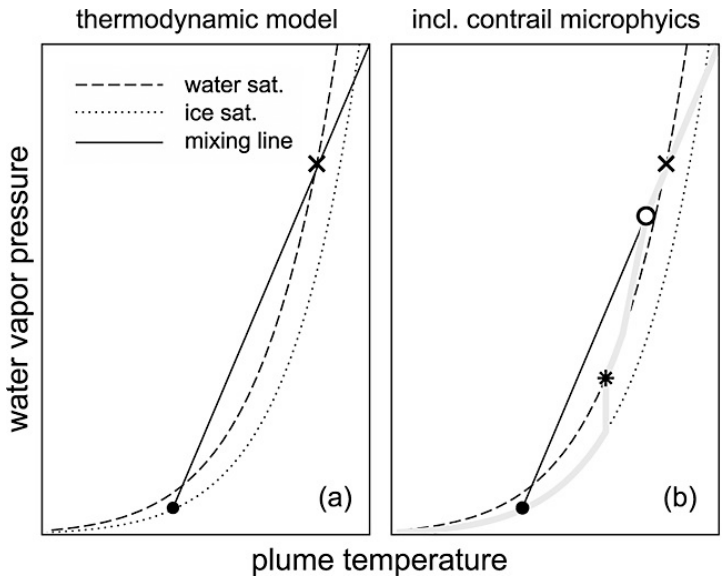

Figure 2.1: Comparison of the thermodynamic model for contrail formation and the same model with the addition of microphysical calculations. The cross marks the first water-saturated conditions in the engine's exhaust plume during its cool-down, the open circle marks the point of activation-relaxation, the star marks the point of freezing-relaxation, and the dot marks the end of the plume cool-down (Kärcher et al., 2015).

While the plume is located in an atmospheric region that is supersaturated over ice, so called ice-supersaturated regions (ISSRs), ice crystal dissipation cannot occur. Therefore, a contrail is considered persistent if the plume remains within an ISSR after mixing is complete. This is the case in Figure 2.1(a), where the dot is located above the line of ice saturation. If the contrail is located outside of ISSRs, the dot is below the line of ice saturation and the ice crystals dissipate.

Microphysical model

If a contrail is formed, the thermodynamic approach used for the Schmidt-Appleman criterion accurately defines the points where the exhaust plume enters the state of water- and ice-supersaturation and when the mixed air leaves this state. However, the processes during the supersaturation phases are not described well when purely relying on thermodynamics. A deeper understanding of microphysical processes is required to perform accurate modelling of contrail formation. A microphysical approach to contrail formation modelling is introduced to better understand what happens during contrail formation on a smaller scale (Kärcher et al., 2015).

The microphysical process for contrail formation is presented by Kärcher et al. (2015) and builds on the Schmidt-Appleman criterion. This model is shown in Figure 2.1(b). The microphysical model follows the same basic principles as the thermodynamic model, but provides a more detailed description of the ice crystal formation process once the mixing line has become supersaturated with respect to water. There are two extra points of significance in the microphysical model: the points of activation-relaxation and freezing-relaxation, marked by the open circle and the star in Figure 2.1(b), respectively (Kärcher et al., 2015). Activation-relaxation means that once the wetted-aerosol grows beyond its critical radius (activation), forming water droplets, the water vapor pressure decreases, which results in less super-saturation of the plume with respect to water. Freezing-relaxation occurs when the ice mass content in the plume increases, causing the level of ice-supersaturation to decrease towards saturation.

Condensation nuclei

Much of the water activation at the start of the contrail formation process occurs through condensation onto particles in the exhaust plume. These particles can be either directly emitted by the aircraft or entrained in the exhaust plume from the surrounding air.

The combustion of conventional aviation fuels produces soot, which is the most significant contributor to water activation in the exhaust plume (Kärcher & Yu, 2009). Another contributor is sulphur that can be found in kerosene, which forms sulphuric acid and acts as a coating around soot particles, increasing their performance as water activation platforms (Kärcher & Yu, 2009).

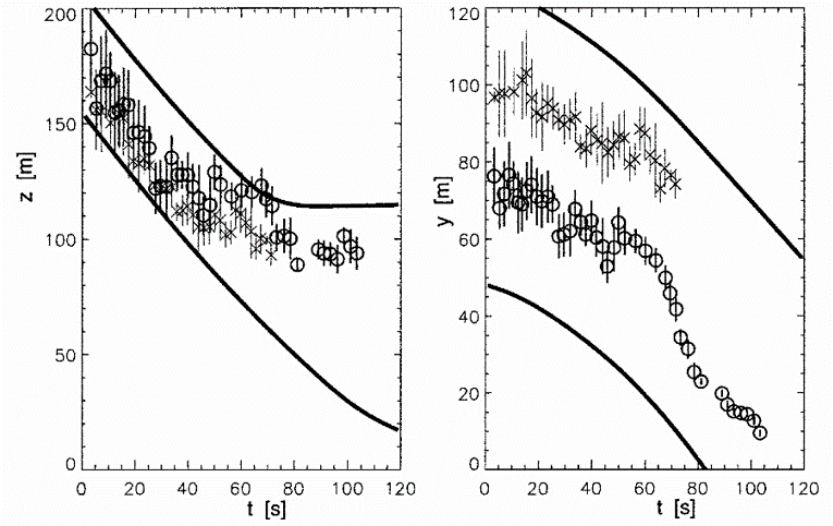

Figure 2.2: Vertical (left) and lateral (right) displacements of port (open circle) and starboard (right) vortices behind aircraft. The vertical lines are the error bars of the lidar observations, and the solid lines indicate the bounds of the expected behaviour following a prediction model as presented by Holzäpfel (Holzäpfel, 2003).

Another contributor to contrail formation are atmospheric particles, which are usually found as matter dissolved in supercooled aerosols (Kärcher & Yu, 2009). These particles play a much smaller role in water activation than soot particles. Soot emissions need to decrease with a factor 10 to 100 (compared to conventional combustion) before atmospheric particles become a higher contributor to contrail formation (Kärcher & Yu, 2009).
Whatever type of particle, its ability to act as condensation nuclei is strongly related to the Kelvin radius r_K. Particles with a radius near r_K need very high levels of supersaturation to perform water activation (Kärcher et al., 2015). The value of r_K is approximately 1 nm. However, water activation can become quite difficult for particles even for values of r above 1 nm. This has everything to do with the Kelvin effect: larger particles need less supersaturation for water activation. This phenomenon and its impact on contrails is more elaborately explained in subsection 2.2.2. Bier et al. (2024) state that the ability of ambient particles to function as condensation nuclei decreases at values of $r \leq 10$ nm.

2.1.2. Contrail persistence

Not all contrails have a significant climate impact. In most areas of the atmosphere, the ambient air is not saturated with respect to ice and the ice crystals that form contrails dissipate into the air within several seconds or minutes. Contrails are a problem if they are warming and persistent, that is, if they continue to exist for multiple hours after forming. This happens in ISSRs as explained in subsection 2.1.1. This can happen if the initial formation of contrails takes place in such a region and stays there, or if the contrail initially forms elsewhere and is transported to such an atmospheric region. For both cases, it is important to determine the dynamics of the contrail to predict its persistence.
Within the first seconds of the contrail formation process, the exhaust plume is caught in the wake vortices behind the aircraft. The circulation of this vortex creates a net downward displacement of the exhaust plume and influences its lateral displacement (Holzäpfel, 2003). The resulting vertical and lateral displacements are shown on the left and right in Figure 2.2, respectively. Accurately modelling these transport dynamics is key in determining the persistence of contrails.
Combining these insights in air mass transportation with meteorological data provides sufficient information to determine whether contrails are located in atmospheric regions where they can persist.

2.1.3. Contrail radiative forcing

A contrail's climate impact can be measured by its radiative forcing (RF): the net radiative flux that results from blocking outgoing long-wave radiation (OLR) and reflecting incoming short-wave (solar) radiation in the Earth's atmosphere. To relate the radiative forcing of contrails to their total climate impact, the effective radiative forcing must be determined. This can be done by multiplying the radiative

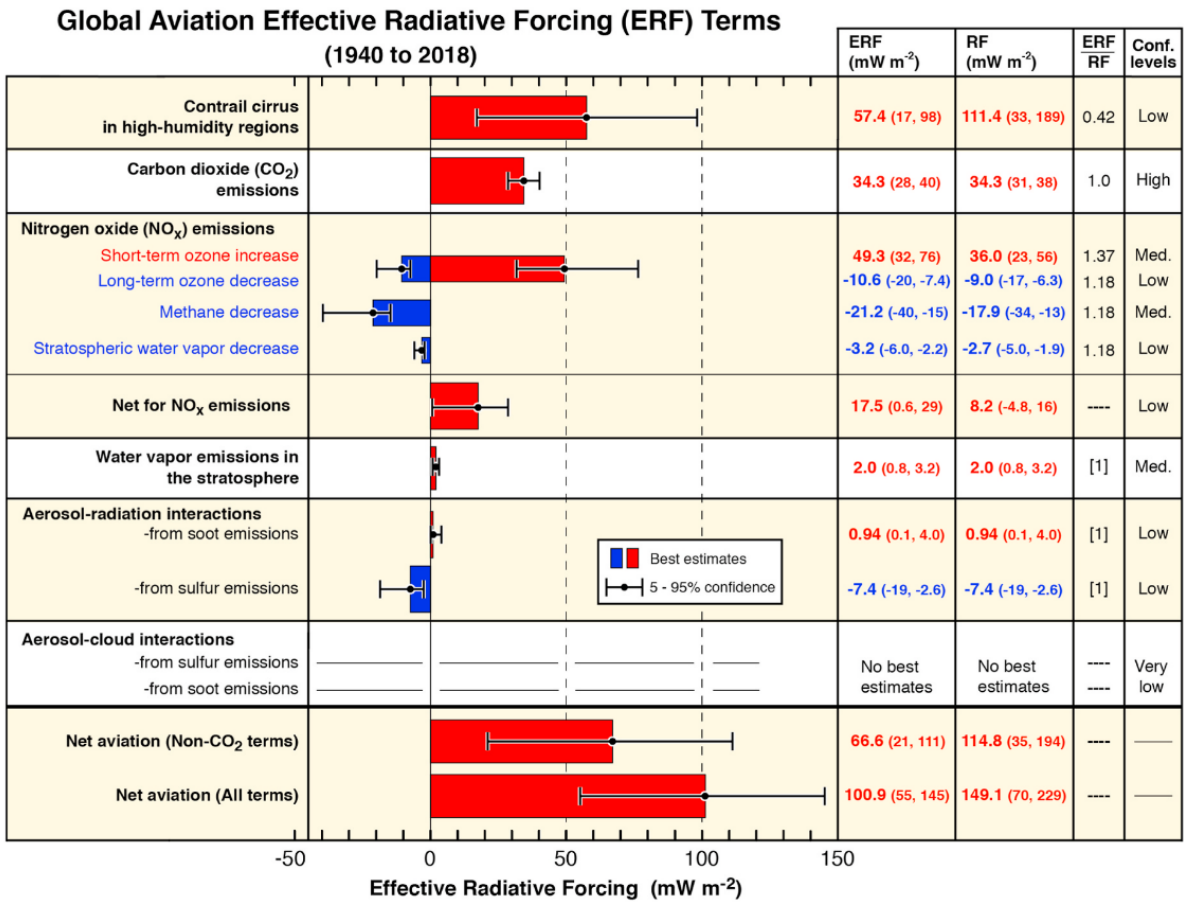

Figure 2.3: The contributions of the dominant climate forcing terms between 1940 and 2018 to the effective radiative forcing of the aviation sector in 2018. The best estimates of these terms are shown, accompanied by the 5%-95% confidence intervals. Warming effects are shown in red and net-cooling effects in blue. The image is created by Lee et al. (2021).

forcing with a factor of 0.42 to account for the fact that contrail cirrus is not evenly distributed throughout the atmosphere and triggers other atmospheric processes than CO_2, causing it to be less effective in increasing the Earth's temperature (Dietmüller et al., 2023; Lee et al., 2021). Lee et al. (2021) estimate the effective radiative forcing contributions in 2018 of the dominant types of aviation emissions between 1940 and 2018 as shown in Figure 2.3. The figure shows that the effective radiative forcing of contrails is a significant portion of the total effective radiative forcing of the aviation sector and is subject to great uncertainties.

The radiative forcing of contrails has several interesting aspects, one of which is the time dependency of its net effect. Day-time contrails have the potential to have a net-cooling effect on the Earth, due to their ability to reflect sunlight entering the atmosphere. The magnitude of cooling contrails is typically less than 50% of their warming counterparts that occur during the night or for other atmospheric conditions in day-time (Schumann et al., 2012). Even though only 25% of flights occur at night, they account for 60-80% of all RF of contrails (Stuber et al., 2006). Focussing on a larger timescale, 50% of all RF of contrails occurs during the winter, although only 22% of traffic occurs during this season (Stuber et al., 2006).

2.2. Hydrogen technologies for aviation

This section dives into concepts of hydrogen technology for aviation purposes and what the introduction of this technology means for the process of contrail development. Cost projections for hydrogen as an aviation fuel are also included, as these increase our understanding of the cost efficiency of trajectory optimisation in later stages of this research.

It is important to note that for this research, only hydrogen-powered aircraft with hydrogen combustion

technology are considered: hydrogen-electric aircraft with fuel cells are excluded. This decision is made based on the projected cruise altitudes of these aircraft types. Aircraft with hydrogen combustion engines are expected to fly at altitudes where ISSRs generally occur, whereas aircraft with fuel cell systems are expected to fly at lower altitudes where these regions are less likely (Lammen et al., 2022). This means that their contrail climate impact is negligible compared to that of aircraft with hydrogen combustion engines.

2.2.1. Aircraft performance

In recent years, several concepts have been developed for aircraft with hydrogen combustion engines. These concepts differ from regional aircraft to aircraft capable of long-range flights. Lammen et al. (2022) propose a concept that is modelled after an Airbus A320neo. This concept features an increased Operational Empty Mass (OEM) and fuselage length to fit the needs for a liquid hydrogen storage tank. This leads to a higher drag, higher energy consumption, and consequently a shorter range than the conventional A320neo. This concept features an adjusted maximum range of 2000 NM while maintaining the maximum payload mass of a regular A320neo.

Fuel use characteristics

Knowledge about the fuel use of aircraft is crucial for accurate contrail analysis. However, for a hydrogen-powered aircraft concept, there are large knowledge gaps due to the novelty of the technology. The values used in this research are therefore highly dependent on estimates presented in the current literature. The important characteristics of hydrogen combustion are the overall propulsive efficiency, fuel mass flow, and engine exhaust temperature.

The overall propulsive efficiency η affects the slope of the mixing line calculated by Equation 2.1. Several studies have attempted to determine the engine performance of current turbofans if conventional fuels are replaced with hydrogen. Derakhshandeh et al. (2021) observe an increase of 0.84 percentage points in overall engine efficiency when hydrocarbons are replaced by hydrogen in a GE90 turbofan: from 33.86% to 34.70%. These values result from a simulation at a cruise altitude of 10,668 m and a Mach number of 0.83. The characteristics of the hydrogen-powered GE90 model are optimised for this new fuel, leading to an increase in bypass ratio from 8.1 to 10.3. This change increases the thermal efficiencies that exceed the optimum values the hydrocarbon version of the GE90. The propulsive efficiency of the two types of engines are almost equal for Mach values lower than 1.4. A study by Balli et al. (2021) concludes differently. A thermodynamic analysis of a TF33 turbofan engine shows a 0.28 percentage point decrease when replacing $C_{12}H_{23}$ by hydrogen, decreasing the overall efficiency from 37.01% to 36.73%. The A320neo concept aircraft by Lammen et al. (2022) assumes a thermal efficiency that is equal for hydrogen-powered and conventional turbofan engines.

A notable difference between the studies by Derakhshandeh et al. (2021) and Balli et al. (2021) are that the former analyses the turbofan engines in cruise conditions and the latter in static sea-level conditions. Another important remark is that Balli et al. (2021) do not optimise the engine design for hydrogen as a fuel by e.g. increasing the bypass ratio, thus causing a lower overall efficiency.

The fuel mass flow can be deduced from traditional aircraft performance profiles combined with specifications of the hydrogen combustion variant of the A320neo (Lammen et al., 2022). This publication presents estimates for the decrease in energy consumption of a 2035 hydrogen-combustion A320neo (93% compared to a conventional A320neo). This decrease is due to general improvements that are foreseen for 2035 aircraft, combined with increases in energy consumption due to the additional weight and drag of the hydrogen-powered aircraft configuration. A 2035 aircraft powered by kerosene would have a decrease in energy consumption of 83% compared to today's aircraft. The difference in fuel consumption between hydrogen-powered aircraft and current aircraft powered by Jet A-1 can be determined by combining this 93% with the difference in lower heating values of the two fuels.

The exhaust temperature can be deducted from analyses of hydrogen-powered turbofan engines and comparisons to the same turbofan engines fuelled by Jet A-1. Derakhshandeh et al. (2021) estimate the combustion chamber outlet temperature of their optimised hydrogen-powered GE90 to be 7.7% higher than that for the conventional engine. The temperature at the nozzle exit could be lower, however, due to the higher bypass ratio used for this optimised engine. Derakhshandeh et al. (2021) do not specify the expected exit temperature. Balli et al. (2021) calculate the combustion chamber outlet temperature to be 1.4% lower for a hydrogen-powered turbofan engine than one powered by Jet A-1. Bier et al. (2024) use a value of $T_E = 580\mathrm{K}$, which is equal to the value used by Bier et al. (2022) in an earlier

study on contrail formation by conventional aircraft. It is also close to the value of $600\mathrm{K}$ used by Kärcher et al. (2015) for their microphysical analysis of contrail formation for conventional aircraft.

Emission profile

Fuel specifics of hydrogen are important for contrail development properties as well. The emission index of water ($EI_{\mathrm{H_2O}}$), expressed in kg water per kg fuel, is higher for LH_2 ($8.94\ \mathrm{kg_{H_2O}kg_{fuel}^{-1}}$) than for Jet A-1 ($1.25\ \mathrm{kg_{H_2O}/kg_{fuel}^{-1}}$) (Schumann, 1996). This causes a higher mixing line slope according to Equation 2.1.

Another feature of hydrogen-powered aircraft emissions that is of interest for contrail formation is the lack of non-volatile particulate matter (nvPM) in the exhaust plume. For regular aircraft, the main form of nvPM is soot, resulting from incomplete combustion of hydrocarbons in parts of the engine where the air-to-fuel ratio is poor (Brink, 2020). Soot plays a crucial role in the formation of conventional aircraft, as it is the main platform for water activation (see subsection 2.1.1). As nvPM are absent for hydrogen-powered aircraft, water activation happens on ambient particles entrained in the plume (Bier et al., 2024). This process is explained in more detail in subsection 2.2.2. Volatile particles are also expected to play a role in contrail formation of hydrogen-powered aircraft, but these potential condensation nuclei are excluded in recent studies due to the difficulties in modelling their role in this process accurately (Bier et al., 2024).

NO_X emissions are not directly important to contrail formation, but are crucial in understanding the overall climate impact of hydrogen-powered aircraft. For hydrogen combustion, this is the main emission type to be included in the trade-off to determine the potential reduction in climate impact of trajectory optimisation for contrail avoidance. Studies on hydrogen combustion suggest that hydrogen combustion generally increases the emission index of NO_X, but that lean combustion can be applied to decrease this emission index by approximately 25% compared to the emission index for Jet A-1 in current aircraft (Carter & Agarwal, 2021; Sáez Ortuño et al., 2023). This is consistent with the decrease in NO_X suggested by Lammen et al. (2022) for the hydrogen-powered aircraft concept used in this study. However, Sáez Ortuño et al. (2023) suggest that the actual reduction in NO_X emissions could be smaller due to altered flight profiles. Further progress in hydrogen combustion technologies, such as the micromix combustor discussed by Funke et al. (2019) could increase the reduction in NO_X emissions even further.

2.2.2. Contrails of hydrogen-powered aircraft

An adjusted approach to modelling contrails is needed due to differences in engine and emission characteristics between hydrogen-powered and conventional aircraft.

Effect on the mixing line slope

The increased water vapour content of the exhaust plume increases the mixing line slope, as explained in subsection 2.2.1. This slope is increased by a factor of approximately 2.6, due to a higher $EI_{\mathrm{H_2O}}$ and a higher heat of fuel combustion (Bier et al., 2024). Consequently, the threshold temperature at which contrails start to form is about 10 K higher than for conventional aircraft. In addition, due to larger water vapor emissions, the relative humidity over water (RH_w) and ice (RH_i) in the exhaust plume of a hydrogen-powered aircraft are higher for equal ambient temperatures than for conventional aircraft. This phenomenon is visualised in Figure 2.4.

Ambient particles as condensation nuclei

The lack of soot emissions from hydrogen-powered aircraft also significantly impacts the development of contrails. The impact of soot on water activation is shown in Figure 2.5. This figure shows the quenching of supersaturation, that is, when the number of water droplets $n_w(1)$ that can form in an exhaust plume matches the number of water droplets that must form $n_w(2)$ to decrease the supersaturation s_w to 0%. The two lines for $n_w(1)$ show the difference in water droplet numbers that can form for soot-rich ($EI_s = 10^{15}\ \mathrm{kg_{fuel}^{-1}}$) and soot-free exhaust plumes, where condensation occurs on ambient particles ($n_a = 600\ \mathrm{cm^{-3}}$). The lack of soot in the latter plume type means that there are less water activation nuclei to extract water vapour from the air, thus negatively impacting the plume's ability to quench supersaturation. For this reason, the supersaturation in the plume must increase more than for the soot-rich case, before the supersaturation forcing is sufficiently high to quench the supersaturation (Kärcher et al., 2015). When this happens, the high supersaturation forcing forces the abundant water

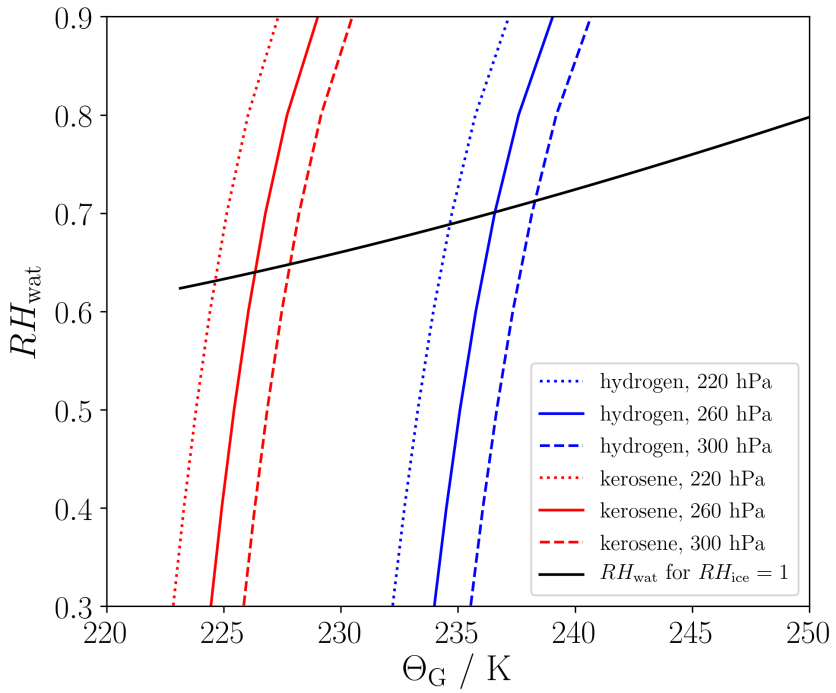

Figure 2.4: The difference in threshold temperature Θ_G for contrail formation between hydrogen-powered aircraft (blue) and kerosene-powered aircraft (red). The coloured dotted, solid and dashed lines represent threshold temperatures at 220, 260, and 300 hPa, respectively. The solid black line shows the different values for relative humidity over water RH_{wat} that are consistent with a relative humidity over ice $RH_{\mathrm{ice}} = 1$ (Bier et al., 2024).

vapour to accumulate onto the few activation nuclei present in the plume. For the near-threshold case in Figure 2.5(a), quenching occurs at similar values of s_w for both the soot-rich and the soot-free case, even with fewer water droplets in the latter case. For the soot-free, well-below-threshold case in Figure 2.5(b), the supersaturation can only be quenched when s_w increases significantly compared to the soot-rich case. The corresponding difference in the number of water droplets formed is greater than for the near-threshold case.

In addition to the increased supersaturation forcing that is necessary to quench the supersaturation, the main takeaway of Figure 2.5 is the difference in the number of water droplets. For the soot-free case, fewer water droplets and consequently fewer ice crystals are formed. However, the same amount of water vapour must condense, leading to a higher mean ice crystal mass for the soot-free case. This affects contrail properties through two distinct processes. The most obvious of these is the added gravitational pull on the individual ice crystals. This leads to ice crystals precipitating to lower atmospheric layers, where conditions force them to dissipate.

The second process that influences the contrail properties when the mean ice crystal mass and radius increase is the Kelvin effect. An ice crystal with a larger radius has a higher surface energy, shifting its critical vapour supersaturation level to the point that they experience supersaturation under the same conditions that smaller ice crystals experience subsaturation (Lewellen et al., 2014). This leads to smaller crystals forfeiting ice mass to the environment, and larger ice crystals collecting this mass, thus widening the spectrum of ice crystal radii in the contrail (Lewellen et al., 2014). This results in even larger ice crystals and the associated precipitation into lower atmospheric layers, and even smaller ones that contribute less to the contrail's radiative forcing or dissipate as a whole.

Bier et al. (2024) researched water activation on ambient particles for hydrogen-powered aircraft. This publication considers the effect of the ambient particle number concentration, dry radius, hygroscopicity and geometric width on the number of ice crystals formed. Simulations suggest among that the number concentration of aerosols is the most significant factor among ambient particle characteristics, as follows from Figure 2.6. Other results from these simulations include the number of ice crystals formed by hydrogen-powered engines relative to conventional aircraft engines, shown in Figure 2.7. These simulations show that the usage of hydrogen decreases the relative number of ice crystals formed compared to Jet A-1 contrails by 85-99% for ambient temperatures lower than 225 K, depending on

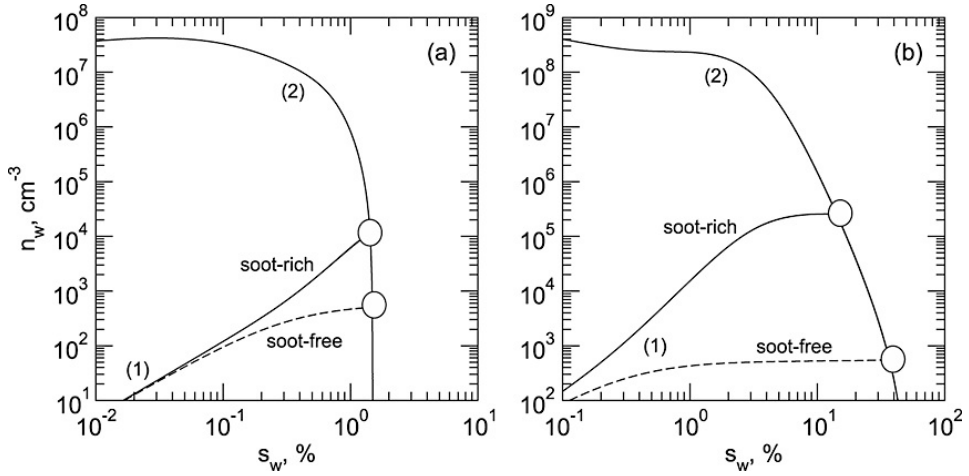

Figure 2.5: Water activation for a near-threshold (a) and a well-below-threshold (b) case, shown for both soot-rich and soot-free exhaust plumes. The soot-rich and soot-free lines, denoted by (1), show the amount of water activation that can occur in the plume, and the remaining solid line denoted by (2) shows the amount of water activation needed to quench supersaturation i.e. a sufficient amount of water activation to decrease the plume's humidity to a saturated level. The intersections between (1) and (2), marked by the open circles, indicate quenching of supersaturation for the associated level of soot emissions (Kärcher et al., 2015).

the soot emissions of the Jet A-1 fuel and the aerosol number concentrations (Bier et al., 2024).
Bier et al. (2024) consider a constant ambient particle number concentration of 600 cm^{-3} as a trade-off between Aitken-mode and accumulation-mode particle median values presented by Minikin et al. (2003) and Borrmann et al. (2010). However, the median of Aitken-mode concentrations shifts significantly for within the range of common cruise altitudes according to Minikin et al. (2003), ranging from around 700 cm^{-3} for altitudes of 9 and 11.5 km, to about 1200 cm^{-3} at 10.5 km. Brock et al. (2021) also published a study that explicitly discusses number concentrations of Aitken-mode particles and finds median values of about 2000 cm^{-3} at common cruise altitudes. However, these values are specific to tropical regions above the Atlantic and Pacific and no number concentrations are given to atmospheric regions above Europe that the current research focusses on.

The role of volatile particles

The presence of volatile particulate matter (vPM) also plays a role in contrail formation. Miake-Lye (2024) state that vPM emissions can contribute to the formation of ice crystals in two ways. If there is a high soot content in the exhaust plume, the vPM will primarily affect contrail formation by forming a hydrophilic coating on the otherwise hydrophobic soot particles (Kärcher, 1999). In the absence of soot particles, vPM nucleates with water-soluble organic matter and can consequently coagulate with water to form water droplets (Miake-Lye, 2024; Wong et al., 2015).
Volatile particles are emitted by turbofan engines as by-products of conventional fuel combustion and through the venting of engine oils (Ponsonby et al., 2024b). The main contributor to the former is the sulfur content in fossil fuels, which results in the presence of sulfuric acid in the exhaust plume. For hydrogen, this type of vPM is not an issue as the fuel itself does not contain sulfur. However, NO_x emissions could contribute to the formation of vPM, as it can react with H_2O and OH to form nitric acid (Bier et al., 2024). Furthermore, hydrogen-powered turbofan engines need lubrication oils just like conventional turbofans do. These oils can bring ultrafine oil particles into the plume that could contribute to ice crystal formation (Bier et al., 2024). The venting of lubrication oil droplets into the air could be counteracted by sealing the engines from the oil systems if this would prove beneficial to reducing the climate impact of hydrogen-powered engines (Bier et al., 2024). Experiments by Ponsonby et al. (2024b) show that even though lubrication oil droplets are less effective condensation nuclei than nvPM, below-threshold conditions can allow the former to compete with the latter for reduced nvPM emissions at high values for supersaturation.

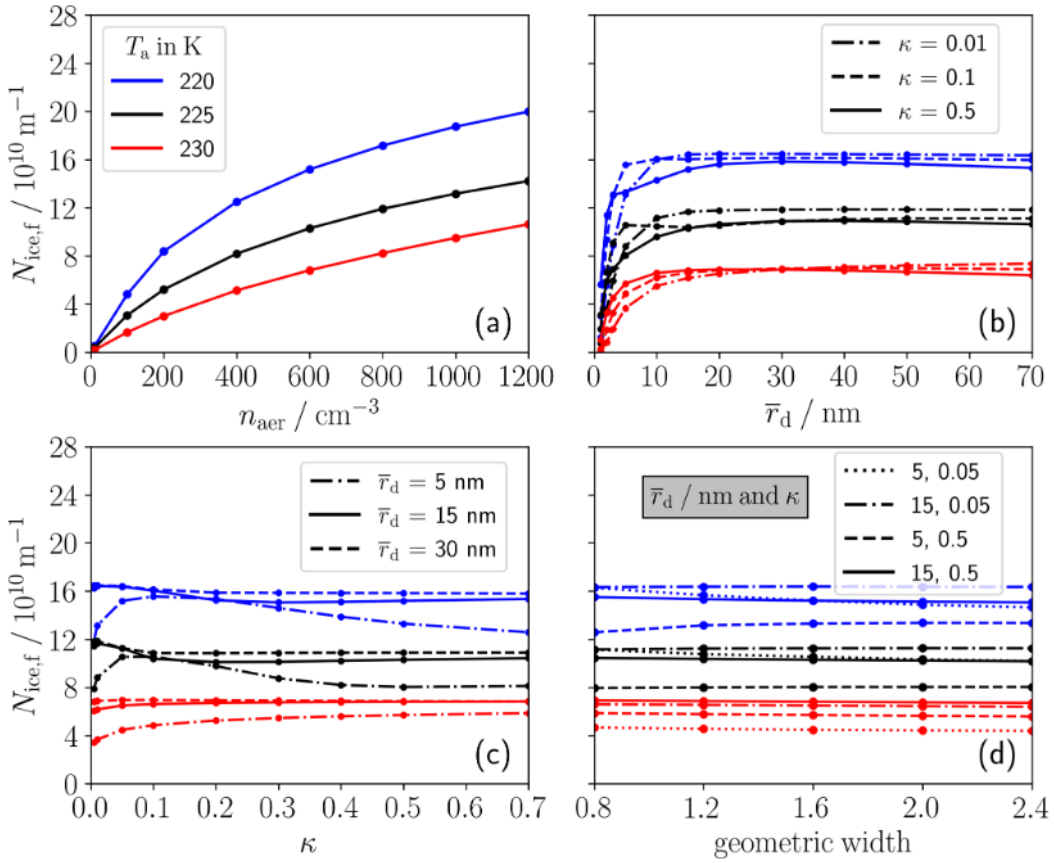

Figure 2.6: Results from Bier et al. (2024) that show the impact of ambient particle properties on contrail formation by hydrogen-powered aircraft. The number of ice crystals formed is shown on the y-axis versus (a) the ambient particle number concentrations, (b) the dry radius of ambient particles, (c) the hygroscopicity of the particles and (d) their geometric width. Variations in values of other particle or atmospheric variables are included through the use of different colours or line styles.

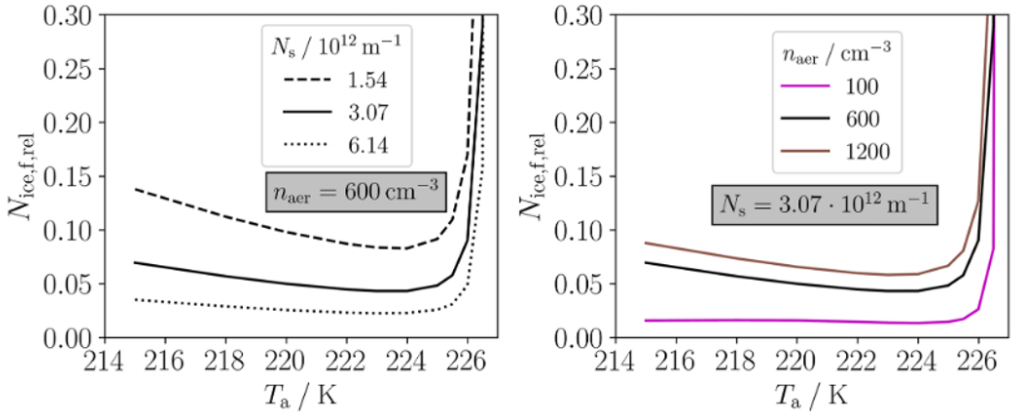

Figure 2.7: Results from Bier et al. (2024) that show the relative number of ice crystals formed compared to a contrail produced by conventional aircraft. The left figure focusses on the difference in soot particles produced by the conventional aircraft on the relative change in ice crystal formation, and the right figure shows the impact of changing number concentrations of ambient particles.

2.3. Trajectory optimisation for contrail avoidance

The altered contrail development and persistence of hydrogen-powered aircraft raise the question of whether the effectiveness of rerouting strategies differs from conventional aircraft. This section dives into the basics of climate metrics, how these can be used to form cost functions for trajectory optimisation, and other aspects to be added for a comprehensive optimisation method.

2.3.1. Quantifying climate costs

To compare the climate impact of all types of non-CO_2 effects for the trajectory optimisation of hydrogen-powered flights, as well as CO_2 emissions when comparing hydrogen-powered rerouting strategies to those of conventional aircraft, a method must be found to effectively compare the costs of these climate effects. For this, an appropriate climate metric must be chosen that climate change functions can be applied to, to determine the relative impact of different types of emissions.

Choice of climate metrics

For trajectory optimisation of conventional flight operations, it is important to be able to compare the climate impact of CO_2 and non-CO_2 effects. For hydrogen-powered aircraft, this is not an issue, but being able to compare different forms of non-CO_2 effects still plays a key role in trajectory optimisation. Several climate metrics can be used for this purpose (Borella et al., 2024; Megill et al., 2024). The Absolute Global Warming Potential (AGWP) integrates the radiative forcing over a defined time horizon (time-integrated metric). The Absolute Global Temperature Change Potential (AGTP) considers the change in global surface temperature at the end of a defined time horizon (end-point metric). A third climate metric, the Average Temperature Response (ATR), takes the average temperature change during the chosen time horizon (time-integrated metric).

The choice of time horizon is challenging and involves linking the climate metric to climate targets. Typical time horizons used for flight trajectory optimisation are 20, 50, and 100 years. The choice of a time horizon can have a significant impact on the eventual trajectory optimisation, as short-term climate effects, such as contrails, contribute significantly to the total climate impact on a short time horizon, and very little on longer horizons. Figure 2.8 shows the CO_2 equivalence of contrail climate effects per climate metric and time horizon as found by Borella et al. (2024). This graph represents a median contrail over the North Atlantic with an efficacy of 0.35 compared to the climate effect of the CO_2 emissions during a median flight (Borella et al., 2024). The values on top of each bars are the ratio of

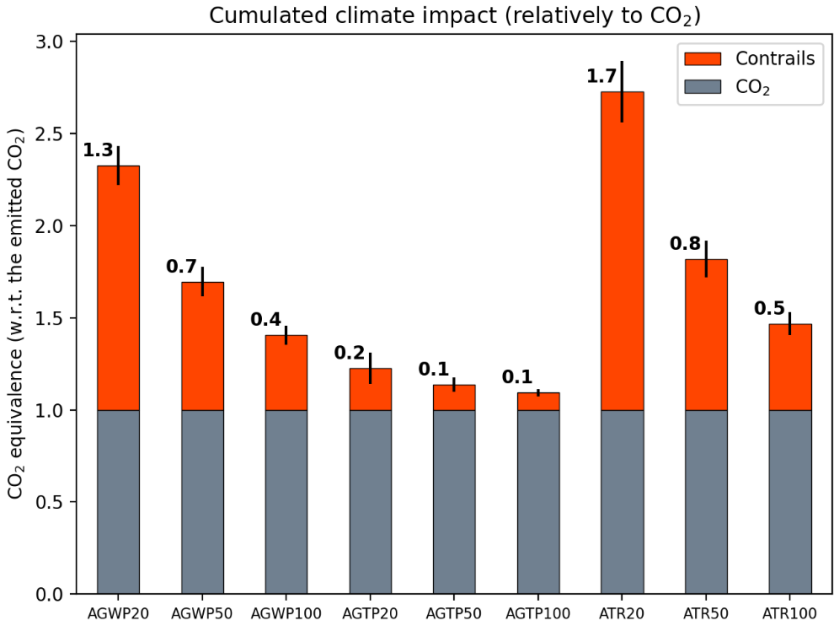

Figure 2.8: The CO_2-equivalence of contrails product by conventional aircraft according to three climate metrics with three time horizons each (Borella et al., 2024).

non-CO_2 to CO_2 climate effects, clearly showing a strong effect of the climate metric and time horizon chosen on the relative impact of the contrail climate impact compared to the CO_2 climate impact.
Finally, a metric can be classified with respect to the emission development type, e.g. pulse, sustained, or evolving. Pulse emissions are of interest when considering individual flights or flights within a short time span relative to the time horizon, and evolving emissions can be used to analyse the climate impact regarding future emissions assuming certain trends in air travel.
Metric notation usually specifies at least the climate indicator (temperature or radiative forcing), whether it is end-point or time-integrated, and the time horizon. For example, GWP20 is RF-based and time-integrated with a 20-year time horizon. Sometimes, the metric notation is also preceded by P-, S- or F- (pulse, sustained, or future emissions) to indicate the emission development type (e.g., P-ATR20).

Algorithmic climate change functions

Different types of emissions contribute to climate change through different processes. Their effect on the Earth's climate can be calculated through the use of algorithmic climate change functions, or aCCFs, which can then be linked to the proper climate metrics. These functions have been developed over the course of several studies (Irvine, 2017; Matthes et al., 2017; Van Manen & Grewe, 2019; Yin et al., 2023). An overview of the aCCFs is shown below.

- CO_2 climate impact in $\mathrm{K}\,(\mathrm{kg\,fuel})^{-1}$:

$$\mathrm{aCCF}_{\mathrm{CO_2}} = 7.48 \times 10^{-16} \tag{2.2}$$

- NO_x-induced O_3 climate impact in $\mathrm{K}\,(\mathrm{kg\,NO_2})^{-1}$, as a function of the ambient temperature T and the geopotential Φ in $\mathrm{m^2\,s^{-2}}$:

$$\widetilde{\mathrm{aCCF}}_{\mathrm{O_3}}(T,\Phi) = -2.64 \times 10^{-11} + 1.17 \times 10^{-13} \times T + 2.46 \times 10^{-16} \times \Phi - 1.04 \times 10^{-18} \times T \times \Phi \tag{2.3}$$

$$\mathrm{aCCF}_{\mathrm{O_3}}(T,\Phi) = \begin{cases} \widetilde{\mathrm{aCCF}}_{\mathrm{O_3}}(T,\Phi) & \text{for } \widetilde{\mathrm{aCCF}}_{\mathrm{O_3}}(T,\Phi) > 0 \\ 0 & \text{else} \end{cases} \tag{2.4}$$

- NO_x-induced CH_4 climate impact in $\mathrm{K}\,(\mathrm{kg\,NO_2})^{-1}$, as a function of the geopotential Φ and the incoming solar radiation at the top of the atmosphere SDR in $\mathrm{W\,m^{-2}}$:

$$\widetilde{\mathrm{aCCF}}_{\mathrm{CH_4}}(\Phi,\mathrm{SDR}) = -4.84 \times 10^{-13} + 9.79 \times 10^{-19} \times \Phi - 3.11 \times 10^{-16} \times \mathrm{SDR} + 3.01 \times 10^{-21} \times \Phi \times \mathrm{SDR} \tag{2.5}$$

$$\mathrm{aCCF}_{\mathrm{CH_4}}(\Phi,\mathrm{SDR}) = \begin{cases} \widetilde{\mathrm{aCCF}}_{\mathrm{CH_4}}(\Phi,\mathrm{SDR}) & \text{for } \widetilde{\mathrm{aCCF}}_{\mathrm{CH_4}}(\Phi,\mathrm{SDR}) < 0 \\ 0 & \text{else} \end{cases} \tag{2.6}$$

- NO_x-induced primary mode ozone (PMO) climate impact in $\mathrm{K}\,(\mathrm{kg\,NO_2})^{-1}$:

$$\mathrm{aCCF}_{\mathrm{PMO}} = 0.29 \times \mathrm{aCCF}_{\mathrm{CH4}} \tag{2.7}$$

- Water emission's climate impact, excluding contrails, in $\mathrm{K}\,(\mathrm{kg\,fuel})^{-1}$, as a function of the potential vorticity PV in standard potential vorticity units (PVUs):

$$\mathrm{aCCF}_{\mathrm{H_2O}}(PV) = 2.11 \times 10^{-16} + 7.70 \times 10^{-17} \times |PV| \tag{2.8}$$

There is also an aCCF for night-time and day-time contrails, which are functions of temperature T and outgoing long-wave radiation OLR, respectively (Yin et al., 2023). However, these are not considered during this research, as one of the main goals of this research is to develop a more accurate method to determine the climate impact of contrails for trajectory optimisation purposes. Chapter 3 explains this in more detail.

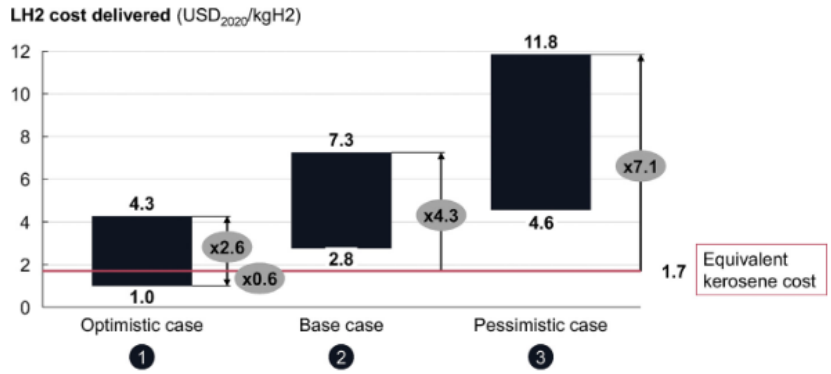

Figure 2.9: The cost of LH_2 at the dispenser for an optimistic, base, and pessimistic case, and their relation to the average cost of kerosene in 2019 (Hoelzen et al., 2022b).

2.3.2. Hydrogen cost projections

The other type of cost that must be included in a cost function for trajectory optimisation is a prognosis of LH_2 fuel costs. To directly apply this cost to flight operations, the focus lies on the price of LH_2 at the dispenser, thus including production, transportation, liquefaction, storage, distribution, and pump costs (Hoelzen et al., 2022a).

In recent years, many researchers have attempted to forecast the price of hydrogen for the next decades, both from the perspective of the aviation sector and other industries (Frieden & Leker, 2024). For this research, the scenarios presented by Hoelzen et al. (2022b) are considered. The prognoses considered in this paper are summarised in Figure 2.9. In this figure, the price of LH_2 at the dispenser is compared to kerosene prices, while accounting for the difference in the specific heat of fuel combustion. The LH_2 costs are taken from cost roadmaps and studies, focused on aviation and other sectors. The 22 cost projections are clustered into the optimistic, baseline, and pessimistic group by separating them by the assumptions made for investments in electrolysers and access electricity costs. To account for possible deviations from the scenarios presented, Hoelzen et al. (2022b) decrease the lowest cost value of each scenario is decreased by 5% and increase the highest by 20%. Hoelzen et al. (2022b) point out that aviation-focused research usually provides optimistic cost scenarios for LH_2 costs compared to research in other industries.

Comparison with kerosene prices shows that the most optimistic and the most pessimistic scenarios would mean a price change of 0.6 and 7.1, respectively. The cost of kerosene in Figure 2.9 is set at a constant price that represents an average in 2019 due to the high uncertainty in cost prognoses (Hoelzen et al., 2022b). However, the mandated SAF-share for European flights is set at 70% in 2050 (Council of the EU, 2022). Current SAF prices are over three times higher than for kerosene, indicating an increase in fuel prices for the SAF blend in 2050 compared to conventional fuel prices today (IATA, 2023).

3

Methods

This chapter describes the methodology used for the current research. The methods can be roughly divided into two categories: the approach taken for contrail analysis is described in section 3.1. This section includes an overview of the contrail analysis model inputs, the method to calculate ambient particle entrainment, and a description of how the climate costs are obtained that can be used for the subsequent trajectory optimisation. The method used to optimise flight trajectories is presented in section 3.2, which consists of the method to obtain comprehensive cost functions for flight operations and the tools used for trajectory optimisation. The case studies used to obtain these outputs are listed in section 3.3.

3.1. Analysing contrail development and climate impact

A thorough analysis of contrail climate impact is needed to obtain results for trajectory optimisation. But first, a better understanding must be obtained of contrail formation and how this differs for Jet A-1 and hydrogen as a fuel. For this, the Python library *pycontrails* (Shapiro et al., 2024), that includes the CoCiP model from Schumann (2012), is used to model contrail development and its climate impact. The CoCiP model in *pycontrails* requires datasets with meteorological and radiation data as inputs, as well as aircraft and engine characteristics and trajectory information. After analysing the difference in contrail formation processes for the two fuels, *pycontrails* is used to set up a contrail climate cost grid to be used in the trajectory optimisation algorithm. This section describes the methods used for contrail analysis in more detail.

3.1.1. Defining model inputs

The contrail analysis model must have access to accurate input data to obtain reliable results. The literature review from chapter 2 is used to this goal. Below, the different types of inputs are covered. These inputs are later used for trajectory optimisation purposes as well.

Aircraft performance

Three types of aircraft are selected for this study. First, it is important to model a currently operated aircraft fuelled by the most common aviation fuel type of today: Jet A-1. The Airbus A320 is chosen as reference aircraft because it is regularly used for short-to-medium range (SMR) flights in Europe and Airbus is already investing in research programs to develop hydrogen-powered powerplants for their aircraft[1]. Another reason to use the A320 is that the contrail analysis and trajectory optimisation software used in this research includes all models for the A320. This is not the case for the A320neo. Apart from the aircraft fuelled by Jet A-1, another aircraft type that is important to include in this research is a future aircraft powered by the most common fuel at that time, to be able to compare the hydrogen-powered aircraft trajectory optimisation to possibilities of other aircraft flying in the same time period. The fuel of this aircraft is a blend of 30% Jet A-1 and 70% SAF, as mandated by the EU in 2050 (Council of the EU, 2023). The aircraft flying at this time also have improvements in the area of e.g. energy

[1] https://www.airbus.com/en/innovation/energy-transition/hydrogen/zeroe

usage and aircraft mass, as shown by Lammen et al. (2022) in their Table 2. The aircraft powered by hydrogen combustion technologies described in this table is used for the third aircraft type that is considered in the current study: the hydrogen-powered aircraft.
In this thesis, the three aircraft types are referenced by naming their fuels: Jet A-1, 70% SAF-blend and hydrogen, but the reader should take notice that this does not only consider the fuel but also the change in aircraft characteristics listed later in this section.
The improvements for future aircraft, included in the model for the SAF blend and hydrogen-powered aircraft, are based on aircraft that enter service in 2035 (Lammen et al., 2022). As the lifetime of aircraft in commercial fleets is about 30 years[2], these improvements are assumed to be applicable to 2050 as well.
For these three aircraft types, it is important to determine the inputs for contrail analysis software, many of which are also required for the trajectory optimisation that follows. The take-off mass (TOM) for the 2000 NM flight of the current, future, and future hydrogen-powered versions of the A320neo listed by Lammen et al. (2022) are reduced according to the difference in the OEM between the A320neo and the A320. Differences in fuel usage between the two aircraft are not taken into account in this reduction. The fuel mass for the adjusted TOM is then multiplied by 0.75, to adjust the mission profile from 2000 NM to 1500 NM, the average distance of the case studies used in this research (see section 3.3).
The performance characteristics values for the A320 are determined using a cruise speed of 230 $\mathrm{m\,s^{-1}}$, consistent with data obtained from EUROCONTROL[3]. Its cruise altitude is determined by using the trajectory optimisation software *OpenAP-TOP* (Sun, 2022) to find the fuel-optimal flight path. The altitude of this path is used to calculate the mean fuel mass flow, overall propulsion efficiency, and NO_X emission index (discussed in the next subsection) during the Jet A-1 flight in *OpenAP* (Sun et al., 2020).
The fuel mass flow for the A320 are calculated in *OpenAP* using the `enroute` function of the `FuelFlow` class. This is calculated for several waypoints in the fuel-optimal flight, after which an average is taken to be used as constant model input.
Finding the overall propulsion efficiency requires values for the thrust provided by the aircraft. This is calculated in *OpenAP* using the `cruise` function of the `Thrust` class and can be used to calculate the overall propulsion efficiency of each aircraft. This value is calculated as follows (Schumann, 2005):

$$\eta = \frac{FV}{\dot{m}_f Q} \tag{3.1}$$

Where F is the thrust in N, V is the true airspeed in $\mathrm{m\,s^{-1}}$, $\dot{m}_f$ is the fuel mass flow in $\mathrm{kg\,s^{-1}}$, and Q is the specific combustion heat in $\mathrm{J\,kg^{-1}}$.
These performance characteristics are used for determining the values of the other two aircraft models, using the relative differences between the aircraft types given by Lammen et al. (2022). The difference in TOM and energy usage in their Table 2 are used to calculate the absolute values for the A320 versions of these aircraft for a range of 1500 NM.
The specific combustion heat of hydrogen is consistent with Schumann (1996) and the values for Jet A-1 and SAF are taken from Table 1 by Teoh et al. (2022).
The values for the aircraft models are shown in Table 3.1. Note that these values are used for calculating the cost grids in *pycontrails*, as the `CoCiP-grid` model requires the constant values for these characteristics. For the calculation of total climate impact and trajectory optimisation strategies, the variations of these characteristics throughout the flight are calculated by *OpenAP* and the constant values in Table 3.1 are not used.

Aircraft emissions

Similar to the aircraft performance characteristics, the emission indices of three aircraft concepts are determined through a combination of literature and modelling. Table 3.2 shows an overview of the emission indices used for the contrail analysis and trajectory optimisation.
The water emission index of hydrogen is consistent with Schumann (1996) and the indices for Jet A-1 and the 70% SAF blend are extracted from Table 1 by Teoh et al. (2022).
Soot emissions highly affect contrail formation for aircraft fuelled by Jet A-1 and SAF. To model nvPM emissions of the former, *pycontrails* uses the nvPM number emission index from the ICAO Aircraft

[2] https://www.airbus.com/en/products-services/commercial-aircraft/the-life-cycle-of-an-aircraft/operating-life
[3] https://contentzone.eurocontrol.int/aircraftperformance/details.aspx?ICAO=A320

Table 3.1: Aircraft, engine, and fuel characteristics for the three types of aircraft-fuel combinations considered for the contrail analysis. The take-off mass of a typical SMR-flight of 1000-2000 km is chosen, using Airbus A320 data as gathered by Sun et al. (2020) and relative weight differences of the aircraft types presented by Lammen et al. (2022). The values for specific combustion heat are consistent with Schumann (1996) for hydrogen and taken from Table 1 of Teoh et al. (2022) for Jet A-1 and SAF. The fuel mass flow is calculated using the aircraft performance program *OpenAP* (Sun et al., 2020) and the overall propulsion efficiency by using Equation 3.1. For these calculations, a standard true airspeed of an A320 of 230 $\mathrm{m\,s^{-1}}$ and cruise altitude of 11.2 km.

Values	Jet A-1	70% SAF blend	Hydrogen
Take-off mass [kg]	$69,100$	$64,700$	$70,600$
Specific combustion heat [$\mathrm{MJ\,kg^{-1}}$]	43.1	43.9	120.0
Fuel mass flow [$\mathrm{kg\,s^{-1}}$]	0.74	0.60	0.27
Overall propulsion efficiency [-]	0.34	0.37	0.35

Table 3.2: Emission characteristics of the considered fuel types. The values of ΔnvPM EI$_n$ for the SAF blend are calculated in *pycontrails* based on the method described by Teoh et al. (2022). The assumption that hydrogen produces no nvPM emissions is consistent with Bier et al. (2024). The values for $EI_{\mathrm{H_2O}}$ are taken from Table 1 by Schumann (1996). EI_{NO_X} for Jet A-1 is calculated in *OpenAP* (Sun et al., 2020) and the values for the SAF blend and hyrogen are consistent with the relative differences between the aircraft types proposed by Lammen et al. (2022).

Values	Jet A-1	70% SAF blend	Hydrogen
$\Delta EI_{\mathrm{nvPM},n}$ [%]	-	-48 to -56	-100
$EI_{\mathrm{H_2O}}$ [$\mathrm{kg_{H_2O}\,kg_{fuel}^{-1}}$]	1.24	1.33	8.94
EI_{NO_X} [$\mathrm{kg_{NO_x}\,kg_{fuel}^{-1}}$]	1.3×10^{-2}	8.2×10^{-3}	9.8×10^{-3}

Emissions Databank (ICAO, 2024) to directly calculate the number of soot particles emitted. To calculate the nvPM emissions of the 70% SAF blend, the method as proposed by Teoh et al. (2022) is used, which is shown in Equation 3.2. This formula is used to determine the relative decrease in nvPM number emission index as compared to a base case, i.e. an aircraft propelled by Jet A-1 without SAF blended in. This method is meant for SAF blends with a minimal relative change in hydrogen content of 0.5% compared to the base case. The considered SAF blend of 70% leads to an increased hydrogen content of 0.95% according to Table 1 by Teoh et al. (2022).

$$\Delta EI_{\mathrm{nvPM},n}[\%] = (\alpha_0 + \alpha_1 \hat{F}) \times \Delta H \times e^{0.5-\Delta H} \tag{3.2}$$

In the above equation, α_0, α_1, and α_2 are model coefficients, ΔH is the difference in hydrogen content between the fuel types and $\hat{F}$ is the thrust setting. This method is integrated in *pycontrails* to determine the $\Delta EI_{\mathrm{nvPM},n}$ for different locations in the atmosphere. This can yield quite large differences as the thrust setting $\hat{F}$ is strongly dependent on the ambient temperature and pressure. Refer to Teoh et al. (2022) Equation 2 and the supplementary material for more information on this method. For the area considered in this research and using the aircraft performance parameters discussed in the previous part of this section, values for $\Delta EI_{\mathrm{nvPM},n}$ are found ranging from approximately -48% for lower altitudes to -56% for higher altitudes.

For hydrogen, no nvPM emissions are considered, consistent with Bier et al. (2024).

The NO_X emissions for the Jet A-1 aircraft are calculated using the `nox` function of the `Emissions` class in *OpenAP*. This function is used to determine the emission index at several points and relies on the ICAO Aircraft Emissions Databank (ICAO, 2024). and an average is taken to be used in this research. The corresponding emission indices for the SAF blend and hydrogen are extracted from the relative differences proposed by Lammen et al. (2022) in their Table 2. The findings in section 2.2 show that the reduction in the NO_X emission index of hydrogen is based on applying lean combustion. This type of combustion is therefore assumed to be the baseline throughout this report. Other technological improvements for reducing NO_X emissions, such as the micromix combustor discussed in section 2.2, are disregarded.

Atmospheric variables

Information on meteorology and radiation must be provided to *pycontrails* for calculations of the climate impact of contrails. The weather and radiation data are ERA5 datasets obtained from the EU Climate Data Store[4]. The added functionality of analysing hydrogen-powered flights in *pycontrails* comes with the need to include a dataset for ambient particle concentrations, due to the high dependence of contrail characteristics on this atmospheric property (see subsection 2.2.2).

There are no datasets currently available that include the desired information on ambient particles. Existing datasets that focus primarily on coarse-mode particles, e.g. the CAMS global reanalysis (EAC4) (Inness et al., 2019), severely underestimate the number of particles available for contrail formation (Bier et al., 2024). Comprehensive datasets that also consider Aitken-mode particles, the main type of particles considered by Bier et al. (2024) for contrail analysis on ambient particles, are not available at this time. The literature review on this topic (see subsection 2.2.2) shows that papers reviewing measurements of ambient particles present number concentrations that significantly differ from each other. As Minikin et al. (2003) provide the most detailed analysis of Aitken-mode particle number concentrations at common cruise altitudes, a dataset is generated to reflect this data. More specifically, the values are modelled after Figure 4 of Minikin et al. (2003). The number concentrations of accumulation mode (0.1 - 1 $\mu\mathrm{m}$) and refractory (>10 nm) are also included, as their size ranges make them important for water activation as well (Kärcher et al., 2015; Minikin et al., 2003). This adds approximately 200 cm^{-3} compared to only considering Aitken-mode particles (Figure 4 of Minikin et al. (2003)).

For their research on contrail formation, Bier et al. (2024) consider additional properties of aerosols and soot emissions, such as the dry radius and hygroscopicity. These values affect whether or not the particles can act as condensation nuclei according to Kärcher et al. (2015). However, in *pycontrails*, it is assumed that all soot and ambient particles included in the input variables are available for water-activation. The actual number of particles that is activated is only dependent on the ambient temperature and critical temperature for the Schmidt-Appleman criterion (Shapiro et al., 2024).

One of the generated datasets for Aitken mode particle concentrations is shown in Figure 3.1. The four subfigures show how the difference in number concentrations for an altitude change of 2 km (Figure 3.1(a) and (b) vs. (c) and (d)) and a time difference of 24 hours ((a) and (c) vs. (b) and (d)). The CAMS global reanalysis dataset on coarse particles in the atmosphere (Inness et al., 2019) is analysed to observe spatial changes in concentrations and how this changes through time. The effect of the wind, slowly moving the ambient particle concentrations towards one direction, is included in the generated data sets as well.

3.1.2. Entrainment of ambient particles

Modelling the entrainment of ambient particles in the exhaust plume is an important step in determining how many particles are available for water activation. Bier et al. (2024) specifically focus on the first seconds of ice crystal formation and have extensive calculations for the entrainment of ambient particles. The focus of the current study is not the evolution of ice crystal numbers over the first seconds, but over longer time periods. Therefore, to simplify calculations, the results from Bier et al. (2024) shown in their Figure 2 are used to model the ambient particle entrainment. This figure suggests that ice crystal formation on ambient particles stops after approximately 1.5 seconds as the relative humidity over water falls too low to form water droplets. For the current research, this is chosen as the time scale for which ambient particles entering the plume contribute to ice crystal formation. It is assumed that the air leaving the engine has no ambient particles, consistent with Bier et al. (2024), and that the air entrained into the plume has the aerosol number concentrations of the ambient air, taken from the dataset described in the previous subsection. The growth of the exhaust plume is calculated by the following equations presented by Kärcher et al. (2015):

$$A(t) = \frac{A_0}{\mathcal{D}(t)}\,, \qquad \mathcal{D}(t > \tau_m) = \left(\frac{\tau_m}{t}\right)^{\beta} \tag{3.3}$$

Equation (3.3) calculates the plume cross-sectional area A in m^2 at time t in s after leaving the engine exit. $\mathcal{D}$ is the plume dilution, τ_m the mixing timescale in s, and β the dilution factor as determined by Kärcher (1999). The mixing timescale depends on the initial jet radius, and is set at $10\ \mathrm{ns}$ which is consistent with an exhaust radius of $0.5\ \mathrm{m}$ (Kärcher et al., 2015). The aerosol number concentrations

[4] https://cds.climate.copernicus.eu/

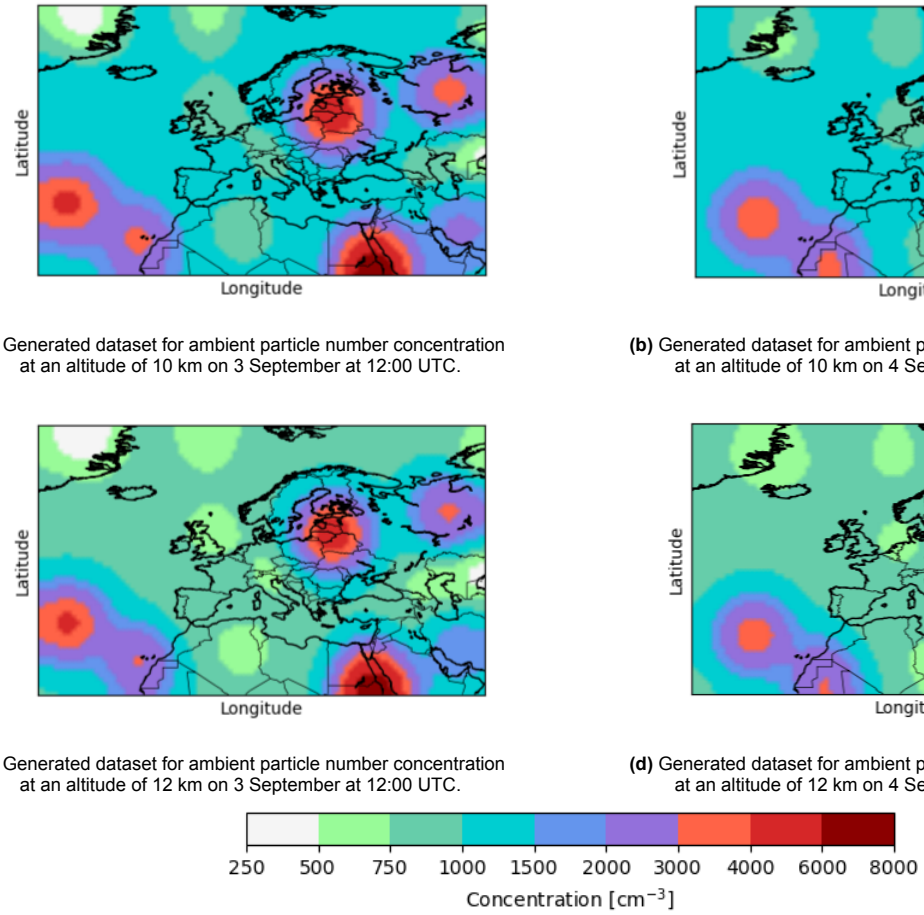

(a) Generated dataset for ambient particle number concentration at an altitude of 10 km on 3 September at 12:00 UTC.

(b) Generated dataset for ambient particle number concentration at an altitude of 10 km on 4 September at 12:00 UTC.

(c) Generated dataset for ambient particle number concentration at an altitude of 12 km on 3 September at 12:00 UTC.

(d) Generated dataset for ambient particle number concentration at an altitude of 12 km on 4 September at 12:00 UTC.

Figure 3.1: An overview of the generated number concentrations for Aitken-mode particles in the atmosphere above Europe, modelled after measurements presented by Minikin et al. (2003). These figures show concentrations at altitudes of 10 and 12 km and relative time differences of 24 hours.

from the generated datasets can then be multiplied by the area to obtain the number of ambient particles per meter, which is used by the `CoCiP` model in *pycontrails* to calculate the number of ice crystals formed.

3.1.3. Obtaining contrail climate costs

For the trajectory optimisation, a cost grid is needed that describes the climate impact of contrails above Europe. There are two approaches to this, which are both examined in this research.

The first is to form a climate impact function similar to the aCCFs discussed in section 2.3. To construct such functions, a dataset containing all flights on one day was run through the CoCiP in *pycontrails*, a model that evaluates each flight independently. A traffic dataset was used with just under 5500 flights within Europe. For each day selected for extensive contrail formation, the flights were separated into smaller segments. This action yielded over 220,000 data points. Finally, the dataset was downselected to only include flights of which waypoints met the Schmidt-Appleman criterion. The global radiative forcing per km contrail is saved as well as the atmospheric variables at midpoints of these contrail segments on which this radiative forcing depends. This way, after collecting a sufficient number of data points, correlations can be determined between these atmospheric variables and contrail radiative forcing, allowing for the development of a climate change function similar to current aCCFs. The main advantage of this method is its ease of use for further research and the biggest challenge is that the data requires strong correlations with atmospheric variables to yield accurate results.

Another method is to directly obtain climate cost grids from *pycontrails*, using its `CoCiP-grid` model. This model calculates the energy forcing per m contrail on predefined grid points. This energy forcing

can be converted to global mean radiative forcing per meter of contrail length by dividing it by the surface of the Earth in m^2 and the number of seconds in a year. To provide this grid as a function of time instead of contrail length, the grid is multiplied by the constant value for true airspeed of 230 $\mathrm{m\,s^{-1}}$. The reason for this conversion is explained further in subsection 3.2.2. This grid of time-dependent RF values can be used as a substitute for the RF calculations in the current aCCF framework for contrails as presented by Yin et al. (2023). As it does not consider flights, there is no possibility to include varying aircraft characteristics such as a decreasing aircraft mass throughout the flight. Furthermore, its ease of use is significantly lower than the previously proposed method as a grid would need to be generated separately on *pycontrails* or another contrail analysis software for each day that trajectory optimisation is to be performed. However, the method allows for more complex relations between variables that influence contrail formation and persistence, rather than relying on correlations between only a few of these.

3.2. Approach to trajectory optimisation

The outputs of the contrail climate impact analysis must be applied to trajectory optimisation. This trajectory optimisation uses the same aircraft models as presented in Table 3.1. Therefore, an objective function involving both fuel and climate costs must be realised for each of these aircraft concepts. The method for this is described in subsection 3.2.1. Section 3.2.2 describes how this cost function is used to obtain the desired data on trajectory optimisation.

3.2.1. Obtaining cost functions for flight operations

The validity of the final trajectory optimisation strongly depends on the objective functions of both the climate cost and the operating costs. The former is a combination of the output of the contrail climate impact analysis conducted prior to the trajectory optimisation and the aCCFs of other aspects of a flight's climate impact listed in subsection 2.3.1. The operating costs that are used for trajectory optimisation only include the amount of fuel used. Other direct operating costs, such as the effect of flight time on crew and maintenance costs, are not included. Operational constraints such as the increased workload for air traffic control and availability of airspace in general are also not considered.

From the climate metric options discussed in subsection 2.3.1, P-ATR20 is considered the most interesting climate metric for this research. ATR in general is a useful metric, as it directly relates aircraft emissions to the change in average global temperature, which is in line with the Paris Agreement goal of limiting the average temperature rise relative to pre-industrial times to 1.5 °C. The time horizon of 20 years is chosen as it is closest to the aviation sector wide climate goals set for 2050. The choice for P-ATR as opposed to F-ATR has to do with the fact that the application of this climate metric is meant for the trajectory optimisation of individual flights. In the current research, P-ATR20 is expressed in terms of pK (10^{-12} K) global warming.

For the climate cost function to be used during trajectory optimisation, the aCCFs listed in subsection 2.3.1 are used to determine the climate impact of CO_2, NO_X, and H_2O. The contrail radiative forcing is calculated using contrail analysis software described in the previous section, after which it is multiplied by a factor of 0.0151 to translate it to the P-ATR20 climate metric, consistent with Yin et al. (2023). The aCCFs for CO_2, NO_X, and H_2O are adapted for the different fuel types. To this goal, the aCCF for H_2O is adapted for the differences in water vapor emissions of the different fuels, and the CO_2 aCCF is set to zero for hydrogen. The latter is not adjusted for the SAF blend, as only in-flight emissions are important for trajectory optimisation. The differences in total CO_2 emissions between SAF and Jet A-1 result from using previously captured CO_2 in the production of the fuel, rather than reducing in-flight CO_2 emissions.

The aCCFs are calculated on a grid and added to the contrail climate cost grid. Note that this means that standard values for the climate costs are calculated per time and location, and that the climate costs therefore do not depend on varying aircraft and emission characteristics throughout the flight, like changes in aircraft mass, fuel flow and emission indices. For these characteristics, the constant values shown in Table 3.1 and Table 3.2 are used. This limitation is further discussed in section 5.1.

3.2.2. Performing trajectory optimisation

The cost function is defined on a four-dimensional grid, for which the climate cost values depend on longitude, latitude, altitude and time. This grid is integrated in the trajectory optimisation software

OpenAP-TOP (Sun, 2022). This trajectory optimiser is based on the aircraft performance program *OpenAP*, used to define model inputs for the different aircraft types in subsection 3.1.1. The built-in function of *OpenAP-TOP* `obj_fuel` is used to determine the fuel-optimal route of each flight. It does so by utilising the `enroute` function of the `FuelFlow` class in *OpenAP* to minimise the output of this function over the entire flight. The *OpenAP-TOP* function `obj_grid` can be used to integrate a cost grid into the optimisation and find the route that minimises the grid cost throughout the flight. For the current research, this objective contains the contrail climate cost grid calculated in *pycontrails* (see subsection 3.1.3) and the aCCFs of CO_2, NO_X, and H_2O, multiplied by the appropriate atmospheric variables (see subsection 2.3.1). All factors of the grid objective are provided in terms of $\mathrm{pK\,s^{-1}}$ according to the P-ATR20 climate metric. *OpenAP-TOP* requires the grid to be time-dependent for the trajectory optimisation to be independent the number of nodes used to partition the flight into flight segments.
A custom function that combines the fuel and climate costs is used to find the most optimal routes for a chosen set of function weights.

$$\texttt{obj\_total} = w \times \texttt{obj\_grid} + \frac{1}{w} \times \texttt{obj\_fuel} \tag{3.4}$$

The function weight w is varied between 0 and 1, depending on the case study. Flights with higher climate costs need higher weights to obtain results in desirable ranges. These weights are chosen to end up with an increase in fuel use of 0% to 3%, to remain within bounds of realistic trajectory optimisations.
The trajectory optimisation in *OpenAP-TOP* is based on the CasADi library. *OpenAP-TOP* provides several optimisation options, including the `Cruise` optimizer class which is used for this research. The function `nlpsol`, used to solve non-linear problems, defines the solver to be an interior-point optimizer, `ipopt` in short.
The solver is set up with the following state array:

$$\mathbf{x} = [x_p, y_p, h, m, t_s]$$

With x_p is the vector of projected longitudinal values, y_p projected latitudes, h the altitude, m the aircraft mass, and t_s the time step per node in the optimisation program. The control array is defined as

$$\mathbf{u} = [M, vs, \psi]$$

which includes the Mach number M, vertical speed vs and heading ψ. The latter is measured clockwise from the North.
Due to the complexity of the problem, the performance of the optimisation is increased by adjusting the solver options. New solver parameters are added to allow for a warm start of the solver: using information from previous runs with similar parameters to start at a point closer to the predicted optimal solution. This includes initial guesses for states, as well as solver-specific parameters. The initial guesses of the states are set equal to the previous trajectory. So the first run for weighted climate costs uses vectors in $\mathbf{x}$ and $\mathbf{u}$ from the fuel-optimal trajectory to start its solver. Furthermore, the solver's λ-values are passed to the next run to gain a warm start on the Lagrange multipliers for the bounds on $\mathbf{x}$ and $\mathbf{g}$, thus giving the solver even more information on the problem at hand. This approach shows significant improvements in finding near-optimal solutions compared to the original solver configuration. Despite the improvements in solver performance, the large solution space of the problem causes *OpenAP-TOP* to have trouble finding an optimal solutions for extra fuel usages higher than 0.1%. Most often, the maximum number of iterations is exceeded and the solver settles at a suboptimal solution. The results are filtered such that only suboptimal solutions that approach the optimal solution are included in the final results. This is done by filtering out all solutions that return a higher climate impact for a higher extra fuel usage compared to other data points. Due to the high number of data points found, the solutions that pass this filter are determined to be a good estimate of the optimal solution for their extra fuel usage. Therefore, it should be noted that the trajectory optimisation results presented in section 4.2 are estimates of optimal trajectories.

3.3. Choice of case studies

Before starting the contrail analysis and trajectory optimisation, four dates were selected for which there was an extensive presence of ISSRs causing many contrails to persist. For an even spread throughout

Figure 3.2: The fuel-optimal trajectories of the three different routes used for the case studies shown on a map of Europe. The numbers are included to link each route to the case studies in Table 3.3.

the year, accounting for different atmospheric and radiative variables, 20 February, 8 May, 3 September and 22 November 2023 were selected initially. However, shortly into the progression of contrail analysis and trajectory optimisation, it was decided to remove 8 May 2023 from the set of dates. The presence of ISSRs during this day was too low to obtain enough data on contrail formation to be used for trajectory optimisation. Disregarding 8 May in the remainder of this study is considered acceptable, as contrail formation and persistence throughout the other three dates vary significantly, thus providing a diverse selection of possible situations. These dates are evaluated for contrails that only exist either during the day or during the night.

To focus on the difference between the three aircraft types in contrail formation of individual flights, a flight is chosen from Amsterdam to Athens on 3 September 2023 departing at 19:00. This route and time are chosen such that the aircraft passes through a large ISSR and forms a persistent contrail with high radiative properties. As can be seen in Figure 3.1, the variance in ambient particle concentrations is not extremely high for this flight. For the comparison of contrail formation and persistence between the three aircraft types, this is beneficial, as there are fewer changes in variables to account for during the analysis of a difference in contrail properties. However, a different route should be chosen to be able to further investigate the impact of ambient particle concentrations on route diversions for hydrogen-powered flights. More on this is discussed in chapter 5.

All flights at night depart just after sunset, such that the entire life time of these contrails is between sunset and sunrise. This selection is made to investigate this type of contrail separate from contrails that exist during the day, as night-time contrails typically have a higher climate impact (Stuber et al., 2006).

The approximate fuel-optimal trajectories of the flights are shown in Figure 3.2. The specifics of each case study are listed in Table 3.3 for a concise overview.

Table 3.3: An overview of the case studies used in this report. The case studies cover three routes for two different departure times, to force the simulation of contrail formation for day-time and night-time contrails. The case studies are linked to the routes shown in Figure 3.2 through the numbers in the last column.

Route	Date	Time of departure (UTC)	Number on map
Amsterdam - Athens	3 September 2023	11:00	1
Amsterdam - Athens	3 September 2023	19:00	1
Stockholm - Alicante	20 February 2023	11:00	2
Stockholm - Alicante	20 February 2023	19:00	2
Antalya - Bergen	22 November 2023	11:00	3
Antalya - Bergen	22 November 2023	19:00	3

4

Results

The results presented in this chapter are instrumental in understanding the effect of the aircraft fuel on contrail properties, the increased role of ambient particles in contrail formation for hydrogen-powered flights, and the possibilities for trajectory optimisation strategies for these flights. The results are obtained by implementing the methods presented in chapter 3 and what they mean in the bigger picture of contrail climate impact, alternative fuels and trajectory optimisation, is discussed in chapter 5.
Section 4.1 dives into the results of contrail analysis in *pycontrails*, by showing the differences in contrail characteristics of different fuel types for a single flight and by comparing the two methods to use contrail analysis results for trajectory optimisation purposes. The results of the trajectory optimisation are presented in section 4.2. This section first covers the climate costs of the fuel-optimal routes of the three aircraft types, after which the trajectory optimisation results are shown. This chapter concludes with section 4.3, which analyses model inputs that carry significant uncertainties and how this potentially affects the results found during this research.

4.1. Contrail climate impact analysis

The methods described in section 3.1 are used to analyse a singular flight for the three aircraft concepts to observe the change in contrail characteristics, and to obtain data on contrail climate impact to be used for trajectory optimisation. The results are presented in this section.

4.1.1. Contrail characteristics of individual flights

The main differences between contrails for conventional aircraft and hydrogen-powered aircraft is the lack of soot particles and the increased water vapor content in the exhaust plumes of hydrogen-powered aircraft. The importance of these features is discussed in section 2.2. This review on current literature indicates that this difference is expected to mainly affect the number of ice crystals formed in the jet phase, and consequently the radius of these ice crystals. Therefore, *pycontrails* is used to analyse the evolution of these two contrail characteristics during the lifetime of a contrail. The results are shown in Figure 4.1. The values for the ice crystal mean radius are averaged per waypoint and are shown as dots in the top plot. The standard deviation of this value between waypoints is visualised by the error bars. The bottom plot shows the number of ice crystals. To show the effect of decreasing ice crystal numbers throughout all waypoints, the ice crystal number per m at each waypoint is multiplied with the segment length of that waypoint and summed together to obtain an estimate of the total number of ice crystals in the contrail. Taking the mean and standard deviation as done for the radius would not represent the total decrease in ice crystal numbers well. The first data points at $t = 0$ are taken after the initial downwash of the contrail. The results are obtained using an integration time step of 30 minutes.
The plots in Figure 4.1 are consistent with expectations for hydrogen: there are fewer ice crystals with larger radii in contrails produced by this aircraft type. The number of ice crystals of the SAF blend also decreases compared to Jet A-1, which can be expected by the decrease in fuel consumption and nvPM emissions listed in Table 3.1 and Table 3.2. The mean radius of the ice crystals is only slightly larger for the SAF blend than for Jet A-1. The ice crystal numbers of hydrogen decrease at a steeper rate than

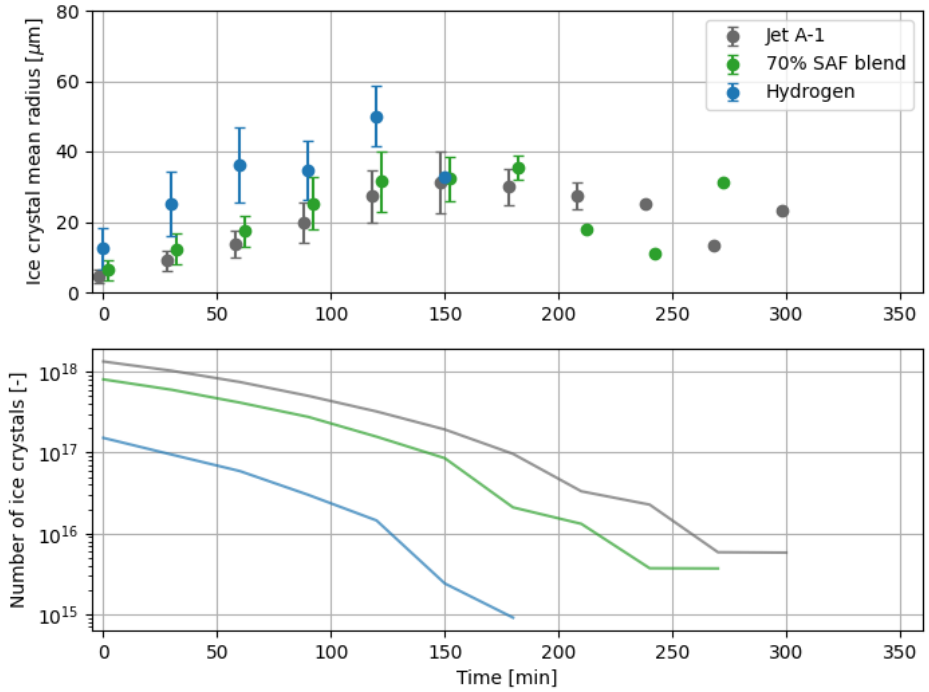

Figure 4.1: The mean volume radius of ice crystals (top) and number of ice crystals (bottom) throughout the lifetime of contrails formed by the current A320 aircraft model on Jet A-1, future aircraft model on a 70% SAF blend, and future hydrogen-powered aircraft model. Results found by use of the `CoCiP` model in *pycontrails* using a time integration step of 30 minutes. This contrail is generated on a flight from Amsterdam to Athens on 3 September 2023, departing at 19:00. Artificial spacing on the x-axis was added to show Jet A-1 and SAF separately, although the results are obtained at the same timestamp. The radiative forcing of the Jet A-1, SAF-blend and hydrogen-powered aircraft contrail is 1.68×10^{-8}, 1.05×10^{-8}, and 2.23×10^{-9} $\mathrm{W\,m^{-2}}$, respectively.

for the other fuels, completely nullifying after a lifetime of 3 hours. The contrail of the SAF-powered flight diminishes at 4.5 hours, and the Jet A-1 induced contrail has a lifetime of 5 hours.
The final point in the graph depicting the radius of the ice crystals formed by Jet A-1 and the SAF blend stands out as ice crystals in this stage generally reduce in size and sublimate after. The waypoint shown here increases in size. This is because the ice water concentration increases and the number of ice crystals strongly decreases, which leads to the addition of more ice on fewer nuclei.
To better understand the impact of the chosen aircraft model on the contrail radiative forcing, the values of the initial ice crystal number and radiative forcing are shown in Table 4.1. The former is chosen to show separately, as this contrail property has a high impact on the contrail radiative forcing according to the literature review in subsection 2.2.2. These properties are shown in absolute terms, and in terms

Table 4.1: The initial ice crystal number and total global mean radiative forcing of contrails formed by a conventional aircraft using Jet A-1, an improved aircraft using a 70% SAF blend, and a hydrogen-powered aircraft. The contrail properties are calculated in *pycontrails* for a flight from Amsterdam to Athens departing on 3 September 2023 at 19:00.

	Ice crystal number		Radiative forcing	
	Absolute [10^{17}]	Relative [%]	Absolute [10^{-9} $\mathrm{W\,m^{-2}}$]	Relative [%]
Jet A-1	13.4	100	16.8	100
70% SAF blend	8.05	60	10.5	63
Hydrogen	1.52	11	2.23	13

relative to the value of the reference Jet A-1 aircraft. These results can be used to better understand the reason for differences in contrail climate costs per fuel in the next parts of this report. How these results compare to findings in literature is discussed further in chapter 5.

4.1.2. Contrail analysis for trajectory optimisation

The first method to translate the contrail analysis output to useful data for trajectory optimisation involves analysing traffic data in *pycontrails* and using the resulting data points to find correlations and set up climate change functions. The other method focuses on directly cost grids in *pycontrails* that contain data on contrail climate impact and can be imported into trajectory optimisation software.

Correlations for climate change functions

The data in Figure 4.2a and Figure 4.2b shows the radiative forcing values per km contrail for Jet A-1 and hydrogen, respectively. Both plots use the same input data set, described in subsection 3.1.3. The data points are obtained from running each flight in this traffic data set through the `CoCiP` model in *pycontrails*. Meteorological and radiation data of 3 September 2023 is used. For Jet A-1, there are a total of 46,000 contrail segments found with a non-zero radiative forcing, distributed over more than 2,600 flights. The simulations with hydrogen-powered aircraft result in 69,000 non-zero data points from 3,500 flights. Each flight that produces useful data points typically forms one to three distinct contrails.

In order to form a climate change function, correlations must be found between the radiative forcing and atmospheric variables on the horizontal axes. From Klingaman and Shine (2023), it follows that the highest correlations should be with temperature and outgoing longwave radiation. Therefore, the data points resulting from the runs in *pycontrails* are compared to these two variables. For hydrogen-powered aircraft, a strong correlation can be expected with the number concentration of ambient particles (see subsection 2.2.2). This variable is thus added to the correlation analysis for hydrogen-powered aircraft. Note that the variables used to find correlations are at the contrail onset: variation due to contrail movement through the atmosphere during its lifetime are not taken into account. Figure 4.2a and Figure 4.2b show little correlation. The strongest correlations for Jet A-1 are with T ($R = 0.037$ during the day, $R = 0.34$ during the night). For hydrogen, the highest correlations are with OLR during the day ($R = 0.19$), and with T during the night ($R = 0.35$). The latter is obtained with an exponential fit; the other R-values are found using a linear fit.

These correlations are found to be too weak to be used for setting up algorithmic climate change functions. The visualisations in Figure 4.2a and Figure 4.2b support this. For most values of T, OLR, and n_a (only for hydrogen), a wide range of RF values is possible with similar probabilities. Especially as these plots only apply to one date (3 September 2023), stronger correlations should be found to use this method for accurate contrail radiative forcing calculations. Therefore, these results are not used for trajectory optimisation purposes, and the focus is shifted to the alternative method of obtaining contrail climate impact results: producing grids directly through contrail analysis.

Contrail cost grids

The grids containing the contrail climate impact are produced for the three dates mentioned in section 3.3. The grids for the fuels are shown in Figure 4.3 on 3 September 2023 to visualise the difference in grids between the fuel types used for trajectory optimisation. The values shown in the cost grids signify the climate costs of contrails formed at that point in time. Note that the colourbar scale is not linear: this distribution of values is chosen to use one scale for all graphs and thus allow for direct comparison between the climate costs. The values are expressed as $\mathrm{pK\,s^{-1}}$. This unit is chosen to allow for direct integration into *OpenAP-TOP*, which requires a grid with climate costs over time. The software multiplies these values by the timestep of the solution to obtain the P-ATR20 cost in pK. The grids shown in Figure 4.3 are at an altitude of 10 km at 12:00 and 20:00. This constant altitude is chosen to showcase the relative differences in contrail climate impact between the fuels, even though the fuel-optimal cruise altitudes between the aircraft models differ from this constant altitude. The times at which the grids are shown are 1 hour after the departures of the case studies, listed in section 3.3. The changes in climate costs with altitude and time are shown in the flight analyses later in this chapter. The main takeaway from these visualisations is that the pattern of atmospheric regions for contrail formation are similar, but that the magnitude of climate impact decreases when using SAF and hydrogen.

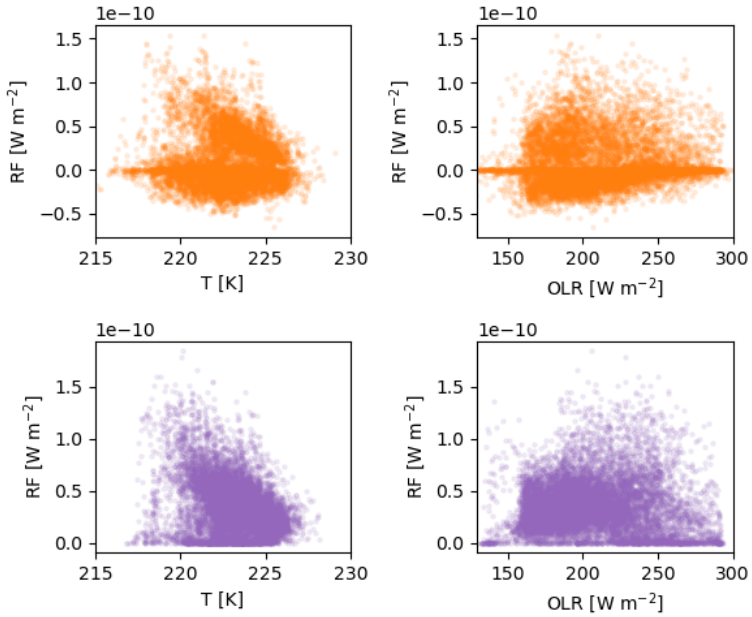

(a) Global mean radiative forcing per km contrail of contrails formed by kerosene-powered aircraft versus temperature and outgoing longwave radiation. The bottom plots are contrail segments that exist only when the sun is down, thus producing solely positive RF values. The top plots consist of data points of contrail segments that exist completely during the day and partially during the day and night.

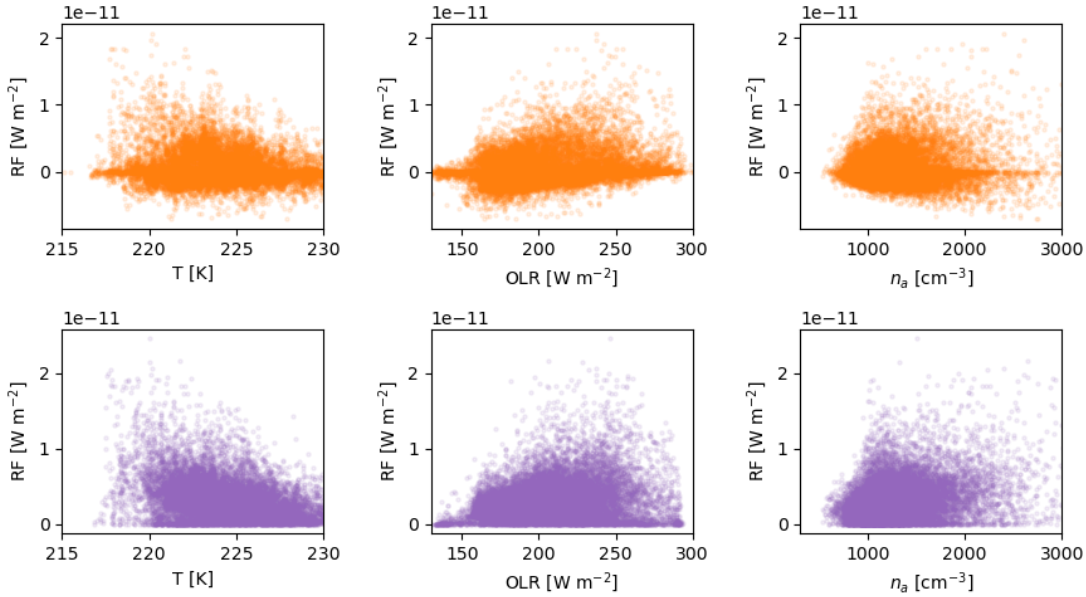

(b) Global mean radiative forcing per km contrail of contrails formed by kerosene-powered aircraft versus temperature, outgoing longwave radiation, and ambient particle concentrations. The top plots (orange) consist of data points of contrail segments that occur (at least) partially during the day. The bottom plots are contrail segments that exist only when the sun is down, thus producing solely positive RF values.

Figure 4.2: Correlations of contrail radiative forcing for Jet A-1 and hydrogen with atmospheric variables.

4.2. Trajectory optimisation

The cost grids resulting from the contrail analysis in the previous section can be used for trajectory optimisation. First, in subsection 4.2.1, the climate costs of the fuel-optimal flights are presented, after which the climate impact decreases that result from trajectory optimisation are shown in subsection 4.2.2.

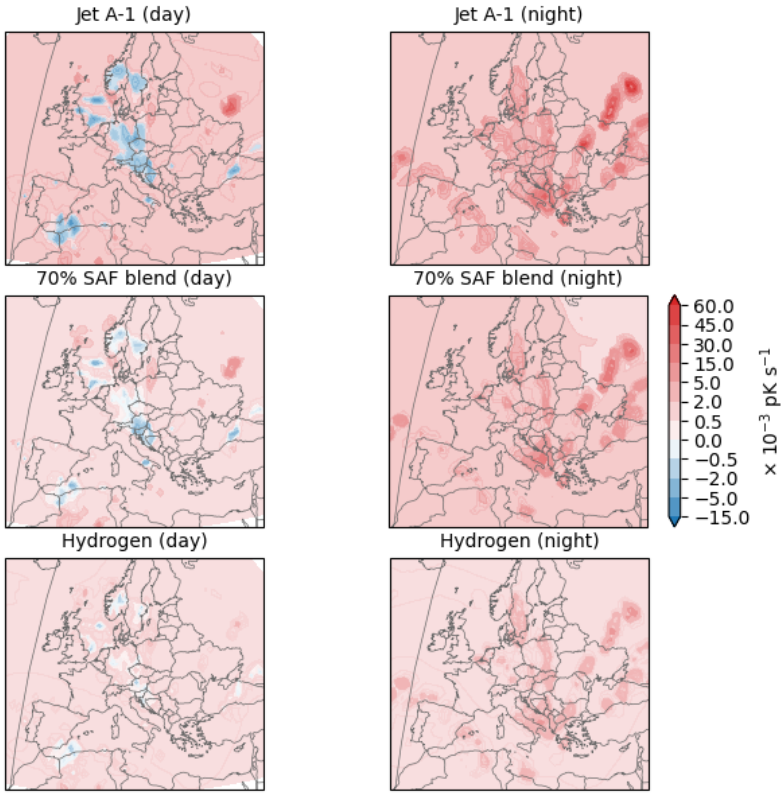

Figure 4.3: Cost grids on 3 September 2023 during the day (left) and the night (right) for Jet A-1 (top), a 70% SAF blend (middle) and hydrogen (bottom) as fuel types. The scale of the colour mapping differs per fuel due to the large differences in climate cost magnitudes. The cost grids are generated for a cruise altitude of 11 km.

4.2.1. Climate impact of fuel-optimal routes

Before analysing trajectory optimisation opportunities to decrease the climate impact, it is important to determine the base values of the different climate impact factors, i.e. CO_2, NO_X, H_2O and contrails, for the fuel-optimal routes. The contributions of these factors are shown in Figure 4.4. The absolute values for the P-ATR20 metric of all emissions are shown in the top figure, and the bottom figure of Figure 4.4 is added to show the smaller differences more clearly on a logarithmic scale..

Figure 4.4 provides a complete overview of the contribution of each climate effect to the total climate impact of every aircraft model and every case study. The supplementary bar plots provided in Figure A.1 show the relative differences in total climate impact between the fuel more clearly. This figure shows a typical climate impact decrease of 80% to 90% for the hydrogen-powered aircraft compared to its Jet A-1 counterpart. The improved aircraft using a 70% SAF blend results in a climate impact decrease of 2% to 60% compared to the conventional aircraft type.

There is one scenario for which the climate impact of a hydrogen-powered flight is higher than that of a flight on Jet A-1 on the same route. This can be explained by a negative offset of the Jet A-1 climate impact due to contrail persistence in cooling regions. This is shown in first case study in the top part of Figure 4.4 by the cross on the negative y-axis and visualised by the blue regions in the top-left part of Figure 4.3. These negative values make bar plots for this case study unclear. Therefore, it is left out of Figure A.1.

The high variations in climate impact decrease is accounted for the difference in mission profiles of the aircraft models. Appendix B showcases the fuel-optimal routes of the aircraft types on each trajectory in grey, and the route for a relatively small diversion corresponding to different values of fuel increase in black. The extra fuel usage per visualisation is specified in the caption of each figure. The top plots show the horizontal deviations, the middle ones show the changes in altitude, and the bottom plot shows the velocity change throughout each flight. The different aircraft specifications discussed in subsection 3.1.1 cause the fuel-optimal trajectories to vary strongly between the fuel types. Appendix B show that hydrogen-powered aircraft fly significantly lower than the other aircraft types and that there

is also a slight difference in optimal cruise altitude between Jet A-1 and the improved aircraft using the SAF blend. Even though the latter difference is smaller than the former, it does have a larger effect as contrails contribute more to their total climate impact.
To assess the relative difference in contrail climate impact disregarding differences in cruise altitudes, the contrail climate impact of the SAF blend and hydrogen are calculated on the fuel-optimal route of an aircraft powered by Jet A-1. The results are consistent with the findings on single-flight contrail formation discussed in subsection 4.1.1: for the night flight of Amsterdam to Athens on 3 September 2023, the contrail climate impact of SAF used in an improved aircraft is 62% of that of Jet A-1, and the climate impact of hydrogen-induced contrail is 19% of the Jet A-1 value. Other case studies show a relative value of $37 - 62\%$ for SAF and $5 - 20\%$ for hydrogen. In terms of total climate impact, the case studies show that the climate impact of the SAF blend is $40 - 65\%$ of that of Jet A-1 when these aircraft fly the same route. The hydrogen-powered aircraft forces $10 - 25\%$ of the climate impact of the Jet A-1 flight. This excludes the first case study, with the strongly cooling contrail, for which the relative climate impact of the alternative aircraft models compared to Jet A-1 is 97% and 71% for the SAF blend and hydrogen, respectively.
For trajectory optimisation, it is important to understand the relative climate impact of contrails for each aircraft model compared to the other climate effects. Trajectory optimisation through contrail avoidance is only effective when contrails are responsible for a large fraction of the total climate impact of an aircraft. To obtain a better view of the relative importance of contrails per aircraft model, the contribution of each climate effect per aircraft type relative to its total climate impact are visualised in Figure A.2. Again, the case study Amsterdam-Athens during the day is excluded as it cannot be clearly visualised due to the cooling climate effects. From these plots, it becomes clear that the relative contribution of

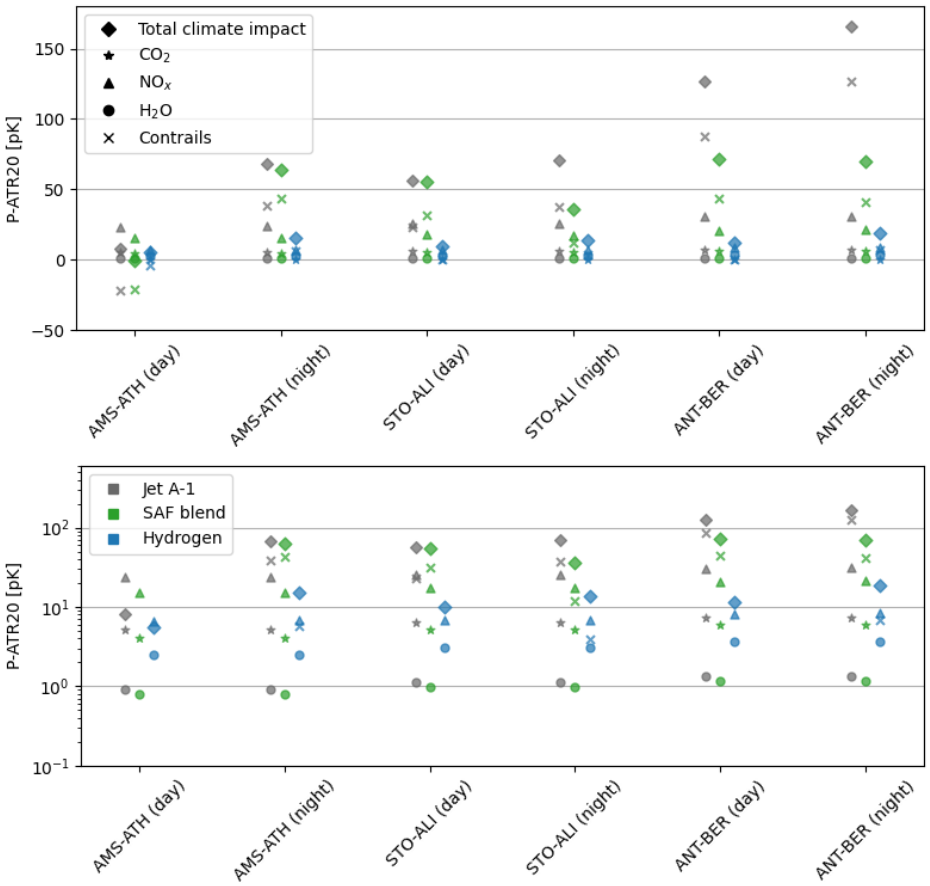

Figure 4.4: Normalised contributions of climate impact factors per fuel type per case study. The x-axis shows the case studies Amsterdam - Athens, Stockholm - Alicante, and Antalya - Bergen during the day and night. The bottom graph shows the positive values of the top figure on a logarithmic scale to more clearly show the difference between the low-impact emissions of each fuel. Note that the bottom figure does not include the cooling contrails of the first case study.

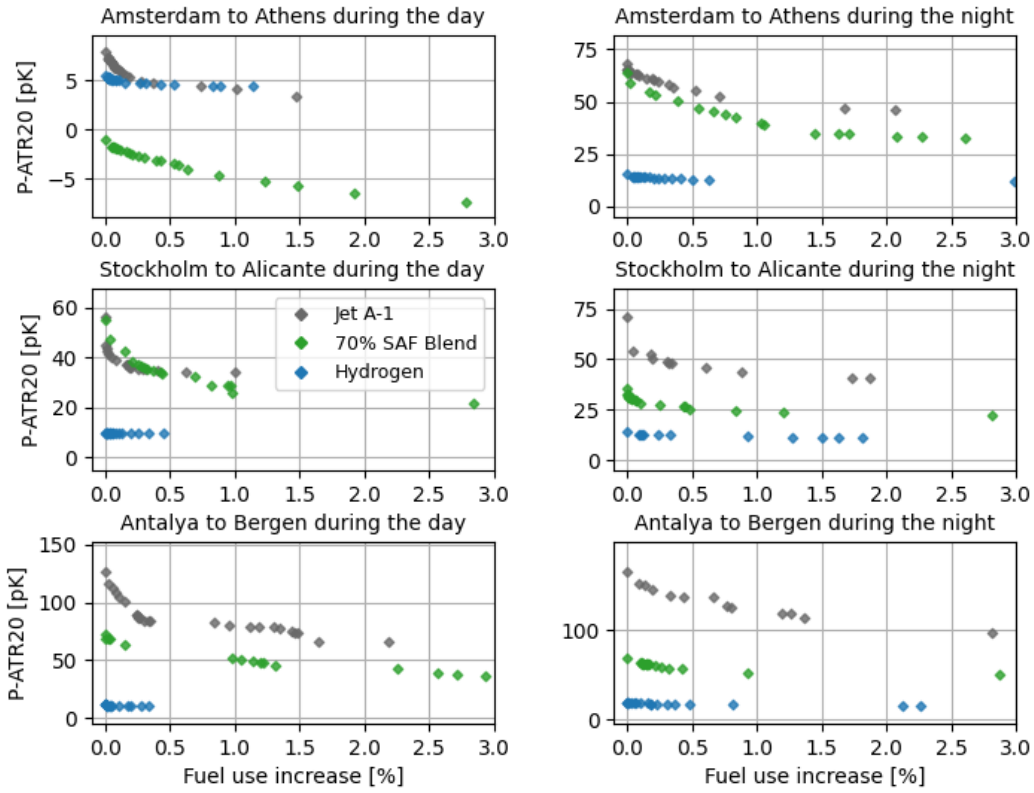

Figure 4.5: Climate costs of trajectory optimisation possibilities in terms of relative increased fuel usage. Results are shown for conventional aircraft powered by Jet A-1 (grey), conventional aircraft in the future powered by a 70% SAF blend (green) and hydrogen-powered aircraft in the future (blue). The trend lines shown for the different fuel types are based on the dots of the same colour.

contrail climate effects of hydrogen-powered aircraft is lower than for the other aircraft models. Whereas contrails force $41-76\%$ of the total climate effects, this relative contribution reduces to $34-68\%$ for the 70% SAF blend and $0-38\%$ for hydrogen-powered aircraft.
To show the impact of the choice of climate metrics on the base climate costs, the bar plots for the base climate costs in Appendix A are also shown for F-ATR100. Figure A.3 shows that the decrease in climate impact when using SAF and hydrogen is less significant when using the F-ATR100 metric for case studies with a high contrail climate impact. The relative contribution of contrails compared to other climate effects per aircraft model is lower when using the F-ATR100 metric instead of P-ATR20, as shown in Figure A.4. This indicates that examining trajectory optimisation strategies for F-ATR100 provides less opportunities than for P-ATR20.

4.2.2. Climate impact reduction through trajectory optimisation

Figure 4.4 shows the climate costs for the fuel-optimal routes of the six case studies. The total climate impact and the ratio of all contributing factors can be changed through trajectory optimisation. As the case studies are specifically chosen for high climate-impact contributions of contrails, the trajectory optimisation is primarily focused on avoiding ISSRs. The trajectory optimisation is carried out according to the methodology described in section 3.2 and the results are presented in Figure 4.5.
Jet A-1 and SAF both show significant potential to reduce the climate impact at each of the chosen case studies. In terms of absolute climate cost reductions, route diversions for climate impact reduction is least effective for the case study shown in the top-left of Figure 4.5. The other case studies show reductions of approximately $25-50$ pK for Jet A-1 within the first 2% of extra fuel usage, and approximately $10-30$ pK for the 70% SAF blend. Independent of the case study, Figure 4.5 clearly

shows that trajectory optimisation for hydrogen-powered aircraft barely decreases the climate impact of these flights. The method by which the data in Figure 4.5 is prepared (see section 3.2), ensures that all points with a higher fuel usage signify a decrease in P-ATR20. This means that the hydrogen-powered aircraft trajectory optimisation yields lower climate costs, but the plots show that these decreases are negligible.
The large gaps on the horizontal axes in Figure 4.5 indicate fuel usages for which the trajectory optimiser does not converge. This indicates that for these values of fuel increase there are no routes available that decrease the climate costs compared to lower fuel increases. One case study that shows this behaviour is the bottom-left plot in Figure 4.5. For Jet A-1, there are no datapoints available between fuel usage increases of approximately $0.4 - 0.8\%$. The same goes for the SAF blend between approximately 0.2 and 1%. The inability of the solver to find routes with lower climate costs than for lower fuel usages is also visible for hydrogen. The mid-left and bottom-left plot show that the most optimal route within this range of extra fuel usage is found at a fuel usage increase of $< 0.5\%$, concluded from the lack of datapoints beyond this value.

Mission profiles

As mentioned in subsection 4.2.1, the different mission profiles between the aircraft types considered have a high impact on the climate costs of the fuel-optimal flights. It also affects the possibilities of trajectory optimisation. This is visualised well in some of the trajectories shown in Appendix B. The flight from Stockholm to Alicante during the day with the three aircraft types shows the difference in trajectory optimisation for different cruise profiles. The fuel-optimal route of the SAF-powered flight travels straight through an ISSR, as shown in Figure B.8. This results in possibilities for trajectory optimisation for a large range of extra fuel usages, as it would require a lot of extra fuel to completely avoid the ISSR. This can be observed in Figure 4.5 by the high number of datapoints for a large range of fuel usage increases. The flight on Jet A-1 in Figure B.7 only crosses smaller parts of this ISSR, leading to fewer trajectory optimisation opportunities to decrease its climate impact. This leads to fewer datapoints in the top-right figure of Figure 4.5 for Jet A-1. The hydrogen-powered flight in Figure B.9 does not cross the ISSR at all. Therefore, little climate impact reduction is possible through trajectory optimisation.

Net-cooling contrail regions

The case study shown in the top-left of Figure 4.5 passes through regions where the contrails formed have a net-cooling effect. The trajectories for this flight are shown in Figure B.1, Figure B.2, and Figure B.3 for Jet A-1, the 70% SAF blend, and hydrogen, respectively. These figures, showing the trajectory optimisation for the extra fuel usage mentioned in the captions, show that these net-cooling regions can be exploited to decrease a flight's climate impact even further. The top-left plot in Figure 4.5 shows that this can lead to a net-cooling effect of all climate impact factors combined, shown by the negative P-ATR20 values for the SAF flight. The presence of regions that cooling contrails of such magnitude are very rare, as found by Wilhelm et al. (2021). Therefore, even though it is interesting to see this effect in one of the case studies, it can be considered an outlier in research into trajectory optimisation for contrail avoidance.

Rate of decrease in climate costs

This rate of decrease in climate costs is an important measure in determining for what flights it would be worth it to perform route diversions. Some reductions in P-ATR20 for low extra fuel usages are steep (Stockholm-Alicante during the night, mid-right in Figure 4.5), while other case studies show a more gradual reduction in climate cost reductions over a larger range of extra fuel usages (Amsterdam-Athens during the night, top-right in Figure 4.5). The former is more interesting for real-world implementation, as airlines prioritise minimising their fuel usage. Comparing this behaviour between the different fuels, Jet A-1 shows the steepest decreases in climate costs. The SAF blend generally shows more gradual decreases in climate costs for low fuel use increases. Figure 4.5 shows more data points for SAF at higher fuel usage increases, indicating more climate cost reduction opportunities at higher fuel increase levels. This is less useful for real-world implementation because airlines prefer to minimise their extra fuel usage.
Translating these extra fuel usages to monetary costs poses more problems for trajectory optimisation with future fuels. Section 2.3.2 discusses the state-of-the-art predictions on hydrogen fuel costs. Three

predictions are shown: an optimistic case, for which fuel costs would be lower than the current price for Jet A-1, a base case and a pessimistic case. Due to the low climate impact decrease of hydrogen-powered flight optimisations, route diversions have an extremely high cost-to-yield ratio for any of these pricing scenarios compared to route diversions with Jet A-1 and SAF. Furthermore, as the current price for SAF is three times that of Jet A-1 (IATA, 2023), it is likely that flights with the 70% SAF blend would also cost significantly more to divert than Jet A-1 flights.

4.3. Sensitivity analysis

The current research contains parts that include major uncertainties. It is important to assess the effect of the assumptions made during this thesis and analyse results for alternative model inputs. Section 4.3.1 focusses on the trajectory optimisation results for different hydrogen-powered aircraft characteristics, covering the potential of higher and lower technological advancements in this area. The effects of uncertainties regarding ambient particle number concentrations and the magnitude of contrail climate impact are analysed in subsection 4.3.2 and subsection 4.3.3, respectively.

4.3.1. Hydrogen-powered aircraft characteristics

At the time of conducting the current research, all characteristics of hydrogen-powered aircraft and engines are based on theoretical models. The coming years are set to change our understanding of this future aviation technology through testing, which could prove this type of aircraft to be either better performing or worse than what is currently believed. Therefore, the effect of these two situations on the current results is analysed.

The situation for which hydrogen-powered aircraft prove to be more efficient than currently thought is defined as an 11% decrease in energy usage compared to the baseline hydrogen-powered aircraft model, assuming the same flight time. This change includes a decrease in OEM and fuel flow and an increase in overall propulsion efficiency, as shown in Table 4.2. The other extreme considers an 11% increase of total energy usage for the same mission. The parameters of the two altered hydrogen-powered aircraft concepts and the original one are shown in Table 4.2. These values are determined using *OpenAP*.

The results for trajectory optimisation are shown in Figure 4.6. Note that the vertical axis does not extend to 0, contrary to other figures in this report. The reason for this is that the changes in P-ATR20 values is so small for the differences in technology perspective that it is best presented on a smaller range of P-ATR20 values.

The results in Figure 4.6 can be explained by considering the impact of the technology changes on the aircraft's mission profile. Figure B.19 and Figure B.20 show an approximate difference in cruise altitude of 1500 m. Similar to differences in climate impact between Jet A-1 and hydrogen-powered aircraft (see subsection 4.2.1), this difference has a large effect on the climate impact of the fuel-optimal case. In this case study, the aircraft with the pessimistic view flies low enough to avoid the largest part of the ISSR on its fuel-optimal trajectory. This is the reason that its climate impact in the fuel-optimal case is even lower than that of the baseline case, despite the increase in fuel mass flow. It also explains the limited trajectory optimisation strategies shown in Figure 4.6.

The cruise altitude of the optimistic case is higher than that of the baseline case, which causes more contrail formation and thus a higher total climate impact of this aircraft type. It also means that this flight offers trajectory optimisation opportunities for a higher range of extra fuel usage values, as it has

Table 4.2: Hydrogen-powered aircraft parameters for the sensitivity study. There are two additional aircraft concepts: one case that is more optimistic on the progress of hydrogen technologies for aerospace applications, where the overall propulsion efficiency increases, and a case which assumes less progress in this technology causing it to be less efficient. The values are determined using the aircraft performance program *OpenAP* (Sun et al., 2020).

Values	Optimistic H_2 concept	Baseline H_2 concept	Pessimistic H_2 concept
Take-off mass [kg]	$68,000$	$70,600$	$73,000$
Fuel mass flow [$\mathrm{kg\,s^{-1}}$]	0.24	0.27	0.30
Overall propulsion efficiency [-]	0.38	0.35	0.32

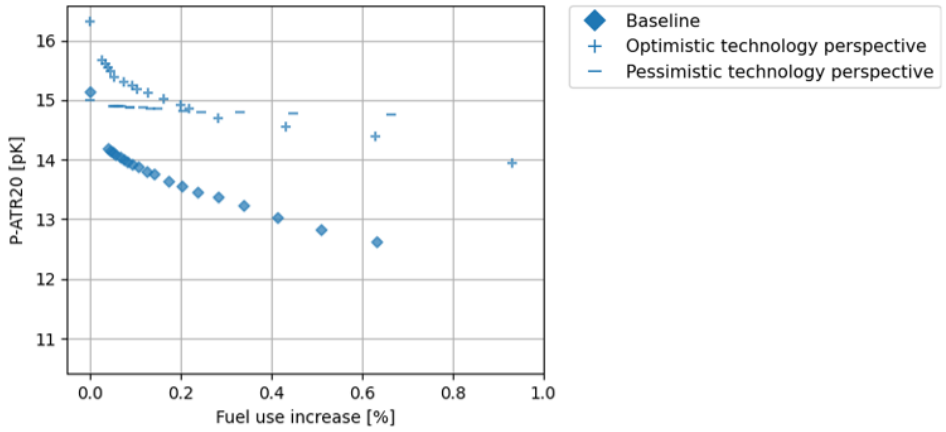

Figure 4.6: Trajectory optimisation strategies for hydrogen-powered aircraft with a pessimistic (-) and an optimistic (+) view on technological advancements. Both views are compared to the baseline technology scenario used for the current research. The different technology scenarios assume changes in aircraft mass, fuel mass flow, and overall propulsion efficiency.

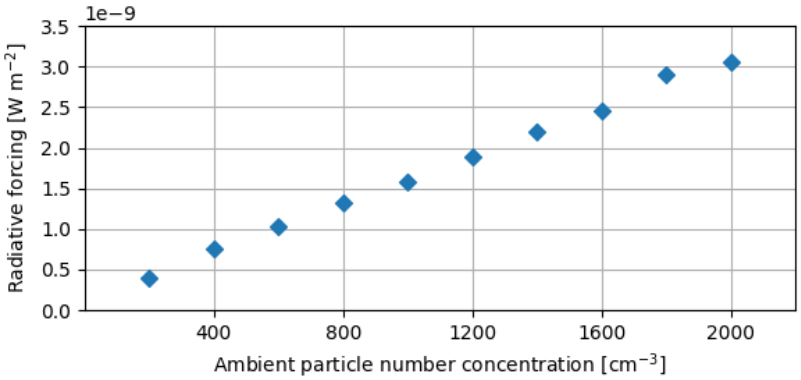

Figure 4.7: The global mean radiative forcing of the contrail formed by a hydrogen-powered flight from Amsterdam to Athens on 3 September 2023. The ambient particle concentration is set at a constant value throughout the flight and all particles entrained into the exhaust plume in the first 1.5 s are water-activated.

a larger part of the ISSR to avoid. This is indicated shown by the trajectory optimisation opportunities at higher fuel use increase values for the optimistic case in Figure 4.6.

4.3.2. Ambient particle number concentrations

Current literature focuses on contrail formation on ambient particles with a constant number concentration. Bier et al. (2024) choose a value of $600\ \mathrm{cm}^{-3}$. However, as described in chapter 3, local variations in number concentrations are included in this report, mainly to account for the differences with altitude described by Minikin et al. (2003). Also, the median value is chosen to be higher than $600\ \mathrm{cm}^{-3}$, also consistent with Minikin et al. (2003) for common cruise altitudes. However, it is interesting to assess to what extent these variations in choices for ambient number concentrations impact the current results.
The case study for the single flight in subsection 4.1.1 is performed for constant values of ambient particle number concentrations. The results are shown in Figure 4.7. The hydrogen-powered aircraft contrail RF of 2.23×10^{-9} in subsection 4.1.1 corresponds to a number concentration of about $1300\ \mathrm{cm}^{-3}$.
The continuous increase in radiative forcing for higher values of ambient particle concentrations indicates that the assumption of ambient number concentrations highly affects trajectory optimisation for hydrogen-powered aircraft. Thus, two alternative scenarios are investigated: one for which the mean number concentration is lower, consistent with Bier et al. (2024), and one where it is higher. The new mean values for the ambient particle number concentration are approximately 600 and $2000\ \mathrm{cm}^{-3}$, respectively. The relative changes of number concentrations with respect to the mean value, as explained

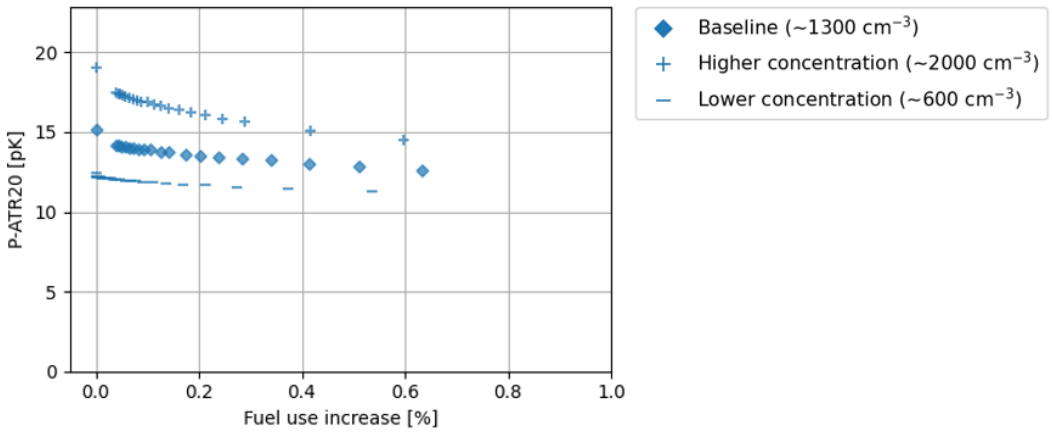

Figure 4.8: Trajectory optimisation for different ambient particle number concentrations. The mean value of the ambient particle number concentration is shifted to 600 and 2000 cm^{-3} to observe the behaviour of trajectory optimisation opportunities for lower and higher number concentrations. The same relative deviations from the mean number concentration is preserved as for the dataset generated for the baseline case, described in subsection 3.1.1.

in subsection 3.1.1, are preserved. The impact of these alternative values on trajectory optimisation is shown in Figure 4.8. This figure indeed shows a significant change in P-ATR20 with a change in ambient number concentrations. It is interesting to see that trajectory optimisation causes the P-ATR20 values of the different scenarios to approach each other as route diversions are most beneficial for the scenarios in which the radiative forcing of contrails is highest.

4.3.3. Magnitude of contrail climate impact

As determined in the literature review on contrails (see section 2.1), there is great uncertainty in determining the contrail climate impact. Lee et al. (2021) estimate the $5-95\%$ confidence interval to cover effective radiative forcing values of 30% to 170% of the best estimate. To explore the effect of this uncertainty, the cost grids of contrail climate impact are multiplied by 0.3 and 1.7. This multiplication is performed on the contrail cost grids used for trajectory optimisation. The results are shown in Figure 4.9.

The results of this case study are as expected: a higher magnitude of contrail climate impact equals more potential for trajectory optimisation. This can be concluded from the converging lines in Figure 4.9: the climate impact of the fuel-optimal route are significantly far apart, and come closer together for higher fuel increase levels. The absolute impact of this the change in contrail climate impact magnitude is smallest for hydrogen-powered aircraft, due to the reduced climate impact significance of contrails in its total climate impact as discussed in section 4.2.

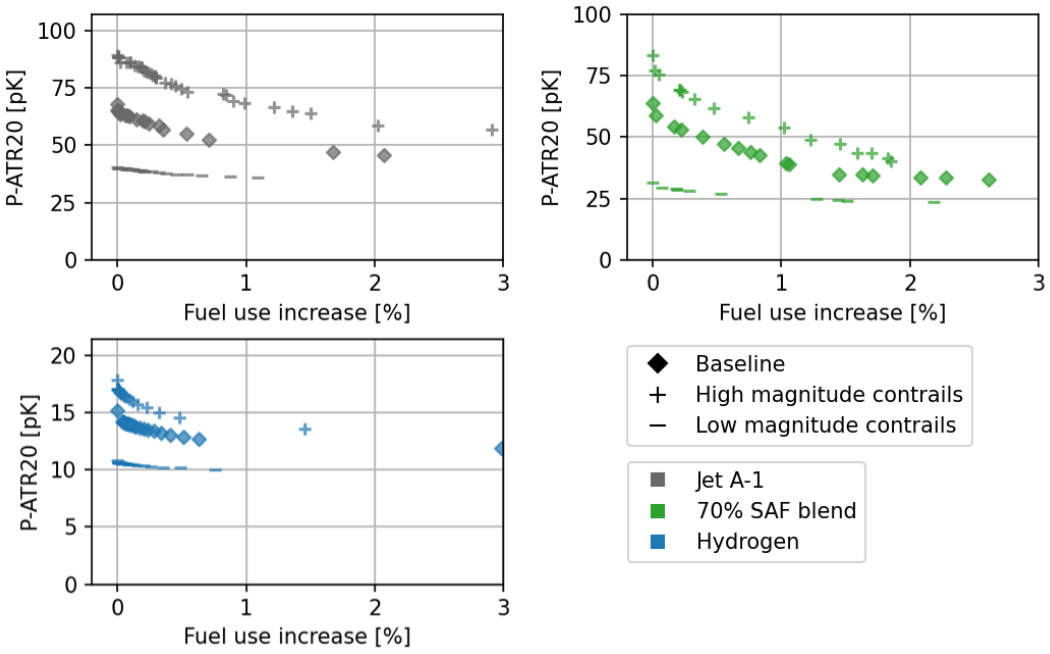

Figure 4.9: Trajectory optimisation results for the flight from Amsterdam to Athens on 3 September 2023 departing at 19:00 for three contrail climate impact scenarios. The diamonds indicate the total climate impact as calculated in *pycontrails* using `CoCiP-grid`, the (+)-symbols show the trajectory optimisation opportunities if the climate impact magnitude would be 70% higher, and the (-)-symbols show the trajectory optimisation for a climate impact decrease of 70%. The colours are consistent with the rest of the report: grey visualises the climate impact for current aircraft powered by Jet A-1, green is future aircraft powered by a 70% SAF blend, and blue is a future aircraft powered by hydrogen.

5 Discussion

The results presented in this research adds to our understanding of trajectory optimisation for contrail avoidance and hydrogen-powered flight operations. This chapter discusses how the current research what factors have limited the current research in section 5.1. Section 5.2 dives into recommendations for further research.

5.1. Limitations

The current research strongly depends on the methods that were available at the time of conducting this research. This section identifies the main limitations that this research faces and what it could mean for the results presented in this report.

5.1.1. Challenges in contrail modelling for hydrogen-powered aircraft

As this research mainly focused on trajectory optimisation, contrail modelling for hydrogen-powered aircraft is mainly performed using existing software. However, some critical aspects of contrail formation by this aircraft type are not included in *pycontrails*. The most important ones, and what this means for the results presented in this thesis, are discussed below.

Impact of vPM emissions

As there is very little knowledge on the expected vPM emissions from hydrogen-powered aircraft, as well as their role in the contrail formation process in the absence of soot, this topic is particularly difficult to research at the moment. Bier et al. (2024) point this out as well, stating that the vPM emissions of hydrogen-powered aircraft could even cause the radiative forcing of the resulting contrails to exceed that of contrails formed by conventional aircraft. Further research into this topic should be prioritised to better understand the climate impact of hydrogen-powered aircraft.

Varying ambient particle number concentrations

The importance of ambient particle concentrations for contrail formation of hydrogen-powered aircraft has been highlighted by Bier et al. (2024) and is discussed in section 2.2. It would be interesting to investigate the role of variations in ambient particle number concentrations, in order to better understand its role in hydrogen-powered aircraft contrail formation and trajectory optimisation strategies. This part of the research was limited by the absence of datasets for ambient particle concentrations that play a role in contrail formation. As an alternative approach, custom ambient particle concentration data sets were generated in order to account for changes of concentrations for different altitudes as presented by Minikin et al. (2003), and local maxima and minima were added to be able to analyse the impact of these variations on trajectory optimisation.

The impact of these variations was not investigated further, as the effect of trajectory optimisation for hydrogen-powered aircraft was found to be negligible. However, similar research should be carried out once applicable datasets on ambient particles are published, especially if these datasets show higher number concentrations than the values found by Minikin et al. (2003). This would result in higher contrail climate impact values for hydrogen-powered aircraft, and thus more trajectory optimisation

opportunities. This would invite more research into trajectory optimisation based on local variations in ambient particle number concentrations as well.

Ice crystal sizes and their effects

As presented in subsection 4.1.1, one of the main differences between the contrails formed by the three aircraft types discussed in this report, is the mean size of the ice crystals. The main effect of a higher ice crystal size in the `CoCiP` model in *pycontrails* is an increase in terminal velocity that leads to earlier sedimentation of ice crystals, and subsequentially to a shorter contrail life time. However, there are more intricate effects that are also interesting to include. The role of the Kelvin effect, for example, is more significant when a contrail contains larger ice crystals (see subsection 2.2.2). Using simplifications for these types of physical phenomena could prove to yield less accurate results when simulating contrails from hydrogen-powered aircraft.

5.1.2. Exclusion of air traffic in contrail climate impact calculations

The cost grids generated by `CoCiP-grid` in *pycontrails* calculate the climate impact of contrails formed by individual flights that cross the grid. However, literature suggests that the impact of simulating single flights instead of flight traffic is significant. This becomes clear when comparing the results found in the current study regarding the number of ice crystals formed with the contrail radiative forcing.

The first results in chapter 4 show that the total number of ice crystals drops by 40% when replacing the current aircraft powered by Jet A-1 with the future aircraft powered by a 70% SAF blend. Using hydrogen instead of Jet A-1 decreases the initial ice crystal number by 89%. Burkhardt et al. (2018) find that the relation between the number of ice crystals formed in a contrail and the global radiative forcing is not linear. Their results show that a 50% decrease in ice crystal number reduce the radiative forcing by only 20%. A reduction of 90% of the ice crystal number causes a radiative forcing decrease of 70%.

The results presented in subsection 4.1.1 are not consistent with these findings. The decrease in ice crystal number due to the use of SAF of 40% corresponds to a decrease in contrail radiative forcing of 37%. The hydrogen-powered aircraft causes an ice crystal number reduction of 89% and a reduction in radiative forcing of 87%. These results appear to approach the linear relation that Burkhardt et al. (2018) dispute.

It can be shown that this difference between current findings and literature is at least partially related to the other differences between the aircraft types. The varying fuel properties, for example, cause a significant difference in the critical temperature for the Schmidt-Appleman criterion explained in section 2.1. The initially formed ice crystal number calculation strongly depends on this temperature. Depending on local ambient conditions per flight stage, the critical temperature for the flight on Jet A-1 is 222.5 to 226 K. The critical temperature for the SAF flight is generally 1.5 degrees higher, at 224 to 227.5 K, and the critical temperatures for hydrogen-powered flights are between 232 and 238 K. This large difference for the latter compared to Jet A-1 is consistent with Figure 2.4. This change in critical temperature does not highly affect the radiative forcing, but it does affect the initial number of ice crystals formed. Other characteristics of the aircraft types that could impact this number are the water vapor emissions and aircraft weight, both impacting the survival fraction of ice crystals during the jet phase if calculated by the relation presented by Unterstrasser et al. (2008).

To check whether these differences in aircraft characteristics are the reason that the results presented in this research deviate from Burkhardt et al. (2018), the number of nvPM emissions for the Jet A-1 flight was overridden, keeping all other aircraft properties the same. This leads to the relation between number of ice crystals and RF to become non-linear, as expected, but still numbers deviate from literature. Where Burkhardt et al. (2018) find a 20% decrease in RF for a 50% decrease in ice crystal number, this new method in *pycontrails* find a 40% decrease in RF for the same decrease in initial ice crystal number. Burkhardt et al. (2018) mention that simulating contrail persistence in high-density flight traffic areas yields results that significantly differ from areas in which only few aircraft fly. This has to do with the reinvigoration of old contrail cirrus by newly formed ice crystals in areas with a lot of traffic. In their simulations, a decrease of 80% in ice crystal formation causes the radiative forcing of contrails to decrease by less than 50% in high-density traffic areas and 70% in areas with fewer flights. The latter is in line with the range of values found with *pycontrails* when overriding the nvPM emissions of Jet A-1. Future research should be extended to include the effect of traffic density on the climate cost reduction that can be realised by performing trajectory optimisation.

5.1.3. Exclusion of in-flight emission changes

The method that is used to calculate the climate impact of all in-flight emission types is based on a grid generated before the trajectory optimisation process, thus not allowing for changes in flight performance characteristics to change the emission values. As a result, constant values are assumed for the fuel flow, overall propulsion efficiency, NO_X emission index and the nvPM emissions.

As the `CoCiP-grid` model in *pycontrails* is used to generate a grid prior to trajectory optimisation, which rules out the possibility of directly including in-flight emission changes in contrail climate impact calculations. For NO_X, *OpenAP-TOP* has a function to calculate the emissions in $\mathrm{g\,s^{-1}}$ while including performance alterations due to trajectory optimisation. However, this method is not included in the current research, as this function is only available for aircraft fuelled by Jet A-1. Modelling changes in NO_X emissions with changes in flight performance for SAF and hydrogen is considered outside the scope of the current research. Furthermore, treating NO_X the same as contrails with regard to in-flight emission changes is considered the best option for consistency.

It is important to assess the impact of the chosen method. Figure 5.1 shows the difference in trajectory optimisation results for the Amseterdam-Athens night-flight for the method used in this research and a method where NO_X emissions are calculated based on aircraft performance throughout the flight. This plot is only made for Jet A-1 as the in-flight NO_X emissions cannot be calculated accurately for the other fuels. The plot shows a difference in absolute climate impact, but the trend of the trajectory optimisation opportunities for higher fuel usages is very similar. From Figure 5.1, it can be concluded that the exclusion of in-flight emission changes of NO_X is not likely to affect the conclusions of this report.

Unfortunately, it is not possible to perform the same analysis for emission and performance changes during flight that affect contrail formation. This should be further researched in future efforts.

5.1.4. Trajectory optimisation software

The trajectory optimiser *OpenAP-TOP* is used to find optimal trajectories for given weights between fuel and climate costs, forcing additional fuel usages of $0.1 - 2\%$. This software yielded satisfactory results for the current research, but some limitations regarding the use of this software were encountered that are described below.

Convergence of the optimiser

The solver used for trajectory optimisation has difficulties converging at almost every attempt for which the increase in fuel usage exceeded 0.1%. This is the reason for applying the extra filtering as described

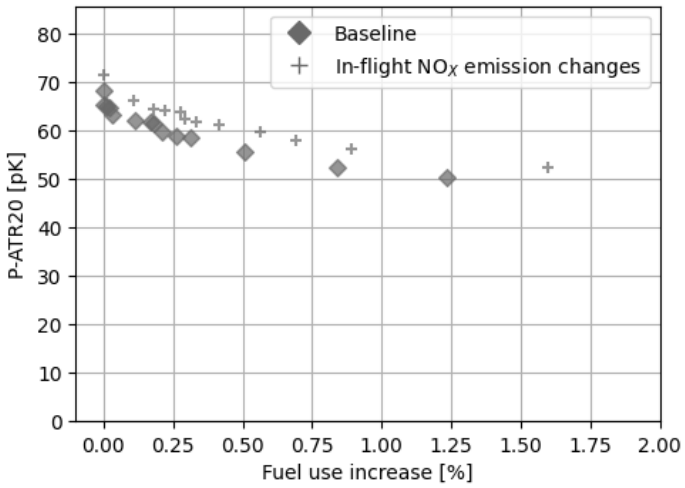

Figure 5.1: Difference in trajectory optimisation for two methods to calculate climate effects for Jet A-1. The baseline (diamonds) shows the method as used in the current research: generating cost grids before trajectory optimisation using constant values for e.g. fuel flow and NO_X emission index. The plus signs show the trajectory optimisation results when in-flight changes in values such as fuel flow and NO_X emission index are included in determining trajectory optimisation strategies. The case study used to show the difference between these two methods is the night-time flight between Amsterdam and Athens on 3 September 2023.

in section 3.2. A better solver performance would lead trends that are more clear and thus easier to interpret than the current ones shown in Figure 4.5. Customising the solver to perform optimal for this purpose is a research on its own, which would include standardising relative weighting between the aircraft types used and optimising warm start capabilities and other parameters of the ipopt solver. This was not pursued in the current research due to time constraints.

Running trajectory optimisation for traffic data

The most important next step is to compare the current findings with results from traffic data. Due to the mentioned solver convergence issues, each case study had to be analysed individually to determine correct values for weights and post-process the output of the trajectory optimisation. Finding trajectory optimisation results for larger data sets of flights can contribute to finding differences between trajectory optimisation strategies of different fuel types that can be universally implemented. Some of the observations discussed in chapter 4 are interesting to investigate further, but basing conclusions on merely six case studies does not give us any indication on the fraction of flights during which these phenomena occur.

Exclusion of ATC constraints

Optimising aircraft trajectories for climate impact reduction is difficult from an Air Traffic Control (ATC) perspective. Finding out how route diversions to avoid ISSRs would fit into the framework of ATC operations is a research on its own. However, some common ATC constraints for regular flights are not included in the current trajectory optimisation, which should be included for more realistic results. For example, cruise altitudes of flights are typically either constant throughout the cruise phase, or include only one step climb (EUROCONTROL, 2017). To focus on the real-world implementation of trajectory optimisation for contrail avoidance, such flights at constant altitude or with one step climb should be considered instead of the fuel-optimal case in the current research, which climbs almost continuously throughout the cruise phase. However, *OpenAP-TOP* only offers this option if the trajectory optimisation that follows is also performed at a constant cruise altitude. This would significantly reduce the trajectory optimisation opportunities for contrail avoidance. Adding the option of including this ATC constraint for the baseline flight and allowing for vertical in-flight route diversions for trajectory optimisation would be an asset for this trajectory optimiser and future research in general.

5.2. Recommendations for future research

The limitations discussed in the previous section reveal several topics that should be included in future efforts. The topics that are deemed priorities in future research are discussed below.

5.2.1. Volatile particles for contrail formation

Modelling vPM emissions in hydrogen-powered aircraft and their impact on the contrail climate impact should be prioritised in future efforts. Ponsonby et al. (2024b) have shown that lubrication oil droplets from aircraft engines are able to act as condensation nuclei. Fushimi et al. (2019) find that unburned lubrication oils account for half the organic particulate matter (< 30 nm) in the wake of a jet engine.
The recommended research on this topic is threefold. First, to gain a better understanding of the role of vPM emissions in the broader picture of contrail formation, software that calculates the contrail climate impact such as *pycontrails* should include more accurate vPM models. Currently, the only way in which vPM emissions are included in *pycontrails* is a lower bound on the number of nvPM emissions of 10^{13} $\mathrm{kg}_{\mathrm{fuel}}^{-1}$ to simulate the increased role of vPM in soot-poor conditions (Shapiro et al., 2024). However, Ponsonby et al. (2024a) show that the apparent emission index of ice crystals (the number of ice crystals formed per $\mathrm{kg}_{\mathrm{fuel}}$) in soot-poor conditions could be two orders of magnitude higher than in soot-rich conditions due to vPM emissions. The asymptote for the number of ice crystals formed is higher for ambient temperatures that are further below the threshold conditions (Ponsonby et al., 2024b).
Due to the higher threshold temperature of hydrogen (see subsection 2.2.2), the effect of vPM on contrail formation could be especially strong for hydrogen-powered aircraft. The second aspect that should be researched is the quantity of vPM emissions of hydrogen-powered turbofan engines. Once these engines enter the testing phase, the emission of lubrication oil droplets should be measured to obtain estimates of the in-flight vPM emissions. These measurements can be compared to similar studies for conventional engines, such as the research by Fushimi et al. (2019), and the results can be integrated into the new vPM model for contrail calculation software as described in the previous

point. Finally, if the previous two recommendations are carried out, the results can be used to aid in the design of hydrogen-powered turbofan engines to decrease the contrail climate impact by this fuel from a design perspective. Fushimi et al. (2019) suggest that lubrication oil droplets in the exhaust plume can be reduced by smarter technologies. Conventional engines typically vent lubrication oil droplets into the bypass flow, after which it mixes with combustion gases (Fushimi et al., 2019). If the proposed research into vPM emissions of hydrogen-powered turbofans show that the number of oil droplets vented is significant, and the proposed vPM model shows that this causes a high contrail climate impact, reducing vPM emissions by hydrogen-powered turbofans should be regarded a crucial design consideration for future research efforts.

5.2.2. Effect of air traffic on contrail climate impact

The current research is focused on finding the difference in contrail climate impact and trajectory optimisation strategies for individual flights. However, the difference in climate impact for the considered aircraft types would change when accounting for air traffic (see the previous section). Therefore, contrail modelling should be performed in the context of regular air traffic in future efforts. This approach is likely to decrease the difference for the climate impact between the aircraft types, and thus the possibilities of trajectory optimisation.

The contrail climate impact software *pycontrails* provides a template to consider a fleet of aircraft instead of individual flights, through its `fleet` mode. However, the inclusion of this mode particularly changes the calculated climate impact of contrails by accounting for the overlap of contrail cirrus (Shapiro et al., 2024). The impact of the reinvigoration of old contrail cirrus, described by Burkhardt et al. (2018), is not included in these calculations. This effect is accounted for in the contrail-cirrus module of the global climate model *ECHAM5*, called `CCMod`. Thus, future research efforts on this topic should either use this software to account for the full effect of air traffic on the contrail climate impact of alternative fuels, or similar calculations should be included in the `fleet` mode of *pycontrails*.

5.2.3. Aircraft performance for trajectory optimisation

The analysis in subsection 5.1.3 showed that including aircraft performance in the calculations of NO_X emissions during trajectory optimisation affected the magnitude of the flight's climate impact, but is not expected to severely change the outcome of trajectory optimisation per se. However, this analysis is not possible for the inclusion of aircraft performance on the contrail climate impact. The high impact of fuel flow and soot emissions (for Jet A-1 and SAF) on contrail formation indicate that including these values with in-flight changes could yield altered results. Future research efforts should focus on a more accurate method to include contrail cost grids into trajectory optimisation software to include these in-flight changes. A possible improvement would be to change the cost grids generated by `CoCiP-grid` in *pycontrails* to be functions of the fuel flow and thrust setting.

Comparing the current results with these future efforts should point out whether including aircraft performance in contrail climate impact calculations is necessary to obtain accurate results, or if the current method provides sufficiently accurate estimates. If the former is true, the ease-of-use of the cost grid approach should be re-examined (see subsection 3.1.3).

6

Conclusion

This research aims to contribute to our understanding of the potential impact of hydrogen-powered aircraft in the future aviation sector considering trajectory optimisation strategies for contrail avoidance. Three aircraft types are considered during this research: hydrogen-powered aircraft, current aircraft powered by Jet A-1, to compare hydrogen-powered aircraft to the status quo, and future aircraft powered by a 70% SAF blend, to compare hydrogen-powered aircraft to an equivalent aircraft with a similar time of entry-into-service. This research focusses on the difference in contrail formation of the three aircraft concepts, methods of contrail analysis to be used for trajectory optimisation, and the potential of trajectory optimisation per aircraft type to decrease their climate impact.

The contrail analysis for individual flights showed large differences in the number of ice crystals formed due to altered amounts of nvPM emissions of Jet A-1 and SAF, and the reliance of contrail formation on ambient particles for hydrogen. The number of ice crystals decreases by 89% when using hydrogen instead of Jet A-1. When comparing hydrogen to the 70% SAF blend, this decrease amounts to 81%. The resulting differences in radiative forcing are 87% and 79%, respectively.

To obtain contrail analysis results to be used for trajectory optimisation, two methods are explored. The first is to find correlations between the climate impact of contrails and atmospheric variables to form an equivalent of current algorithmic climate change functions (aCCF) for hydrogen-powered aircraft. Whereas correlations found by simplified contrail analysis methods in literature are adequately strong to form an aCCF, contrail analysis of traffic data sets in *pycontrails* proved that these correlations are too weak to pursue further for more complex contrail climate cost calculations. The second proposed method is based on contrail climate impact analysis on a grid, which can directly be imported into trajectory optimisation software. This method is found to be the superior method to provide accurate values for contrail climate impact to be used for trajectory optimisation.

Prior to applying trajectory optimisation to six case studies, the climate costs of their fuel-optimal routes are calculated. This shows the impact of implementing hydrogen-powered aircraft disregarding route optimisations: the total climate impact for such a flight is generally decreased by $80-90\%$ compared to current Jet A-1 aircraft. Only when there is a strong presence of ISSRs that produce cooling contrails, the climate impact decrease of using hydrogen is much less significant. However, the occurrence of these regions is very rare. The climate impact decreases with $2-60\%$ when using the 70% SAF blend instead of Jet A-1.

The potential for trajectory optimisation of hydrogen-powered aircraft is very low, which can be attributed to the minor contribution of contrails in the total climate impact of hydrogen-powered flight: $0-38\%$ of the total climate impact is due to contrails in six case studies, compared to $41-76\%$ for Jet A-1 and $34-68\%$ for the 70% SAF blend. Avoiding contrails at the cost of other emissions for hydrogen-powered aircraft barely lowers the total climate impact as a result. Trajectory optimisation for the other aircraft concepts is much more advantageous. Apart from the difference in emission profiles, the mission profiles of the aircraft types highly affect the efficacy of trajectory optimisation. The fuel-optimal cruise altitude of the hydrogen-powered aircraft type is typically lower than for the other aircraft types, causing the aircraft to avoid certain ISSRs that the other aircraft pass through in the analysed case studies. Considering the high projected fuel costs of hydrogen along with the small potential gains in climate effects, airlines are expected not to be interested in route diversions for hydrogen-powered aircraft.

Trajectory optimisation for hydrogen-powered aircraft is more effective if the contrail climate impact magnitude and ambient particle number concentrations are underestimated in the current research. However, upper bounds on these variables that are expected in literature do not change this efficacy to the extent that it competes with the possibilities of route diversions with Jet A-1 and the 70% SAF blend. If vPM play a large role in contrail formation, the potential of trajectory optimisation for hydrogen-powered aircraft could increase significantly. For future efforts, it is key to better understand the role of these emissions in contrail formation, as well as the effect of dense air traffic on the climate impact of contrails with fewer ice crystals. To improve the basis of this research, it is important to increase the ability of the solver to converge to global optima and to include in-flight emission changes.
Even though this research concludes that trajectory optimisation is not beneficial for hydrogen-powered aircraft, it strongly supports the integration of hydrogen-powered aircraft in the aviation sector. The reduction of in-flight climate impact is generally more significant than what can be achieved through trajectory optimisation by conventional aircraft.

References

Appleman, H. (1953). The Formation of Exhaust Condensation Trails by Jet Aircraft. *Bulletin of the American Meteorological Society*, *34*(1), 14–20. https://doi.org/10.1175/1520-0477-34.1.14

Balli, O., Ozbek, E., Ekici, S., Midilli, A., & Hikmet Karakoc, T. (2021). Thermodynamic comparison of TF33 turbofan engine fueled by hydrogen in benchmark with kerosene. *Fuel*, *306*, 121686. https://doi.org/10.1016/j.fuel.2021.121686

Bier, A., Unterstrasser, S., & Vancassel, X. (2022). Box model trajectory studies of contrail formation using a particle-based cloud microphysics scheme. *Atmospheric Chemistry and Physics*, *22*(2), 823–845. https://doi.org/10.5194/acp-22-823-2022

Bier, A., Unterstrasser, S., Zink, J., Hillenbrand, D., Jurkat-Witschas, T., & Lottermoser, A. (2024). Contrail formation on ambient aerosol particles for aircraft with hydrogen combustion: A box model trajectory study. *Atmospheric Chemistry and Physics*, *24*(4), 2319–2344. https://doi.org/10.5194/acp-24-2319-2024

Borella, A., Boucher, O., Shine, K. P., Stettler, M., Tanaka, K., Teoh, R., & Bellouin, N. (2024, February). The importance of an informed choice of CO_2 -equivalence metrics for contrail avoidance. https://doi.org/10.5194/egusphere-2024-347

Borrmann, S., Kunkel, D., Weigel, R., Minikin, A., Deshler, T., Wilson, J. C., Curtius, J., Volk, C. M., Homan, C. D., Ulanovsky, A., Ravegnani, F., Viciani, S., Shur, G. N., Belyaev, G. V., Law, K. S., & Cairo, F. (2010). Aerosols in the tropical and subtropical UT/LS: In-situ measurements of submicron particle abundance and volatility. *Atmospheric Chemistry and Physics*, *10*(12), 5573–5592. https://doi.org/10.5194/acp-10-5573-2010

Brink, L. F. J. (2020, September). *Modeling the Impact of Fuel Composition on Aircraft Engine NO□, CO and Soot Emissions* [Doctoral dissertation, Massachusetts Institute of Technology].

Brock, C. A., Froyd, K. D., Dollner, M., Williamson, C. J., Schill, G., Murphy, D. M., Wagner, N. J., Kupc, A., Jimenez, J. L., Campuzano-Jost, P., Nault, B. A., Schroder, J. C., Day, D. A., Price, D. J., Weinzierl, B., Schwarz, J. P., Katich, J. M., Wang, S., Zeng, L., … Wofsy, S. C. (2021). Ambient aerosol properties in the remote atmosphere from global-scale in situ measurements. *Atmospheric Chemistry and Physics*, *21*(19), 15023–15063. https://doi.org/10.5194/acp-21-15023-2021

Burkhardt, U., Bock, L., & Bier, A. (2018). Mitigating the contrail cirrus climate impact by reducing aircraft soot number emissions. *npj Climate and Atmospheric Science*, *1*(1), 37. https://doi.org/10.1038/s41612-018-0046-4

Carter, R., & Agarwal, R. (2021, December). Development Of A Liquid Hydrogen Combustion High Bypass Turbofan Model In NPSS.

Clean Sky 2 JU & FCH 2 JU. (2020, May). Hydrogen-powered aviation: A fact-based study of hydrogen technology, economics, and climate impact by 2050.

Council of the EU. (2022, June). Proposal for a Regulation of the European Parliament and of the Council on ensuring a level playing field for sustainable air transport – 'ReFuelEU Aviation'- General Approach. Retrieved July 28, 2024, from https://data.consilium.europa.eu/doc/document/ST-9805-2022-INIT/en/pdf

Council of the EU. (2023, October). RefuelEU aviation initiative - Council adopts new law to decarbonise the aviation sector. Retrieved December 16, 2024, from https://www.consilium.europa.eu/en/press/press-releases/2023/10/09/refueleu-aviation-initiative-council-adopts-new-law-to-decarbonise-the-aviation-sector/

Derakhshandeh, P., Ahmadi, A., & Dashti, R. (2021). Simulation and technical-economic-environmental optimization of the General Electric GE90 hydrogen turbofan engine. *International Journal of Hydrogen Energy*, *46*(5), 3303–3318. https://doi.org/10.1016/j.ijhydene.2020.10.182

Dietmüller, S., Matthes, S., Dahlmann, K., Yamashita, H., Simorgh, A., Soler, M., Linke, F., Lührs, B., Meuser, M. M., Weder, C., Grewe, V., Yin, F., & Castino, F. (2023). A Python library for computing individual and merged non-CO_2 algorithmic climate change functions: CLIMaCCF V1.0.

Geoscientific Model Development, *16*(15), 4405–4425. https://doi.org/10.5194/gmd-16-4405-2023

EUROCONTROL. (2017, March). Specification for Trajectory Prediction.

Frieden, F., & Leker, J. (2024). Future costs of hydrogen: A quantitative review. *Sustainable Energy & Fuels*, *8*(9), 1806–1822. https://doi.org/10.1039/D4SE00137K

Funke, H.-W., Beckmann, N., & Abanteriba, S. (2019). An overview on dry low NOx micromix combustor development for hydrogen-rich gas turbine applications. *International Journal of Hydrogen Energy*, *44*(13), 6978–6990. https://doi.org/10.1016/j.ijhydene.2019.01.161

Fushimi, A., Saitoh, K., Fujitani, Y., & Takegawa, N. (2019). Identification of jet lubrication oil as a major component of aircraft exhaust nanoparticles. *Atmospheric Chemistry and Physics*, *19*(9), 6389–6399. https://doi.org/10.5194/acp-19-6389-2019

Gierens, K. (2021). Theory of Contrail Formation for Fuel Cells. *Aerospace*, *8*(6), 164. https://doi.org/10.3390/aerospace8060164

Hoelzen, J., Flohr, M., Silberhorn, D., Mangold, J., Bensmann, A., & Hanke-Rauschenbach, R. (2022a). H2-powered aviation at airports – Design and economics of LH2 refueling systems. *Energy Conversion and Management: X*, *14*, 100206. https://doi.org/10.1016/j.ecmx.2022.100206

Hoelzen, J., Silberhorn, D., Zill, T., Bensmann, B., & Hanke-Rauschenbach, R. (2022b). Hydrogen-powered aviation and its reliance on green hydrogen infrastructure – Review and research gaps. *International Journal of Hydrogen Energy*, *47*(5), 3108–3130. https://doi.org/10.1016/j.ijhydene.2021.10.239

Holzäpfel, F. (2003). Probabilistic Two-Phase Wake Vortex Decay and Transport Model. *Journal of Aircraft*, *40*(2), 323–331. https://doi.org/10.2514/2.3096

IATA. (2021, October). Net-Zero Carbon Emissions by 2050. Retrieved December 20, 2024, from https://www.iata.org/en/pressroom/pressroom-archive/2021-releases/2021-10-04-03/

IATA. (2023, September). Fuel fact sheet.

ICAO. (2024, July). ICAO Aircraft Engine Emissions Databank. Retrieved December 18, 2024, from https://www.easa.europa.eu/en/domains/environment/icao-aircraft-engine-emissions-databank

Inness, A., Ades, M., Agustí-Panareda, A., Barré, J., Benedictow, A., Blechschmidt, A.-M., Dominguez, J. J., Engelen, R., Eskes, H., Flemming, J., Huijnen, V., Jones, L., Kipling, Z., Massart, S., Parrington, M., Peuch, V.-H., Razinger, M., Remy, S., Schulz, M., & Suttie, M. (2019). The CAMS reanalysis of atmospheric composition. *Atmospheric Chemistry and Physics*, *19*(6), 3515–3556. https://doi.org/10.5194/acp-19-3515-2019

Irvine, E. (2017). ATM4E internal report: Contrail algorithmic Climate Change Function derivation.

Kärcher, B. (1999). Aviation-Produced Aerosols and Contrails.

Kärcher, B., Burkhardt, U., Bier, A., Bock, L., & Ford, I. J. (2015). The microphysical pathway to contrail formation. *Journal of Geophysical Research: Atmospheres*, *120*(15), 7893–7927. https://doi.org/10.1002/2015JD023491

Kärcher, B., & Yu, F. (2009). Role of aircraft soot emissions in contrail formation. *Geophysical Research Letters*, *36*(1), 2008GL036649. https://doi.org/10.1029/2008GL036649

Klingaman, E., & Shine, K. (2023). Predicting the climate impact of aviation for en-route emissions: The algorithmic climate change function submodel ACCF 1.0 of EMAC 2.53.

Lammen, W., Kos, J., Sman, E. v. d., & Peerlings, B. (2022). Hydrogen-powered propulsion aircraft: Conceptual sizing and fleet level impact analysis [Artwork Size: 16 pages Medium: PDF Publisher: [object Object]], 16 pages. https://doi.org/10.13009/EUCASS2022-7300

Lee, D., Fahey, D., Skowron, A., Allen, M., Burkhardt, U., Chen, Q., Doherty, S., Freeman, S., Forster, P., Fuglestvedt, J., Gettelman, A., De León, R., Lim, L., Lund, M., Millar, R., Owen, B., Penner, J., Pitari, G., Prather, M., … Wilcox, L. (2021). The contribution of global aviation to anthropogenic climate forcing for 2000 to 2018. *Atmospheric Environment*, *244*, 117834. https://doi.org/10.1016/j.atmosenv.2020.117834

Lewellen, D. C., Meza, O., & Huebsch, W. W. (2014). Persistent Contrails and Contrail Cirrus. Part I: Large-Eddy Simulations from Inception to Demise. *Journal of the Atmospheric Sciences*, *71*(12), 4399–4419. https://doi.org/10.1175/JAS-D-13-0316.1

Martin Frias, A., Shapiro, M. L., Engberg, Z., Zopp, R., Soler, M., & Stettler, M. E. J. (2024). Feasibility of contrail avoidance in a commercial flight planning system: An operational analysis. *Environ-*

mental Research: Infrastructure and Sustainability, *4*(1), 015013. https://doi.org/10.1088/2634-4505/ad310c

Matthes, S., Grewe, V., Dahlmann, K., Frömming, C., Irvine, E., Lim, L., Linke, F., Lührs, B., Owen, B., Shine, K., Stromatas, S., Yamashita, H., & Yin, F. (2017). A Concept for Multi-Criteria Environmental Assessment of Aircraft Trajectories. *Aerospace*, *4*(3), 42. https://doi.org/10.3390/aerospace4030042

Megill, L., Deck, K., & Grewe, V. (2024). Alternative climate metrics to the Global Warming Potential are more suitable for assessing aviation non-CO2 effects. *Communications Earth & Environment*, *5*(1), 249. https://doi.org/10.1038/s43247-024-01423-6

Miake-Lye, R. (2024, September). ICAO Non-CO2 Symposium: Enhancing Scientific Knowledge Part I - NOx and Particulate Matter.

Minikin, A., Petzold, A., Ström, J., Krejci, R., Seifert, M., Van Velthoven, P., Schlager, H., & Schumann, U. (2003). Aircraft observations of the upper tropospheric fine particle aerosol in the Northern and Southern Hemispheres at midlatitudes. *Geophysical Research Letters*, *30*(10), 2002GL016458. https://doi.org/10.1029/2002GL016458

Ponsonby, J., Teoh, R., & Stettler, M. (2024a). Towards an improved treatment of (semi) volatile particle activation in contrail models. *EGU24-17410*. https://doi.org/https://doi.org/10.5194/egusphere-egu24-17410

Ponsonby, J., King, L., Murray, B. J., & Stettler, M. E. J. (2024b). Jet aircraft lubrication oil droplets as contrail ice-forming particles. *Atmospheric Chemistry and Physics*, *24*(3), 2045–2058. https://doi.org/10.5194/acp-24-2045-2024

Sáez Ortuño, M. Á., Yin, F., Gangoli Rao, A., Vos, R., & Proesmans, P.-J. (2023). Climate Assessment of Hydrogen Combustion Aircraft: Towards a Green Aviation Sector. *AIAA SCITECH 2023 Forum*. https://doi.org/10.2514/6.2023-2513

Schmidt, E. (1941). Schmidt_1941_eisnebel_kondensstreifen_contrails.pdf. *Schriften der Deutschen Akademie der Luftfahrtforschung, 44*, 1–15.

Schumann, U. (2012). A contrail cirrus prediction model. *Geoscientific Model Development*, *5*(3), 543–580. https://doi.org/10.5194/gmd-5-543-2012

Schumann, U., Mayer, B., Graf, K., & Mannstein, H. (2012). A Parametric Radiative Forcing Model for Contrail Cirrus. *Journal of Applied Meteorology and Climatology*, *51*(7), 1391–1406. https://doi.org/10.1175/JAMC-D-11-0242.1

Schumann, U. (1996). On conditions for contrail formation from aircraft exhausts. *Meteorologische Zeitschrift*.

Schumann, U. (2005). Formation, properties and climatic effects of contrails. *Comptes Rendus. Physique*, *6*(4-5), 549–565. https://doi.org/10.1016/j.crhy.2005.05.002

Shapiro, M., Engberg, Z., Teoh, R., Stettler, M., Dean, T., & Abbott, T. (2024, October). Pycontrails: Python library for modeling aviation climate impacts. https://doi.org/10.5281/zenodo.13940270

Stuber, N., Forster, P., Rädel, G., & Shine, K. (2006). The importance of the diurnal and annual cycle of air traffic for contrail radiative forcing. *Nature*, *441*(7095), 864–867. https://doi.org/10.1038/nature04877

Sun, J. (2022). OpenAP.top: Open Flight Trajectory Optimization for Air Transport and Sustainability Research. *Aerospace*, *9*(7), 383. https://doi.org/10.3390/aerospace9070383

Sun, J., Hoekstra, J. M., & Ellerbroek, J. (2020). OpenAP: An Open-Source Aircraft Performance Model for Air Transportation Studies and Simulations. *Aerospace*, *7*(8), 104. https://doi.org/10.3390/aerospace7080104

Teoh, R., Schumann, U., Voigt, C., Schripp, T., Shapiro, M., Engberg, Z., Molloy, J., Koudis, G., & Stettler, M. E. J. (2022). Targeted Use of Sustainable Aviation Fuel to Maximize Climate Benefits. *Environmental Science & Technology*, *56*(23), 17246–17255. https://doi.org/10.1021/acs.est.2c05781

Unterstrasser, S., Gierens, K., & Spichtinger, P. (2008). The evolution of contrail microphysics in the vortex phase. *Meteorologische Zeitschrift*, *17*(2), 145–156. https://doi.org/10.1127/0941-2948/2008/0273

Van Manen, J., & Grewe, V. (2019). Algorithmic climate change functions for the use in eco-efficient flight planning. *Transportation Research Part D: Transport and Environment*, *67*, 388–405. https://doi.org/10.1016/j.trd.2018.12.016

Wilhelm, L., Gierens, K., & Rohs, S. (2021). Weather Variability Induced Uncertainty of Contrail Radiative Forcing.

Wong, H.-W., Jun, M., Peck, J., Waitz, I. A., & Miake-Lye, R. C. (2015). Roles of Organic Emissions in the Formation of Near Field Aircraft-Emitted Volatile Particulate Matter: A Kinetic Microphysical Modeling Study. *Journal of Engineering for Gas Turbines and Power*, *137*(7), 072606. https://doi.org/10.1115/1.4029366

Yin, F., Grewe, V., Castino, F., Rao, P., Matthes, S., Dahlmann, K., Dietmüller, S., Frömming, C., Yamashita, H., Peter, P., Klingaman, E., Shine, K. P., Lührs, B., & Linke, F. (2023). Predicting the climate impact of aviation for en-route emissions: The algorithmic climate change function submodel ACCF 1.0 of EMAC 2.53. *Geoscientific Model Development*, *16*(11), 3313–3334. https://doi.org/10.5194/gmd-16-3313-2023

A

Relative contributions of emissions to the climate impact per fuel type

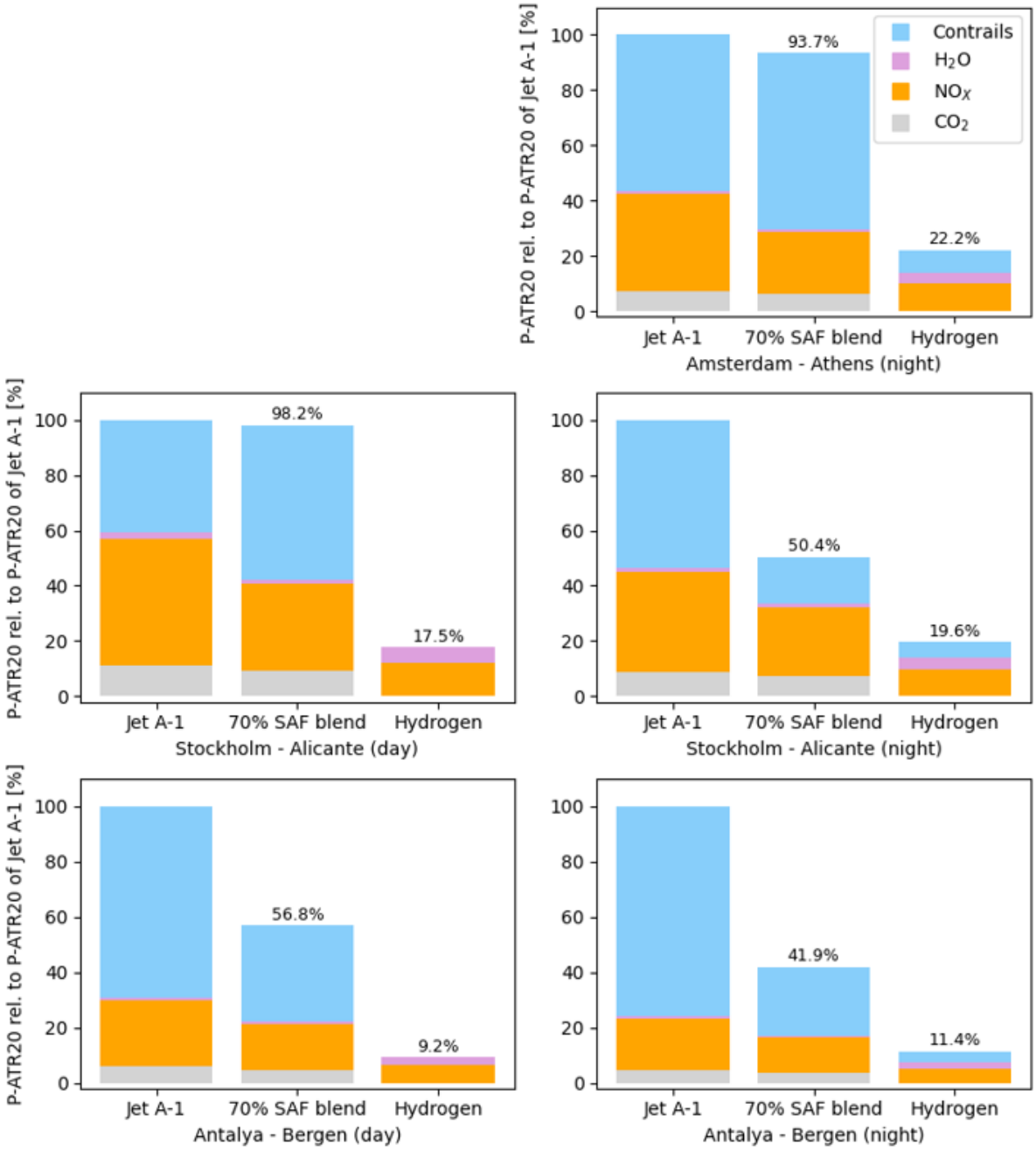

Figure A.1: The differences in climate impact of a the 70% SAF blend and hydrogen compared to Jet A-1. The climate impact values are calculated on the fuel-optimal route for each aircraft type. The values are therefore subject to differences in mission profiles. The colours signify the contributions of the different climate effects of the aircraft emissions. The climate impact is analysed according to the P-ATR20 climate metric.

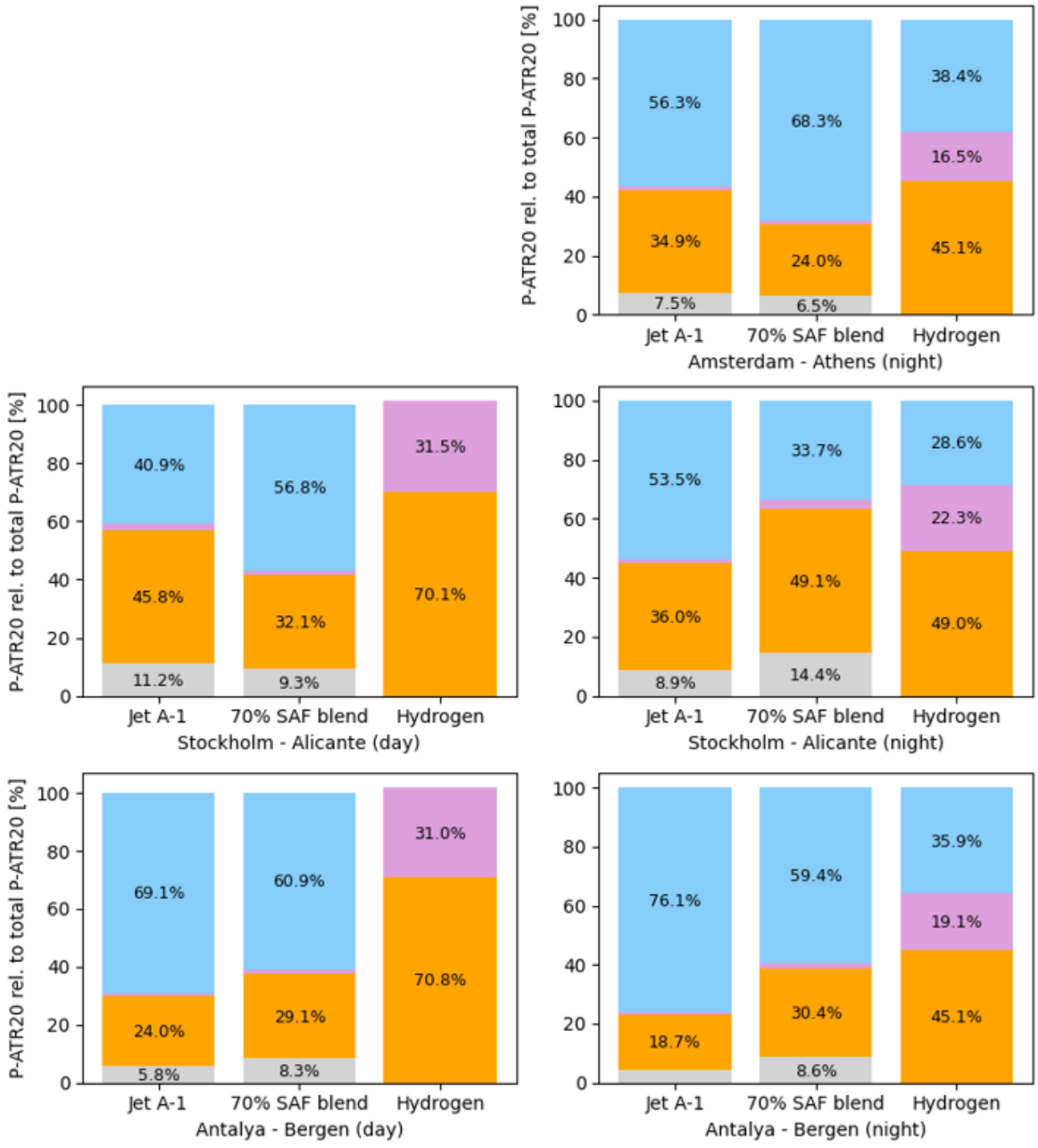

Figure A.2: The relative contributions of climate effects for the total climate impact of each aircraft model considered in this research. The climate impact values are calculated on the fuel-optimal route for each aircraft type. The values are therefore subject to differences in mission profiles. The climate impact is analysed according to the P-ATR20 climate metric.

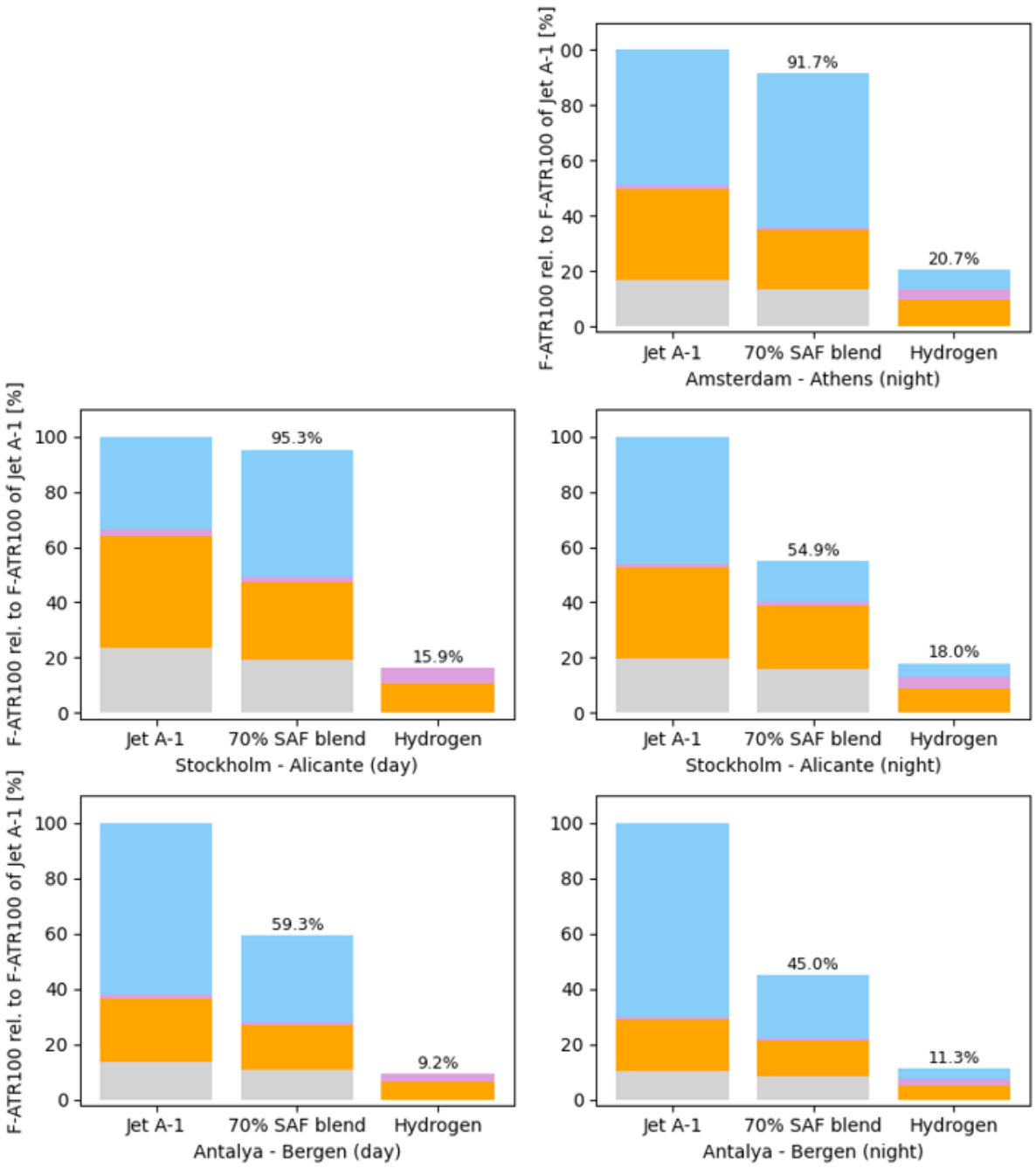

Figure A.3: The differences in climate impact of a the 70% SAF blend and hydrogen compared to Jet A-1. The climate impact values are calculated on the fuel-optimal route for each aircraft type. The values are therefore subject to differences in mission profiles. The colours signify the contributions of the different climate effects of the aircraft emissions. The climate impact is analysed according to the F-ATR100 climate metric.

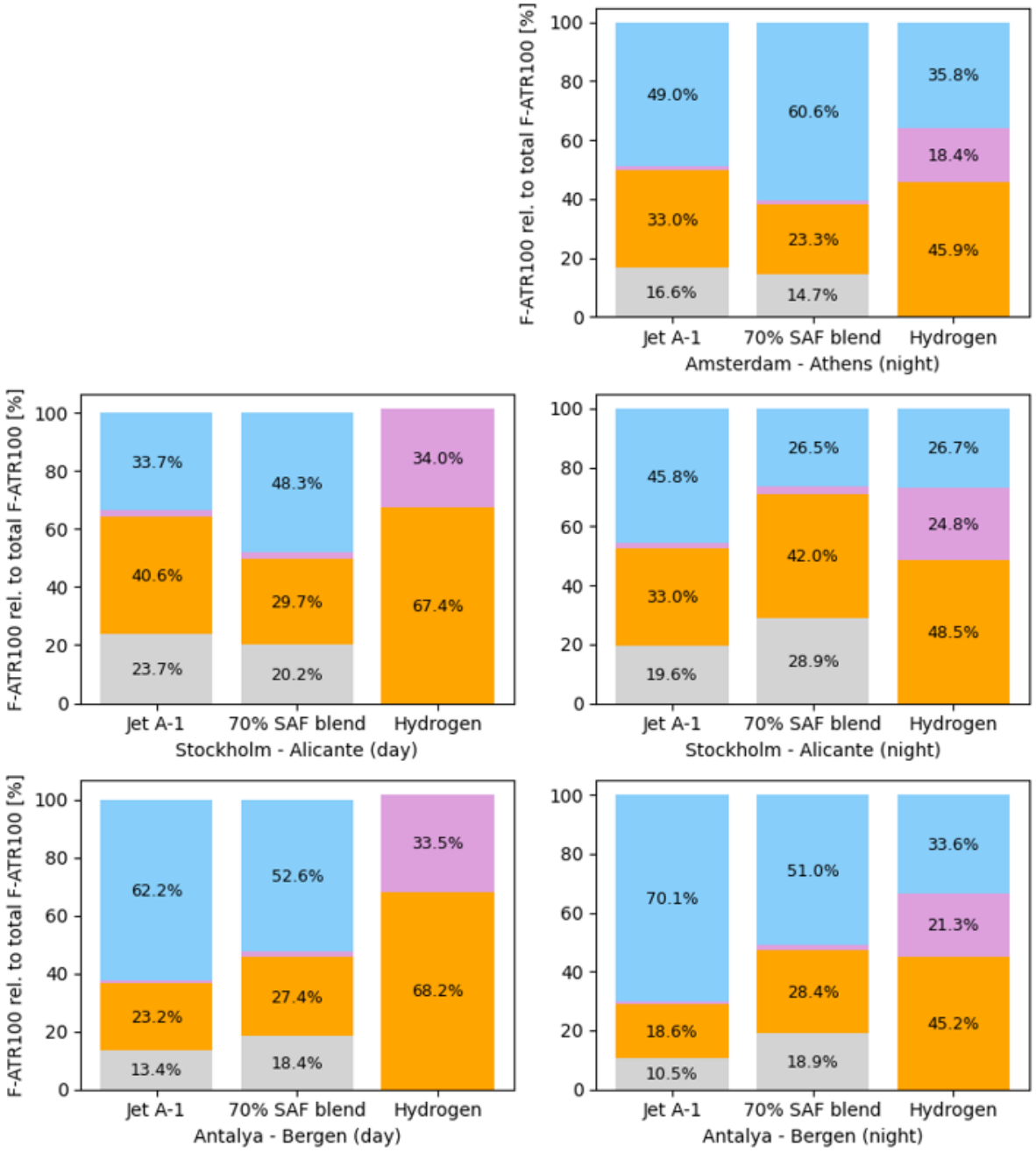

Figure A.4: The relative contributions of climate effects for the total climate impact of each aircraft model considered in this research. The climate impact values are calculated on the fuel-optimal route for each aircraft type. The values are therefore subject to differences in mission profiles. The climate impact is analysed according to the F-ATR100 climate metric.

B

Route diversions for trajectory optimisation

Amsterdam to Athens during the day with Jet A-1

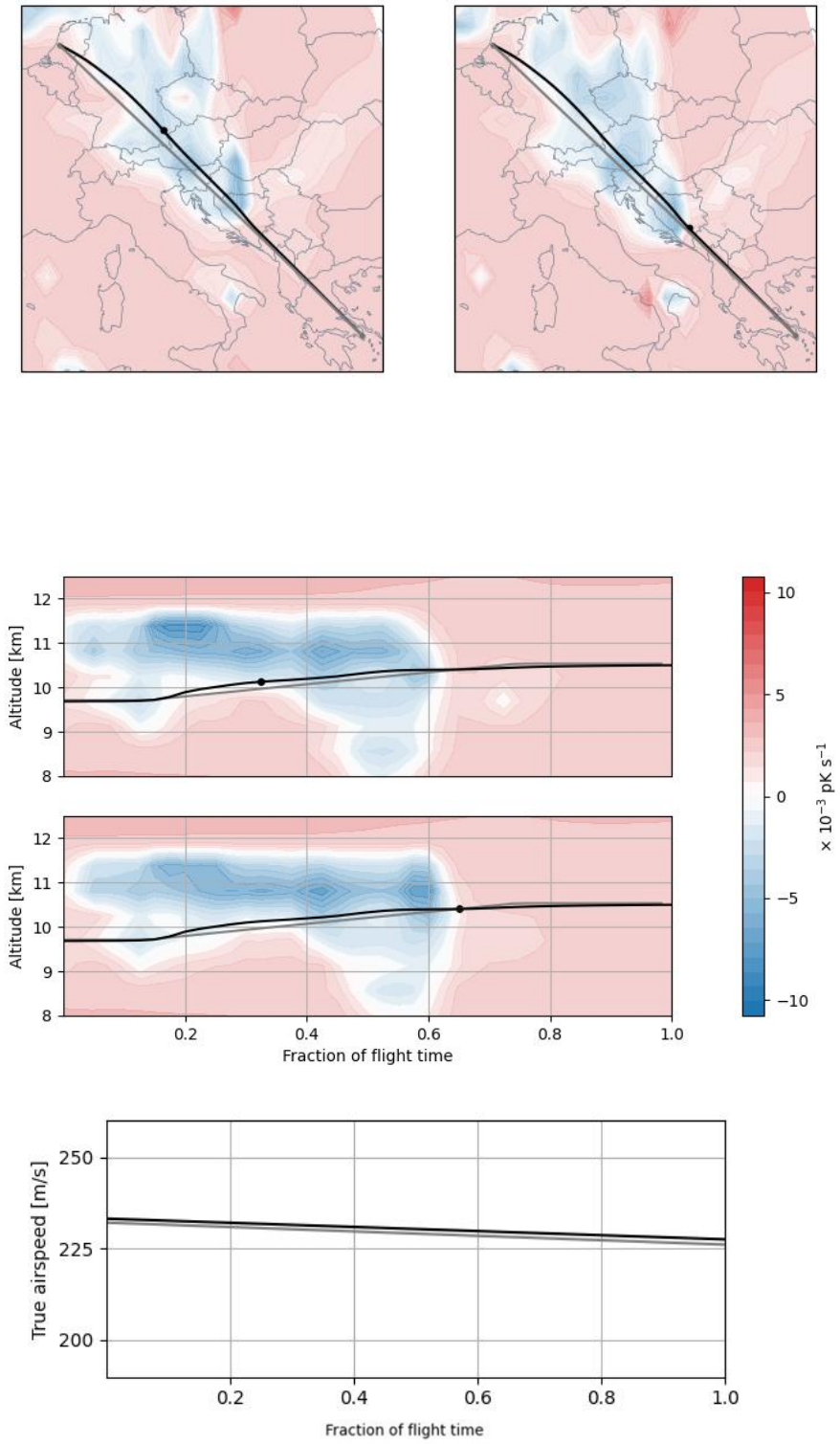

Figure B.1: Visualisation of the flight diversions for trajectory optimisation with a fuel use increase of 0.8%. Horizontal rerouting is shown at the top, changes in altitude are shown in the middle, and velocity changes at the bottom. The grey line represents the fuel optimal route and the black one the optimised trajectory.

Amsterdam to Athens during the day with a 70% SAF blend

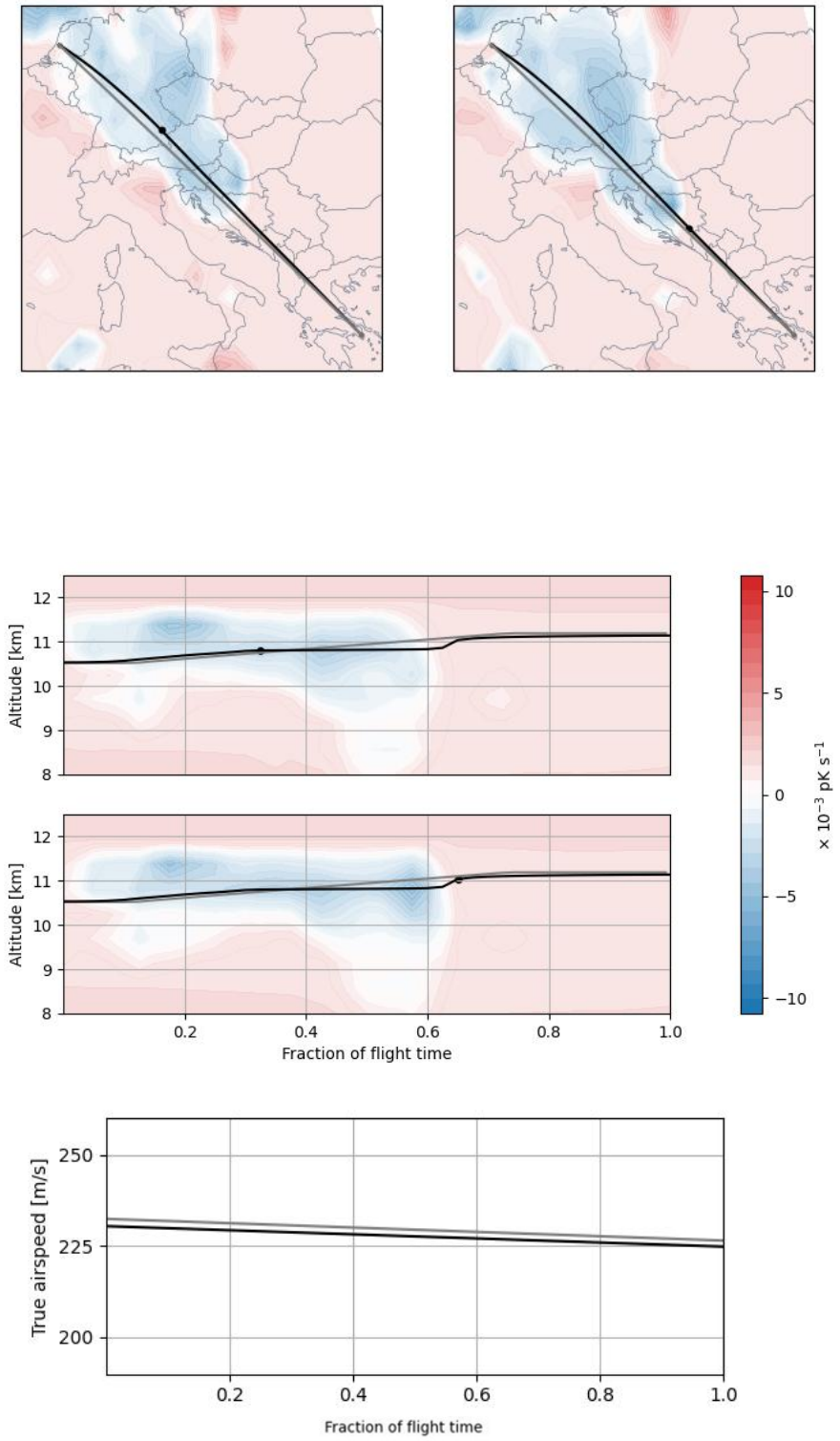

Figure B.2: Visualisation of the flight diversions for trajectory optimisation with a fuel use increase of 0.5%. Horizontal rerouting is shown at the top, changes in altitude are shown in the middle, and velocity changes at the bottom. The grey line represents the fuel optimal route and the black one the optimised trajectory.

Amsterdam to Athens during the day with hydrogen

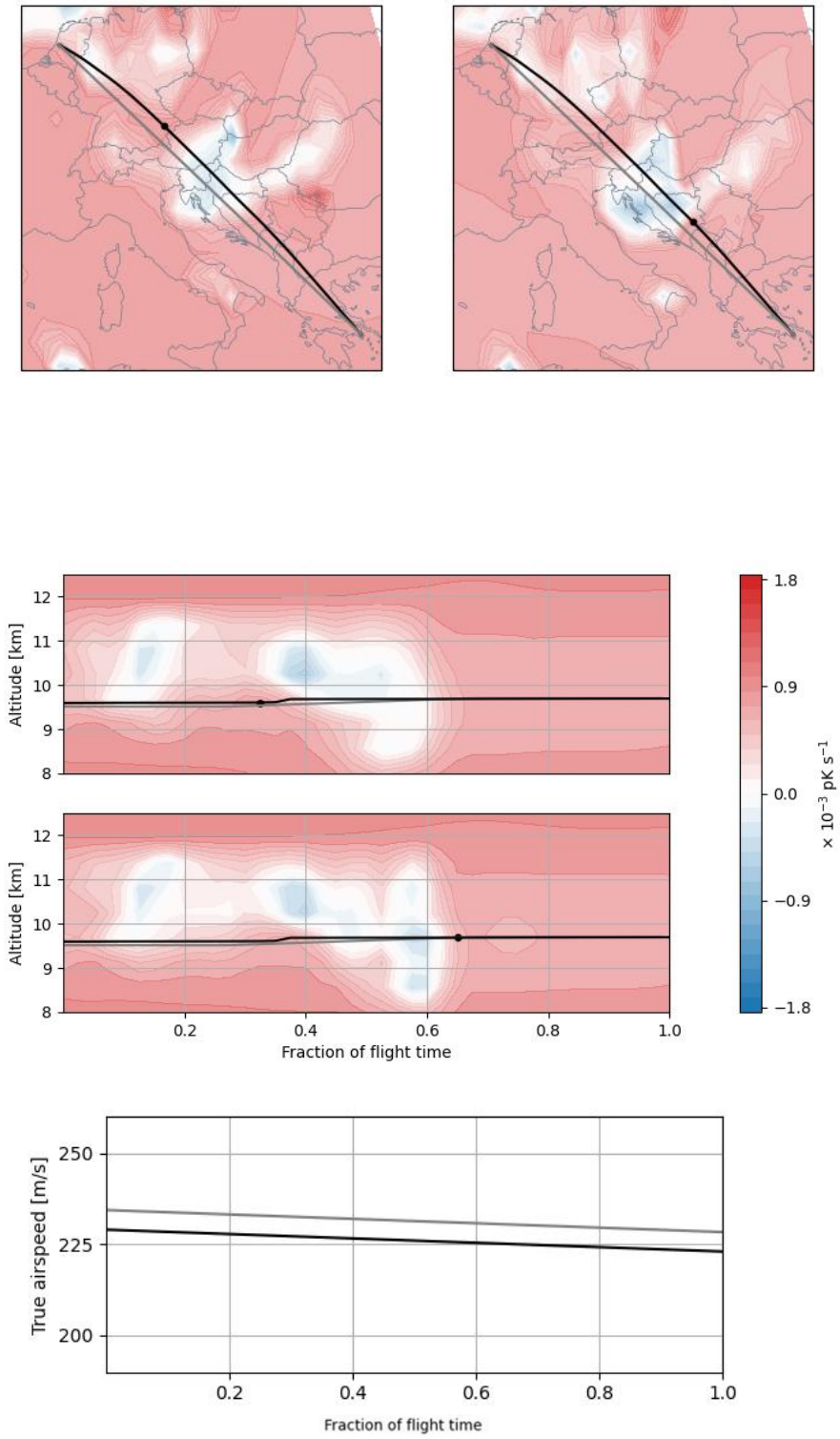

Figure B.3: Visualisation of the flight diversions for trajectory optimisation with a fuel use increase of 0.5%. Horizontal rerouting is shown at the top, changes in altitude are shown in the middle, and velocity changes at the bottom. The grey line represents the fuel optimal route and the black one the optimised trajectory.

Amsterdam to Athens during the night with Jet A-1

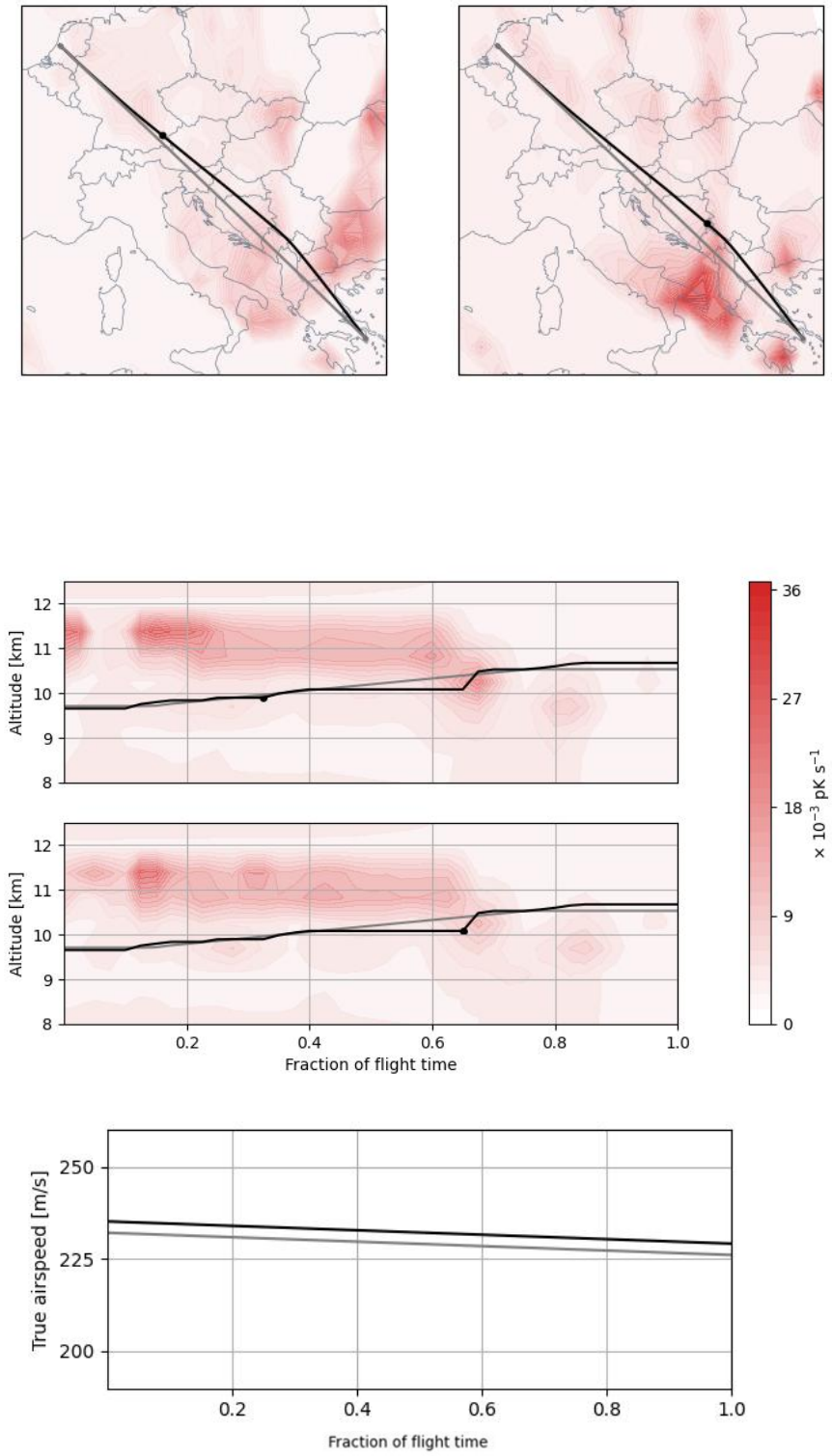

Figure B.4: Visualisation of the flight diversions for trajectory optimisation with a fuel use increase of 0.5%. Horizontal rerouting is shown at the top, changes in altitude are shown in the middle, and velocity changes at the bottom. The grey line represents the fuel optimal route and the black one the optimised trajectory.

Amsterdam to Athens during the night with a 70% SAF blend

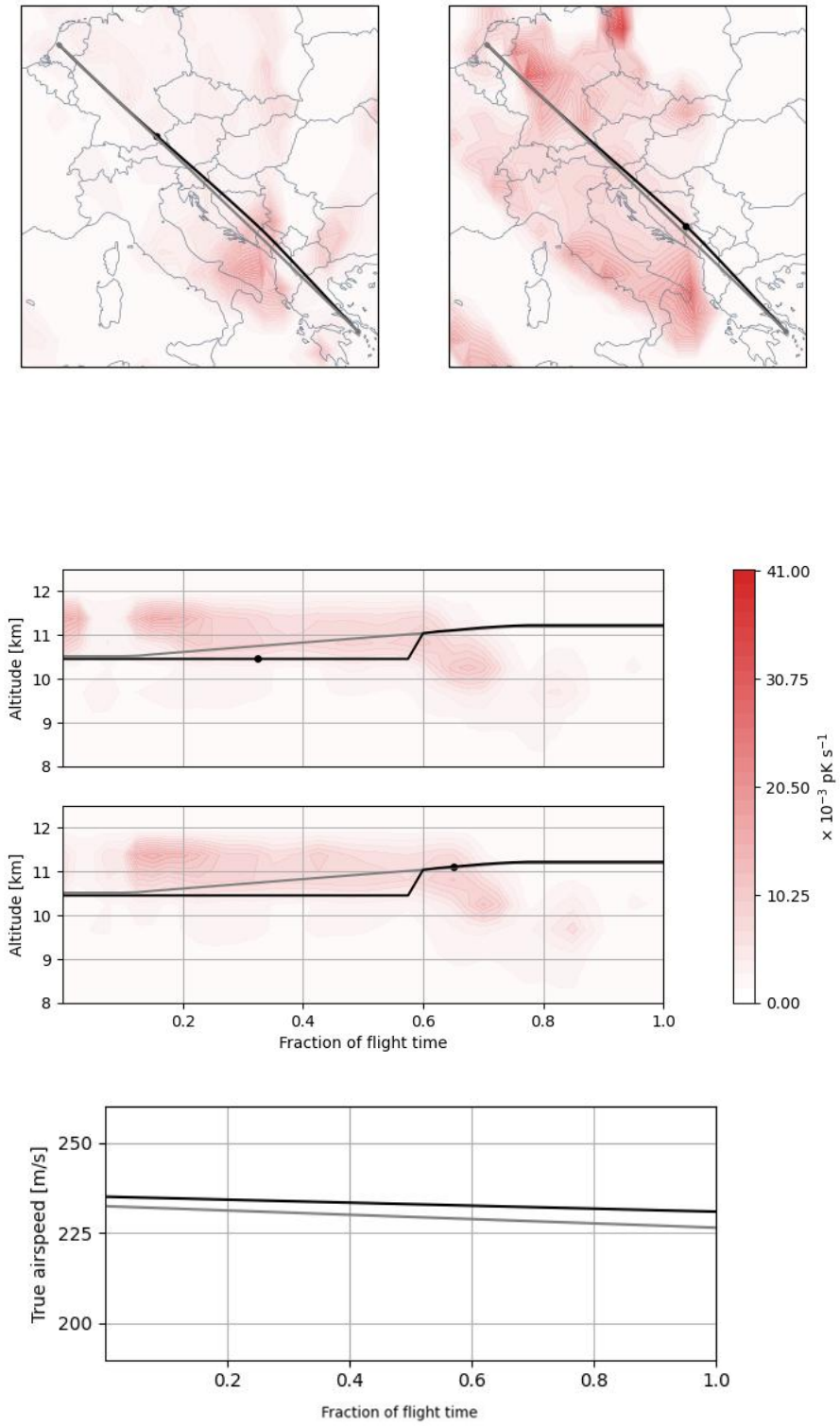

Figure B.5: Visualisation of the flight diversions for trajectory optimisation with a fuel use increase of 0.6%. Horizontal rerouting is shown at the top, changes in altitude are shown in the middle, and velocity changes at the bottom. The grey line represents the fuel optimal route and the black one the optimised trajectory.

Amsterdam to Athens during the night with hydrogen

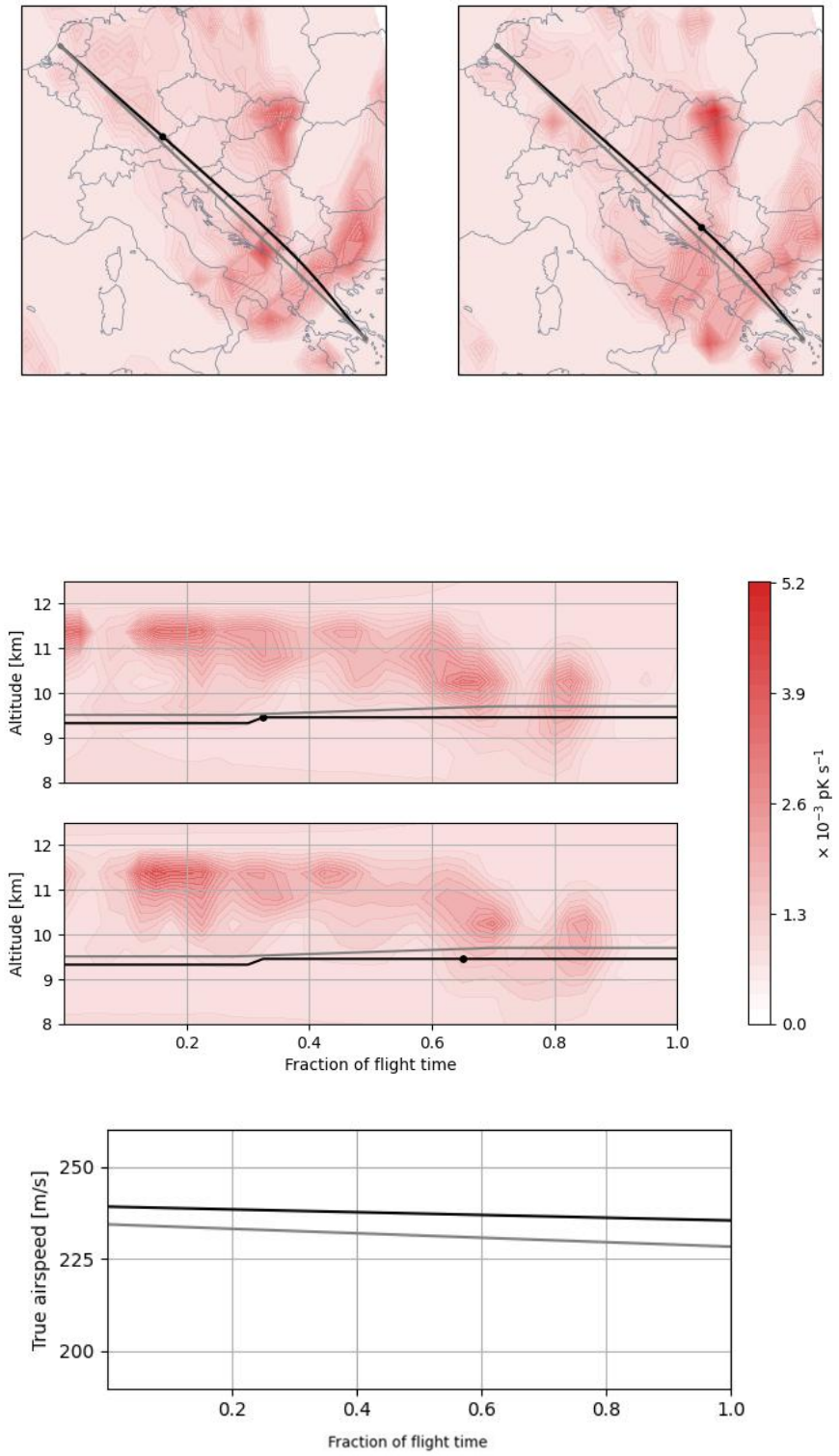

Figure B.6: Visualisation of the flight diversions for trajectory optimisation with a fuel use increase of 0.5%. Horizontal rerouting is shown at the top, changes in altitude are shown in the middle, and velocity changes at the bottom. The grey line represents the fuel optimal route and the black one the optimised trajectory.

Stockholm to Alicante during the day with Jet A-1

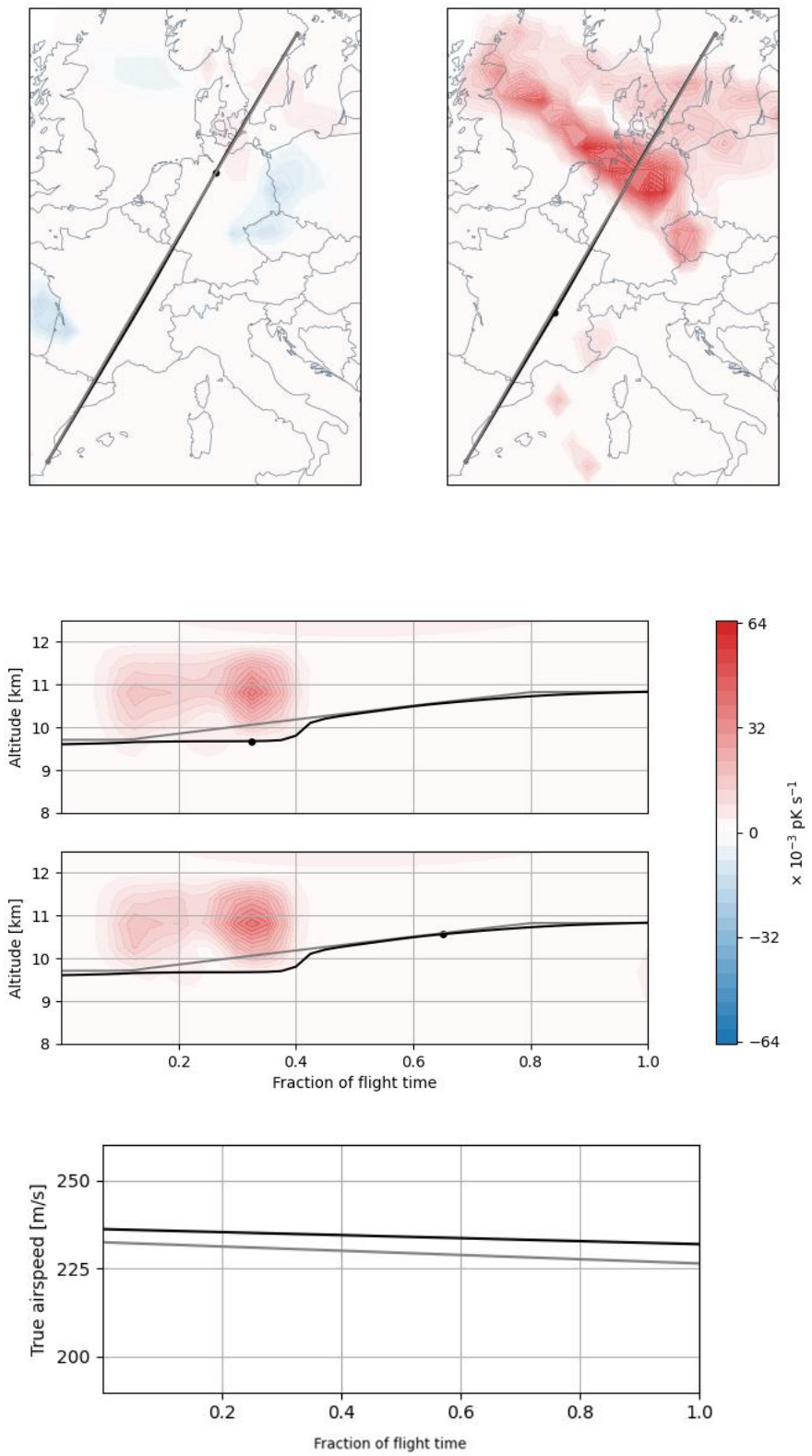

Figure B.7: Visualisation of the flight diversions for trajectory optimisation with a fuel use increase of 0.5%. Horizontal rerouting is shown at the top, changes in altitude are shown in the middle, and velocity changes at the bottom. The grey line represents the fuel optimal route and the black one the optimised trajectory.

Stockholm to Alicante during the day with a 70% SAF blend

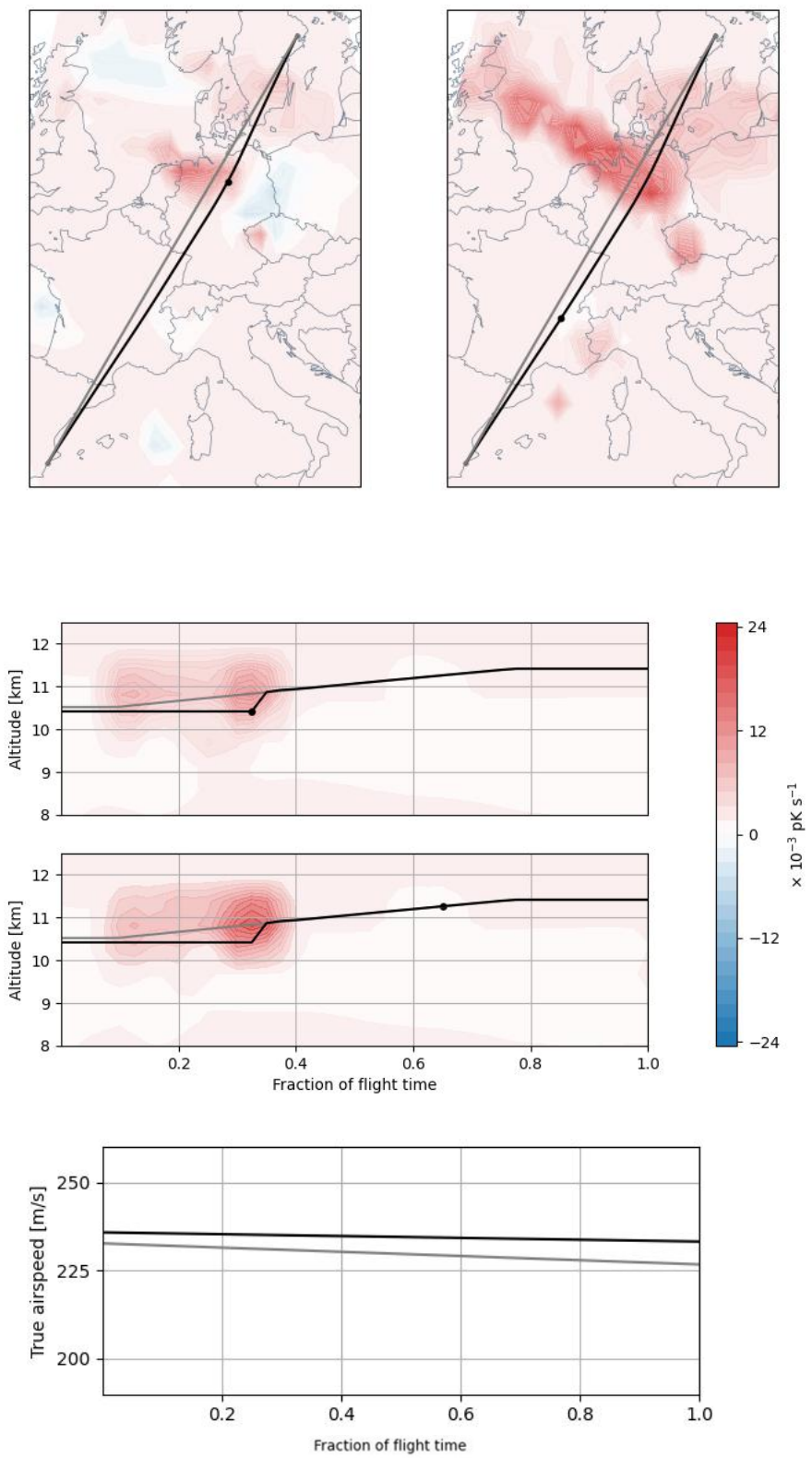

Figure B.8: Visualisation of the flight diversions for trajectory optimisation with a fuel use increase of 0.3%. Horizontal rerouting is shown at the top, changes in altitude are shown in the middle, and velocity changes at the bottom. The grey line represents the fuel optimal route and the black one the optimised trajectory.

Stockholm to Alicante during the day with hydrogen

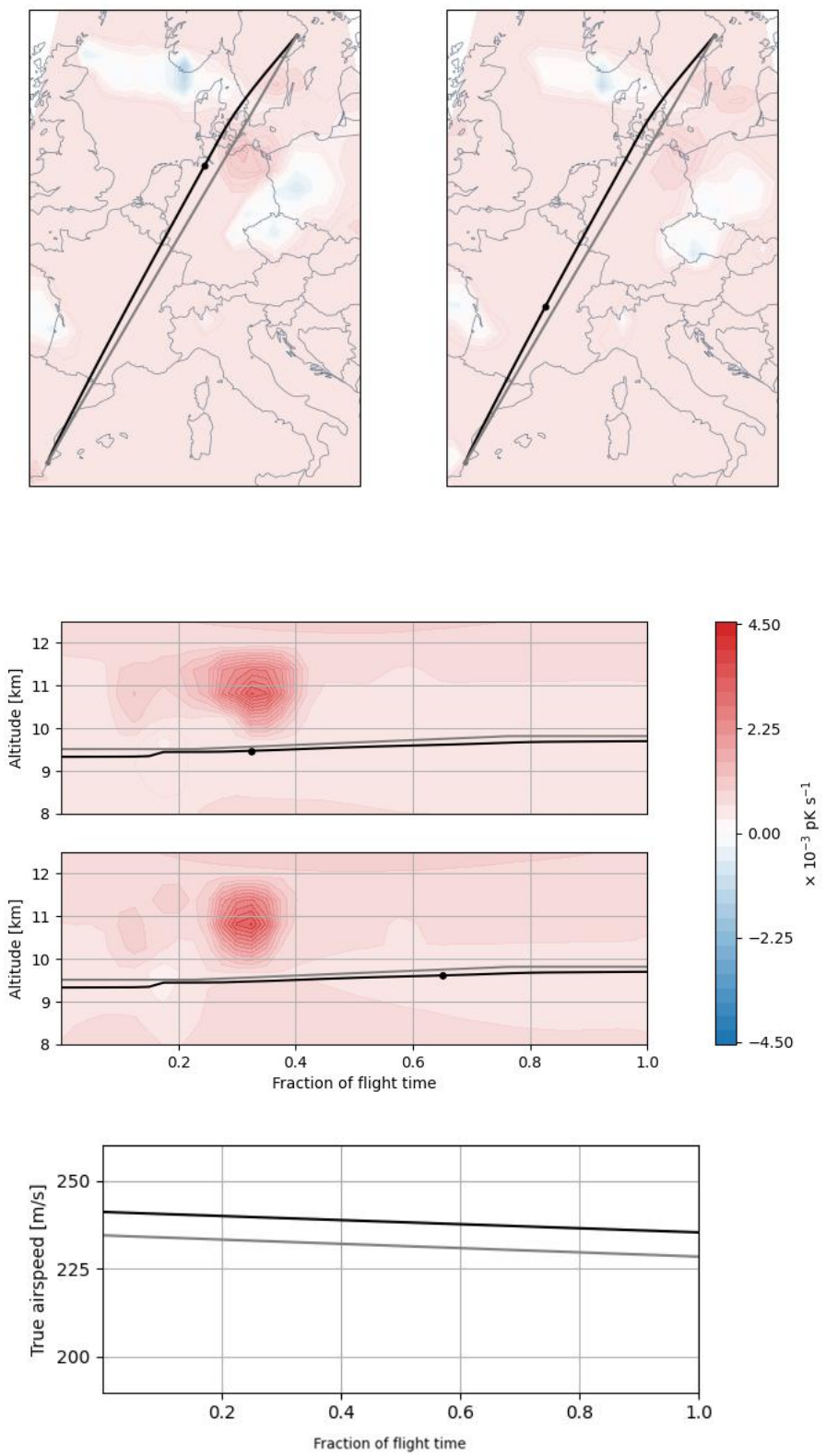

Figure B.9: Visualisation of the flight diversions for trajectory optimisation with a fuel use increase of 0.4%. Horizontal rerouting is shown at the top, changes in altitude are shown in the middle, and velocity changes at the bottom. The grey line represents the fuel optimal route and the black one the optimised trajectory.

Stockholm to Alicante during the night with Jet A-1

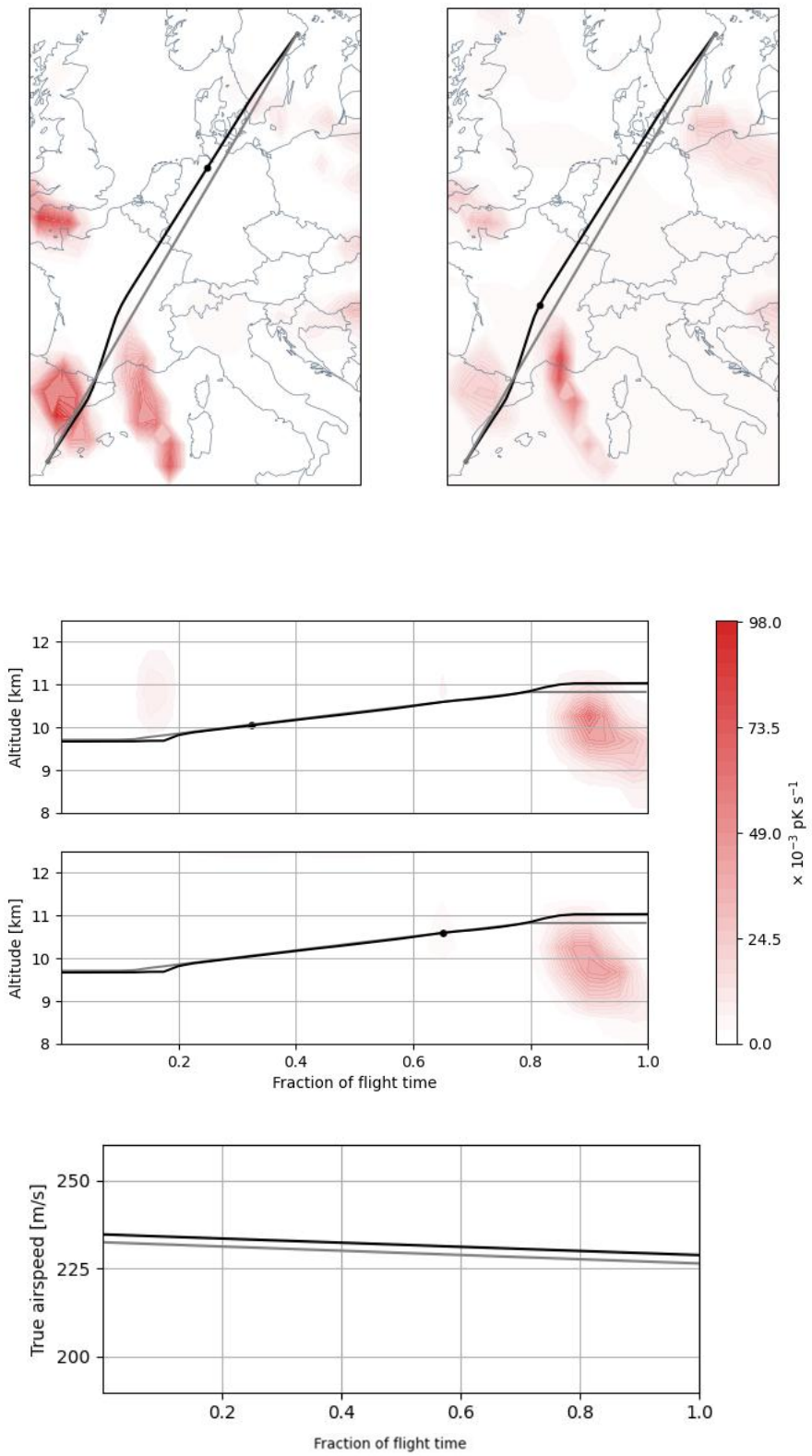

Figure B.10: Visualisation of the flight diversions for trajectory optimisation with a fuel use increase of 0.5%. Horizontal rerouting is shown at the top, changes in altitude are shown in the middle, and velocity changes at the bottom. The grey line represents the fuel optimal route and the black one the optimised trajectory.

Stockholm to Alicante during the night with a 70% SAF blend

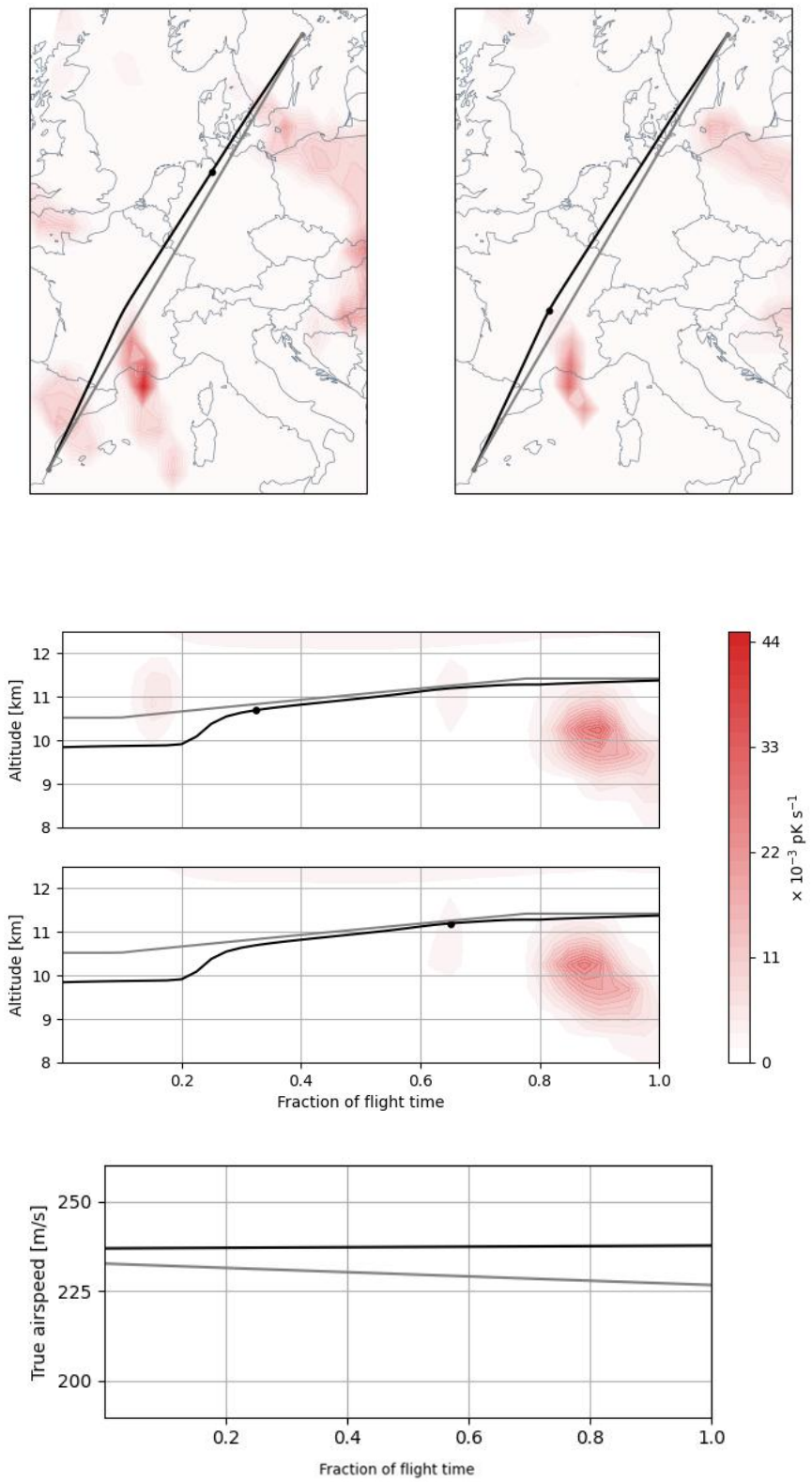

Figure B.11: Visualisation of the flight diversions for trajectory optimisation with a fuel use increase of 1.5%. Horizontal rerouting is shown at the top, changes in altitude are shown in the middle, and velocity changes at the bottom. The grey line represents the fuel optimal route and the black one the optimised trajectory.

Stockholm to Alicante during the night with hydrogen

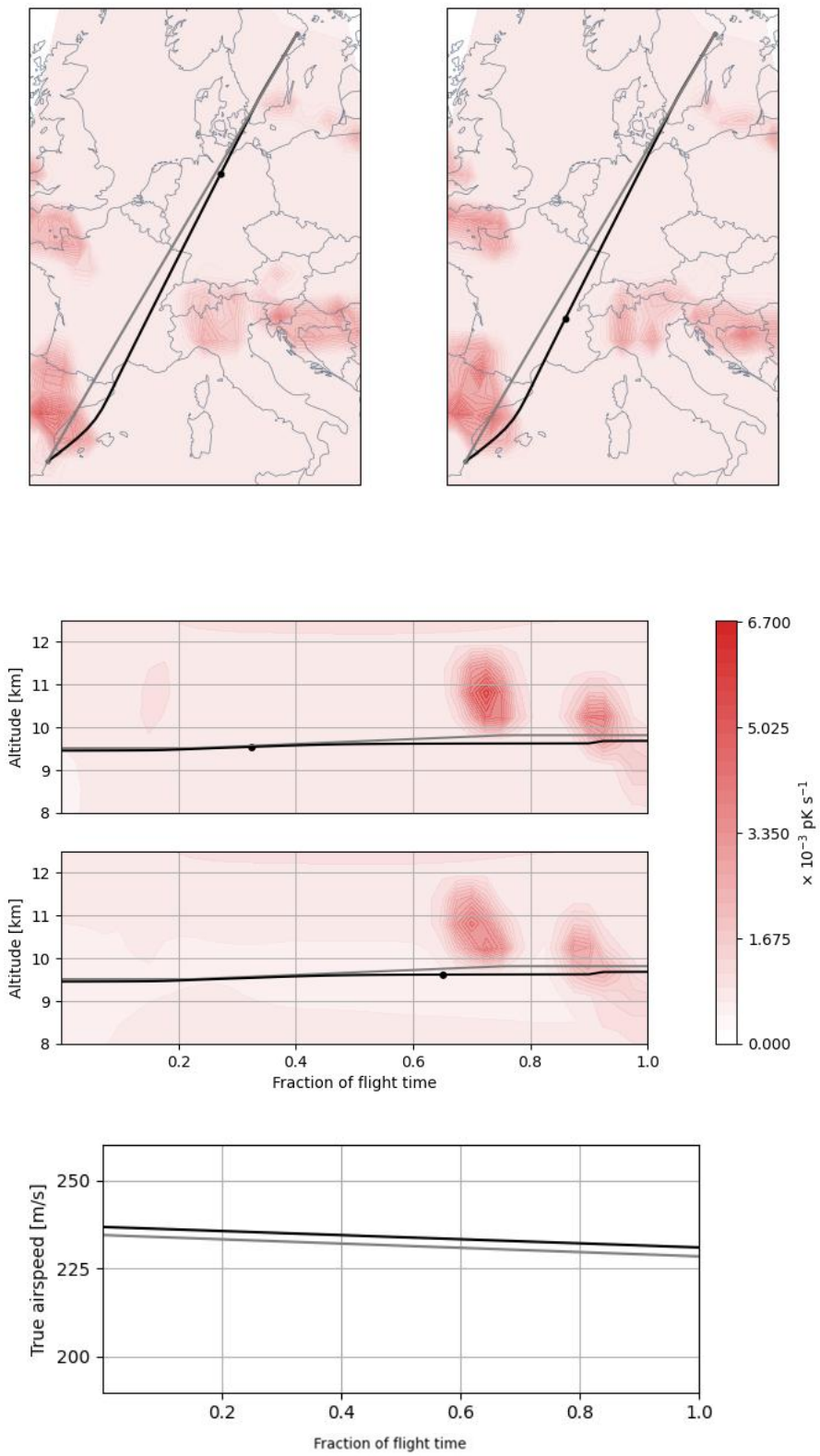

Figure B.12: Visualisation of the flight diversions for trajectory optimisation with a fuel use increase of 0.9%. Horizontal rerouting is shown at the top, changes in altitude are shown in the middle, and velocity changes at the bottom. The grey line represents the fuel optimal route and the black one the optimised trajectory.

Antalya to Bergen during the day with Jet A-1

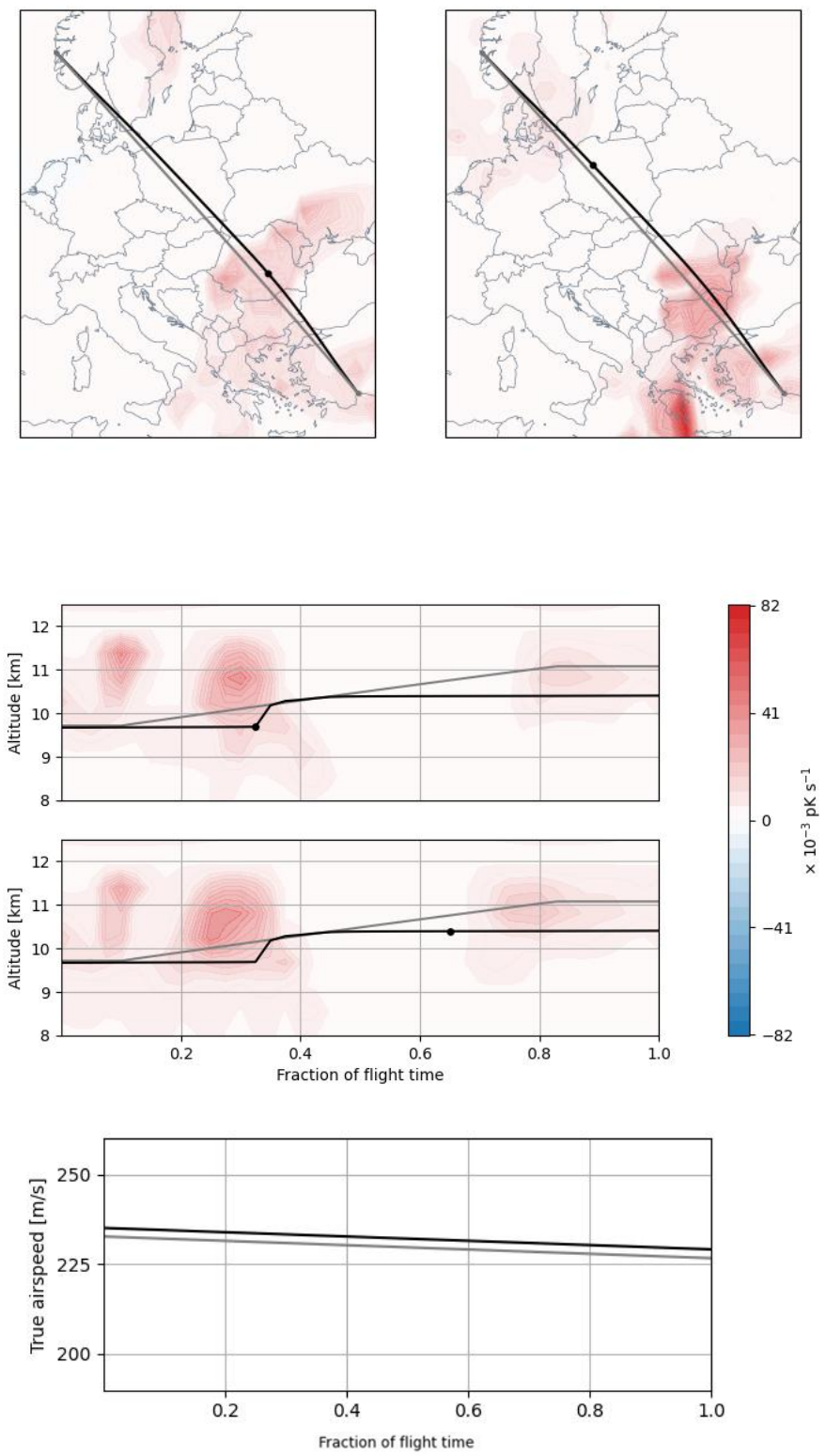

Figure B.13: Visualisation of the flight diversions for trajectory optimisation with a fuel use increase of 1%. Horizontal rerouting is shown at the top, changes in altitude are shown in the middle, and velocity changes at the bottom. The grey line represents the fuel optimal route and the black one the optimised trajectory.

Antalya to Bergen during the day with a 70% SAF blend

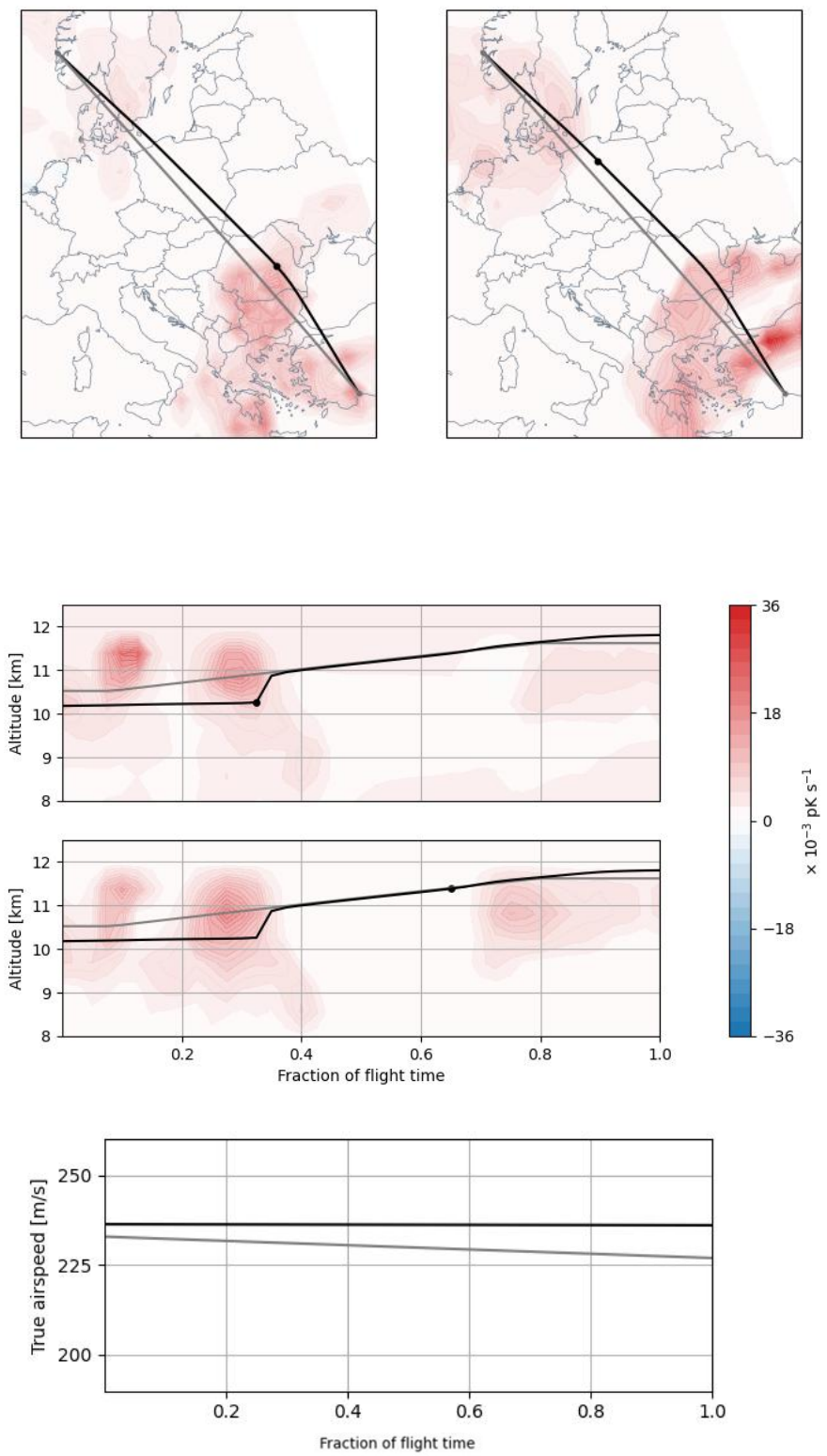

Figure B.14: Visualisation of the flight diversions for trajectory optimisation with a fuel use increase of 1.3%. Horizontal rerouting is shown at the top, changes in altitude are shown in the middle, and velocity changes at the bottom. The grey line represents the fuel optimal route and the black one the optimised trajectory.

Antalya to Bergen during the day with hydrogen

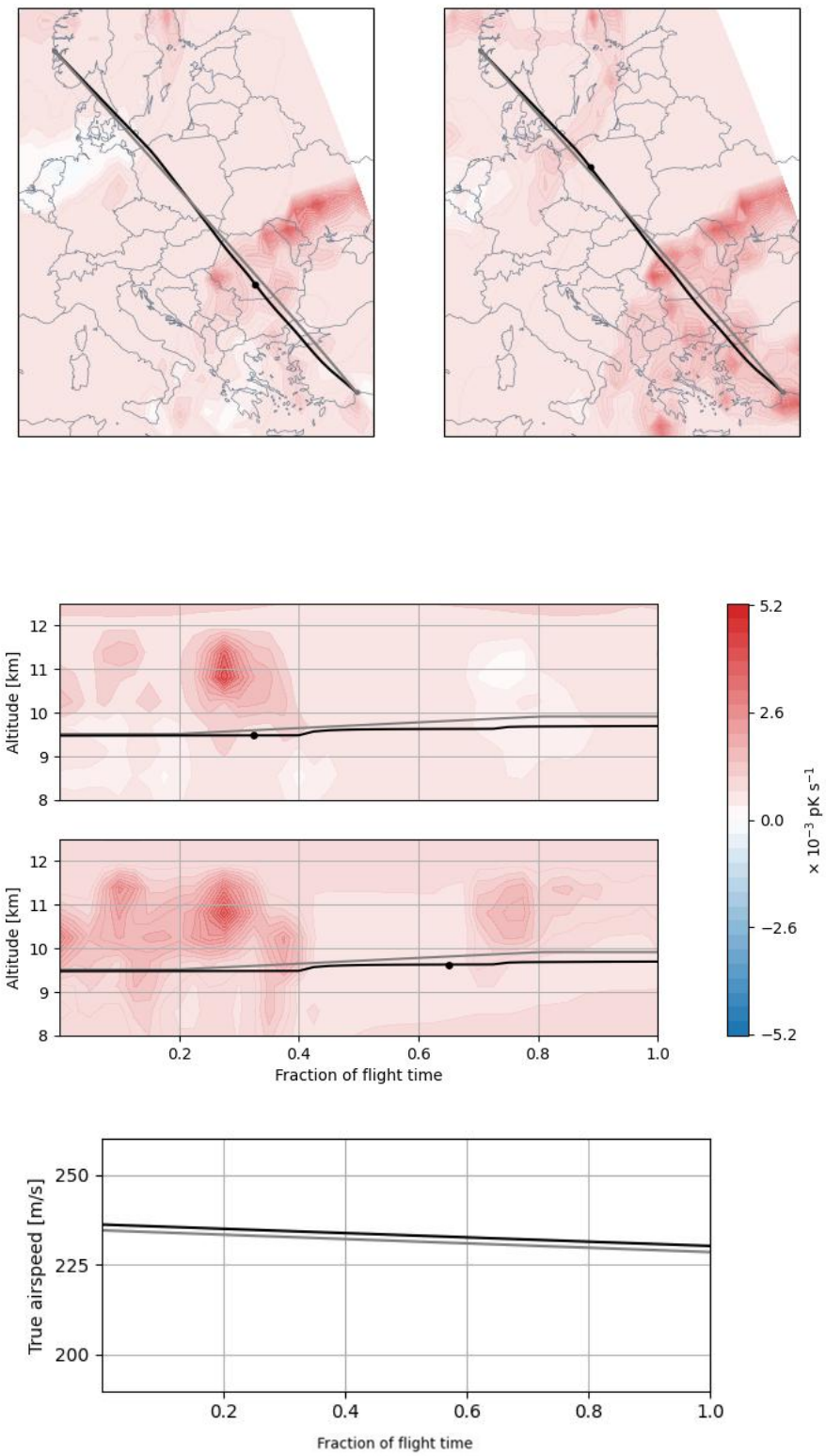

Figure B.15: Visualisation of the flight diversions for trajectory optimisation with a fuel use increase of 0.4%. Horizontal rerouting is shown at the top, changes in altitude are shown in the middle, and velocity changes at the bottom. The grey line represents the fuel optimal route and the black one the optimised trajectory.

Antalya to Bergen during the night with Jet A-1

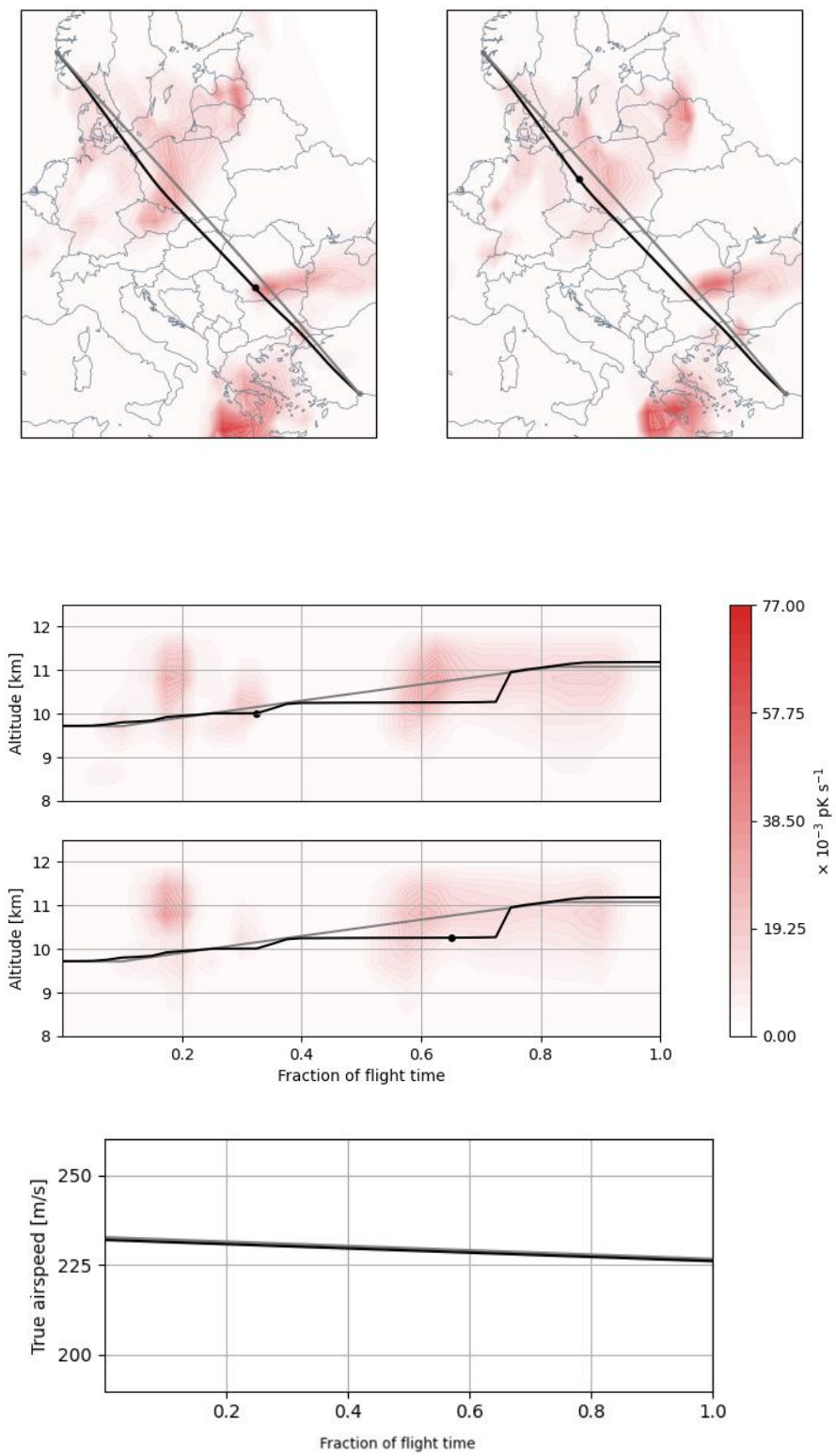

Figure B.16: Visualisation of the flight diversions for trajectory optimisation with a fuel use increase of 0.7%. Horizontal rerouting is shown at the top, changes in altitude are shown in the middle, and velocity changes at the bottom. The grey line represents the fuel optimal route and the black one the optimised trajectory.

Antalya to Bergen during the night with a 70% SAF blend

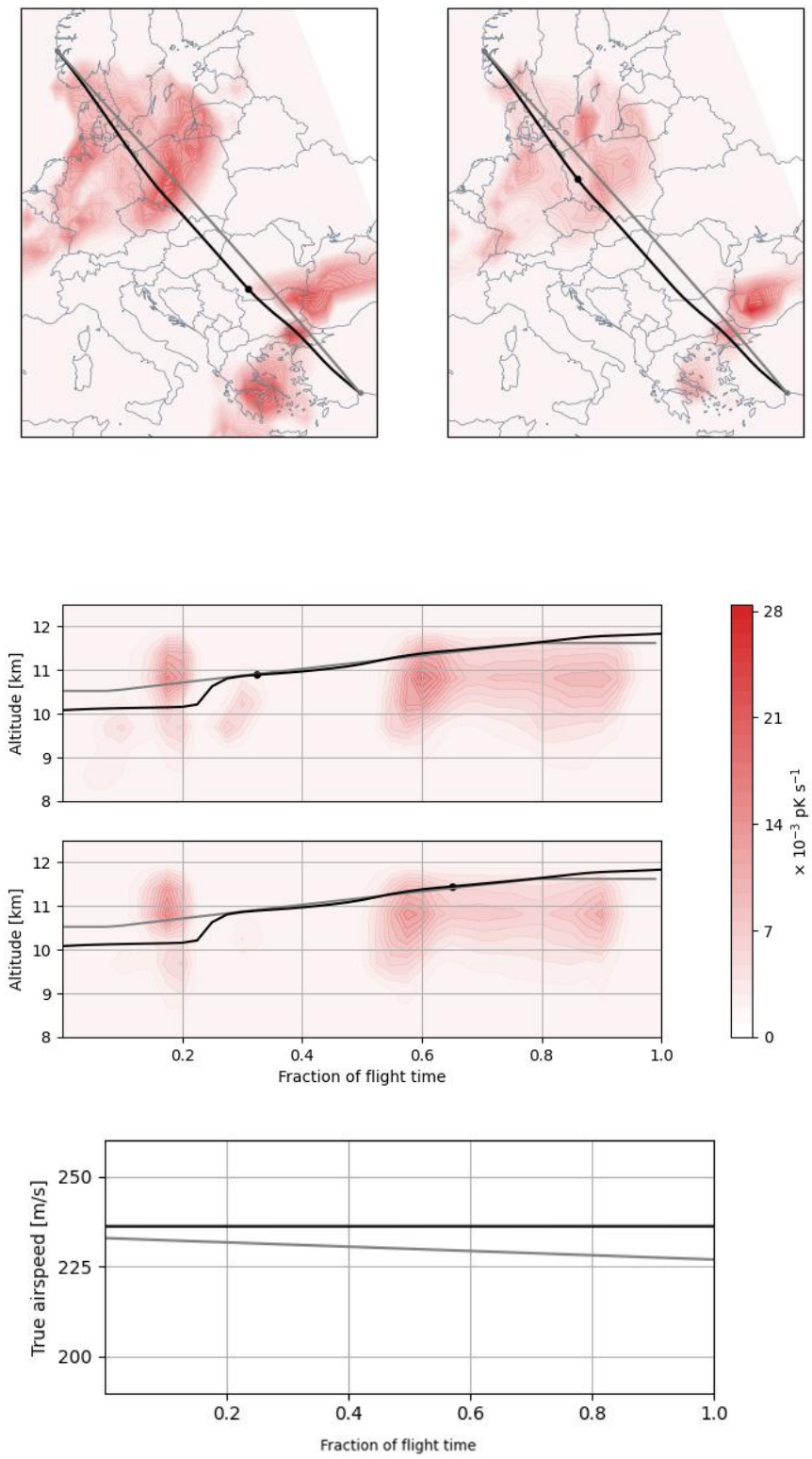

Figure B.17: Visualisation of the flight diversions for trajectory optimisation with a fuel use increase of 1.6%. Horizontal rerouting is shown at the top, changes in altitude are shown in the middle, and velocity changes at the bottom. The grey line represents the fuel optimal route and the black one the optimised trajectory.

Antalya to Bergen during the night with hydrogen

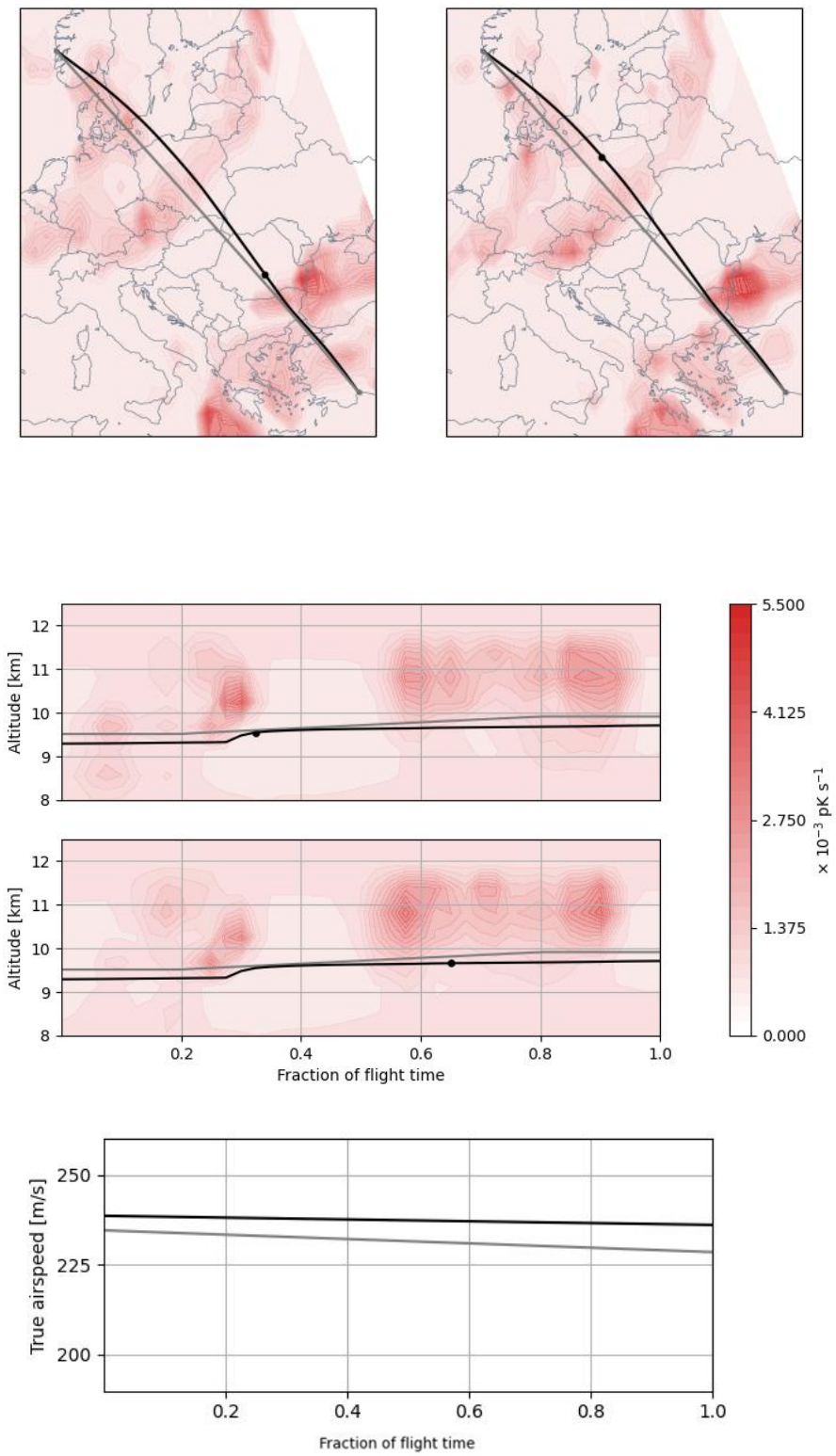

Figure B.18: Visualisation of the flight diversions for trajectory optimisation with a fuel use increase of 0.9%. Horizontal rerouting is shown at the top, changes in altitude are shown in the middle, and velocity changes at the bottom. The grey line represents the fuel optimal route and the black one the optimised trajectory.

Amsterdam to Athens during the night with hydrogen
Optimistic technology scenario

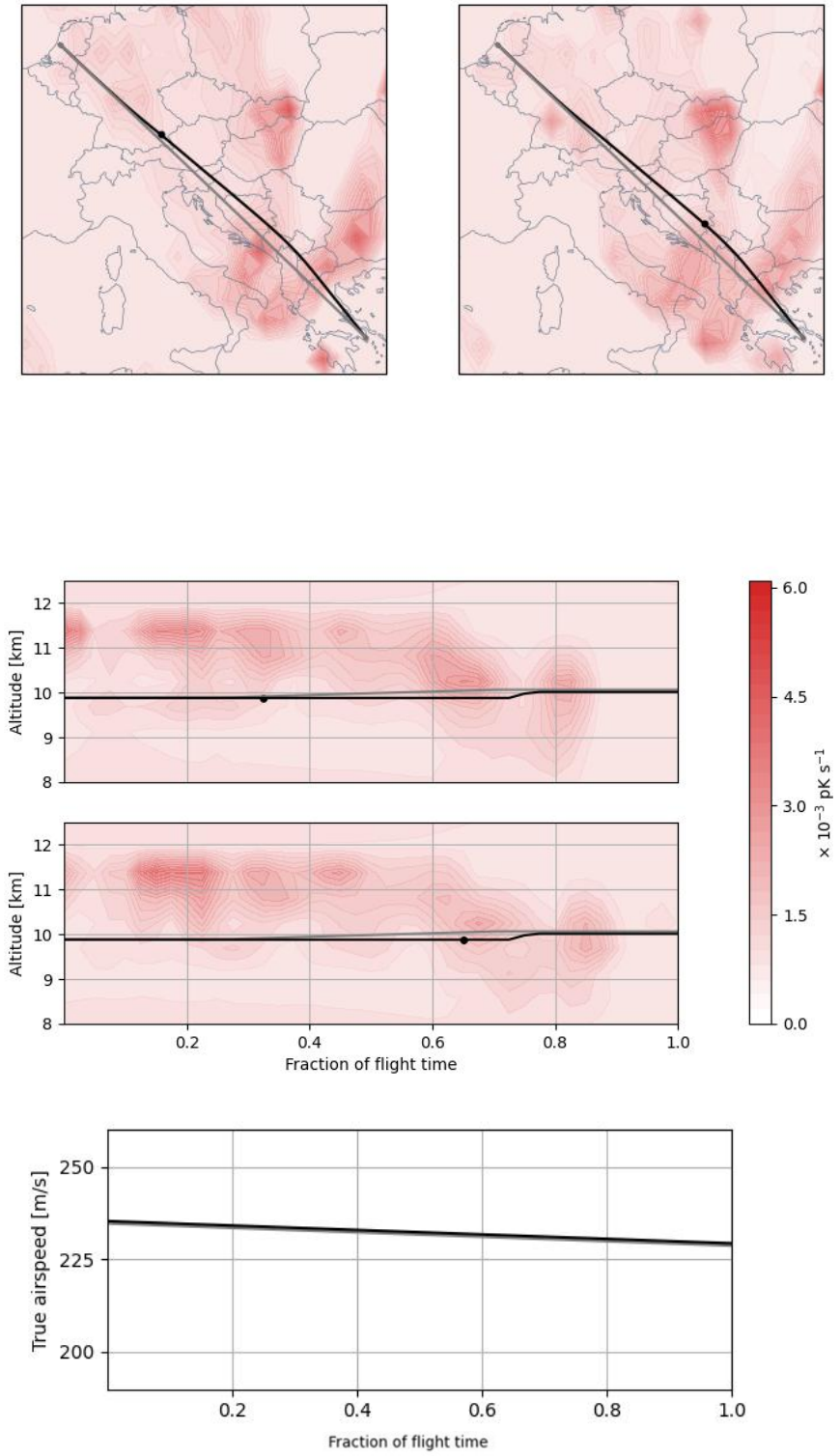

Figure B.19: Visualisation of the flight diversions for trajectory optimisation with a fuel use increase of 0.3%. The graphs are shown for an optimistic scenario regarding technology advancements for hydrogen in the aviation sector. As such, a decrease in take-off mass and fuel flow is considered, as well as an increase in overall propulsion efficiency, compared to the baseline hydrogen-powered aircraft used in this research. Horizontal rerouting is shown at the top, changes in altitude are shown in the middle, and velocity changes at the bottom. The grey line represents the fuel optimal route and the black one the optimised trajectory.

Amsterdam to Athens during the night with hydrogen
Pessimistic technology scenario

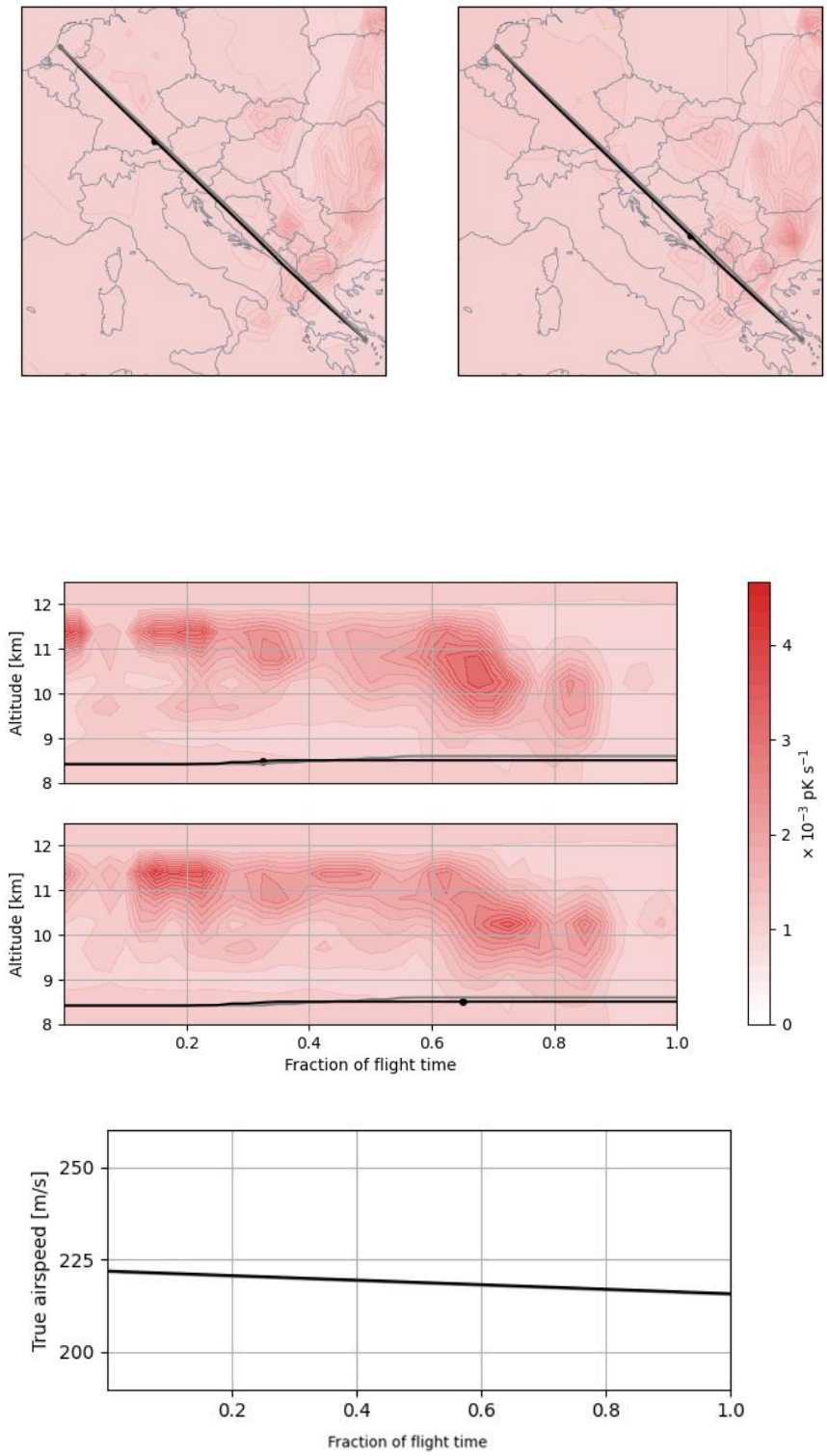

Figure B.20: Visualisation of the flight diversions for trajectory optimisation with a fuel use increase of 0.1%. The graphs are shown for an pessimistic scenario regarding technology advancements for hydrogen in the aviation sector. As such, an increase in take-off mass and fuel flow is considered, as well as a decrease in overall propulsion efficiency, compared to the baseline hydrogen-powered aircraft used in this research. Horizontal rerouting is shown at the top, changes in altitude are shown in the middle, and velocity changes at the bottom. The grey line represents the fuel optimal route and the black one the optimised trajectory.